



HAL
open science

ZnO micro- and nanostructures from Deep-UV photosensitive solutions for electronic and magnetic applications

Chun-Cheng Yeh

► **To cite this version:**

Chun-Cheng Yeh. ZnO micro- and nanostructures from Deep-UV photosensitive solutions for electronic and magnetic applications. Other. Université de Haute Alsace - Mulhouse, 2017. English. NNT : 2017MULH1359 . tel-02088153

HAL Id: tel-02088153

<https://theses.hal.science/tel-02088153>

Submitted on 2 Apr 2019

HAL is a multi-disciplinary open access archive for the deposit and dissemination of scientific research documents, whether they are published or not. The documents may come from teaching and research institutions in France or abroad, or from public or private research centers.

L'archive ouverte pluridisciplinaire **HAL**, est destinée au dépôt et à la diffusion de documents scientifiques de niveau recherche, publiés ou non, émanant des établissements d'enseignement et de recherche français ou étrangers, des laboratoires publics ou privés.

UNIVERSITE DE HAUTE-ALSACE
UNIVERSITE DE STRASBOURG

Année 2017

N° d'ordre :

Thèse

Présentée pour l'obtention du grade de Présentée pour l'obtention du grade de

Docteur de l'Université de Haute-Alsace

Ecole Doctorale : Sciences Exactes

Discipline : Chimie Physique

Présentée et soutenue publiquement

par

Chun-Cheng YEH

7 novembre 2017

ZnO micro- and nanostructures from Deep-UV photosensitive solutions for electronic and magnetic applications.

Sous la Direction de : Dr. Olivier SOPPERA, Institut de Sciences des Matériaux de Mulhouse

Jury : Prof. Gilles LERONDEL, Université de Technologie de Troyes (Rapporteur)
Dr. Jean-Hervé TORTAI, CNRS LTM Grenoble (Rapporteur)
Prof. Yves JOURLIN, Université de Saint-Etienne (Examinateur)
Prof. Dominique BERLING, Université de Haute-Alsace (Examinateur)
Dr. Olivier SOPPERA, CNRS IS2M Mulhouse (Directeur)
Prof. Hsiao-Wen ZAN, National Chiao Tung University (Co-directrice)

List of Acronyms

A.

AFM: atomic force microscope

AGFM: alternative field magnetometer

ALD: atomic layer deposition

B.

C.

CT: charge transfer

CVD: chemical vapor deposition.

D.

DUV: deep-ultraviolet

DMS: diluted magnetic semiconductor

E.

EUV: extreme ultraviolet

EBL: electron-beam lithography

F.

FTIR: fourier transform infrared spectroscopy

FC: field-cooling

FM: ferromagnetism

G.

GMR: giant magnetoresistance

H.

I.

I_D - V_G : drain current versus gate voltage

I_D - V_D : drain current versus drain voltage

J.

J_{sd} : s-d exchange parameter

K.

L.

LCD: liquid crystal display

M.

MOS: metal oxide semiconductor

MAA: methacrylate

MEA: ethanolamine

M-O-M: metal-oxygen-metal

M-H: magnetization versus field

MSP: magnetron sputtering

N.

NBE: near-band emission

NW: nanowire

O.

OLED: organic light emitting diode

OM: optical microscopy.

P.

PL: photoluminescence

PLD: pulsed laser deposition

PEB: post exposure baking

Q.

R.

RTFM: room-temperature ferromagnetism

S.

S.S.: subthreshold swing

SQUID: superconducting quantum interference device

SEM: scanning electron microscope

T.

TEM: transmission electron microscope

TFT: thin-film transistor

TCO: transparent conductive oxide

TPD: temperature programmed desorption

TM: transition metal

T_B: blocking temperature

U.

UV: ultraviolet

UV-vis: ultraviolet-visible

V.

W.

X.

XRD: X-ray diffraction

XPS: X-ray photoelectron spectroscopy

Y.

Z.

ZnMAA: zinc methacrylate

ZFC: zero-field cooling

Table of Contents

Introduction.....	1
Chapter I: Introduction	8
Résumé du Chapitre I.....	12
1.1. Metal-oxide thin films.....	13
1.1.1 Physical and chemical properties of metal-oxide thin films.....	13
1.1.2. Metal oxide thin film deposition	16
1.1.2.1 Vapor-phase deposition.....	16
1.1.2.2 Solution Processing	19
1.2. Direct-patterning techniques for metal oxide precursor	23
1.2.1. E-beam writing.....	24
1.2.2. E-jet printing	25
1.2.3. Micromolding	26
1.2.4. Selective surface wetting.....	26
1.3 Photo-induced patterning	27
1.3.2. Photo-induced crosslinking and decomposition of organic species in photosensitive metal oxide precursor	28
1.3.3. Photopatterning of metal oxide precursor as negative tone resist.....	30
1.3.4. Photopatterning of metal oxide precursor as positive tone resist.....	32
1.4. Applications of solution-processed metal oxide films and patterns	34
1.4.1. Thin-film transistors	34
1.4.2. Transparent electrodes	37
1.4.3. Photodetectors	39
1.5. Applications nanostructured metal oxides	41
1.5.1. Gas sensors	41
1.5.2. Nanowire transistors.....	45
1.6. Transition metal doped metal oxide semiconductors for spin-based applications.....	46
1.7. Bibliography	49
Chapter II: Experimental Methods.....	52
Résumé du Chapitre II	56
2.1. Solution preparation.....	57

2.2. Thin film deposition	58
2.3. DUV-patterning	58
2.4. Development procedure	59
2.5. Thin film characterization	61
2.5.1. X-ray photoelectron spectrometry (XPS)	61
2.5.2. Fourier Transform Infrared (FTIR)	62
2.5.3. Raman spectroscopy	63
2.5.4. X-ray diffraction (XRD)	64
2.5.5. Temperature- Programmed Desorption (TPD).....	65
2.5.6. Optical measurements	65
2.6. Thin-film transistor fabrication and electrical measurements	66
2.7. Gas sensing and micro-fluid gas sensing system	66
2.8. Magnetic measurements	67
2.9. Bibliography	68

Chapter III: DUV-patterned ZnO micro- and nanostructures for electronic applications	69
Résumé du chapitre III	73
3.1. Introduction	74
3.2. Solution synthesis and chemical characterization of photosensitive zinc methacrylate precursor	74
3.2.1. Ellipsometry characterization of DUV-induced photoreaction	75
3.2.2. FTIR characterization	76
3.2.3. XPS characterization	79
3.2.4. Raman spectroscopy	81
3.2.5. XRD analysis	82
3.2.6. TPD.....	83
3.3. DUV-patterned ZnO nanostructures	85
3.4. Electrical and gas sensing properties of DUV-patterned ZnO structures	87
3.4.1. Electrical properties.....	87
3.4.2. Sensor properties.....	89
3.5. Enhancing conductivity of ZnO structures by doping group III elements	92
3.6. Conclusion and perspective	93
3.7. Bibliography	94

Chapter IV: Chemical and structural investigation of

Zn-oxo cluster photoresist	96
Résumé du Chapitre IV.....	100
4.1. Introduction.....	101
4.2. Formation of Zn-oxo clusters in precursor solution.....	102
4.3. DUV Exposure.....	103
4.4. Prebaking.....	106
4.5. Development	108
4.6. Thermal annealing.....	109
4.7. Conclusion and perspective	114
Chapter V: Effect of Co-doping on photo-patterned ZnO structures.....	117
Résumé du chapitre V	121
5.1. Introduction.....	121
5.2. Investigating the incorporation of Co ions into ZnO lattice.....	122
5.3. Magnetic and electrical measurements of Co:ZnO films.....	126
5.3.1. Magnetic properties of Co:ZnO films	126
5.3.2. Electrical properties of Co:ZnO films.....	129
5.4. DUV-patterned Co:ZnO micro- and nanostructures	130
5.5 Conclusion and perspective	132
5.6. Bibliography	133
Conclusions and outlook	135

Introduction

Les matériaux semiconducteurs à base d'oxydes métalliques connaissent depuis plusieurs dizaines d'années un intérêt important, et tout particulièrement sous leurs formes nanostructurées, pour des applications en nanosciences et nanotechnologies. Parmi les différents oxydes métalliques disponibles, l'oxyde de Zinc (ZnO) connaît un engouement important, notamment pour des applications dans des domaines assez variés tels que les nanogénérateurs,^[1] les capteurs de gaz,^[2] les biocapteurs,^[3] les photodétecteurs,^[4] les composants pour la spintronique,^[5] ou les transistors à effets de champs.^[6] De surcroît, ZnO est un matériau transparent dans le domaine du visible (le bandgap est de l'ordre de 3,3 eV), ce qui en fait un excellent candidat pour des composants électronique transparents. Une autre caractéristique déterminante est la possibilité de moduler dans une large mesure les propriétés électriques, optiques ou magnétiques par dopage avec de petites quantités d'autres éléments : le dopage par des éléments du groupe III tels que le gallium,^[7] l'aluminium,^[8] l'indium,^[9] permettent d'augmenter significativement la conductivité. Différentes études ont prouvé par ailleurs des propriétés de ferromagnétisme à température ambiante dans du ZnO dopé par des métaux de transition.^[10] Les propriétés intrinsèques de ZnO, dopé ou non, sont donc extrêmement intéressantes mais un des freins à la réalisation de dispositifs intégrant un tel matériau est lié à la difficulté d'intégrer les oxydes métalliques, micro- ou encore plus nanostructurés.

C'est dans ce contexte que des travaux récents décrivent la possibilité de préparer par des voies liquides des oxydes métalliques tels que a-IGZO, ZnO, ZTO, ITO, ZrO₂, TiO₂, and HfO₂ en les structurant directement par des techniques d'écriture directe telles que la photolithographie UV profond (DUV), Extrême-UV (EUV), ou la lithographie par faisceau d'électrons.^[11-15] La voie liquide présente de nombreux avantages en comparaison avec les techniques de dépôts physiques, en général sous vide, comme un coût des équipements et de procédés bien moindres, tout en garantissant une grande variété de compositions, différents précurseurs pouvant aisément être mélangés en solution pour adapter les propriétés finales du matériau.

Certains travaux concernent l'écriture directe de nanostructures de ZnO. M.S.M. Saifullah *et al.* ont ainsi démontré la possibilité d'élaborer des nanostructures ZnO par lithographie e-beam.^[13] Dans ce cas, la nature du précurseur (Zinc naphthenate) a été judicieusement choisie pour générer une solidification du précurseur induite par le faisceau d'électron. Le matériau irradié devient ainsi

insoluble, ce qui permet de définir la nanostructure en éliminant la partie non-irradiée dans un solvant adéquat. La résine de précurseur de ZnO a donc le comportement d'un photoresist négatif. Dans cet exemple, le recours à la lithographie e-beam a permis aux auteurs d'obtenir une résolution de 5 nm, démontrant ainsi que la résolution intrinsèque de ce type de résines est excellente et permet de répondre aux exigences des prochaines générations de lithographie. Toutefois, la technique de nanolithographie utilisée est complexe, coûteuse et la vitesse d'écriture trop lente pour des applications industrielles. Pour cette raison, les voies photochimiques (mettant en œuvre des radiations lumineuses) connaissent toujours un intérêt important. V. Auzelyte *et al.* ont ainsi utilisé une source EUV (13,5 nm) pour produire des nanostructures ZnO de largeur 10 nm, en utilisant le même type de précurseur Zinc naphthenate.^[14] Peu de détails sont en revanche donnés sur les mécanismes moléculaires conférant la photosensibilité à la résine à cette longueur d'onde. La photolithographie EUV est par ailleurs pressentie pour remplacer la lithographie DUV mais des difficultés liées à la forte absorption des matériaux à cette longueur d'onde et la faible stabilité et puissance des sources lumineuses en limite la portée.^[16]

Cette thèse s'inscrit dans cet objectif de proposer une voie de micro et nanostructuration directe de matériau ZnO en combinant chimie en solution et lithographie DUV. La lithographie DUV a plusieurs avantages par rapport aux autres technologies de lithographie, notamment celui d'être compatible avec une structuration à l'échelle nanométrique inférieure à 50 nm. D'autre part, elle est largement utilisée dans l'industrie des semi-conducteurs aujourd'hui et aucun système de vide n'est nécessaire.

ZnMAA a été choisi comme précurseur photosensible en raison de sa grande stabilité et parce que le complexe s'est révélée photosensible à la lumière dans la gamme DUV.^[15] Les solutions et les films minces de précurseur ZnMAA ont été caractérisés par diverses analyses optiques et chimiques afin de décrire les réactions chimiques induites par l'irradiation DUV et la formation de ZnO à partir du précurseur dans diverses conditions expérimentales. En outre, les nanostructures ZnO et les variations structurelles causées par le traitement thermique ont été étudiées par microscopie à force atomique.

Afin de confirmer que les nanostructures ZnO sont semi-conductrices, ce qui est requis pour les applications en électronique, des mesures électriques ont été effectuées. Les propriétés magnétiques ont également été introduites avec succès dans des structures ZnO, ce qui permet également d'étendre les applications vers des dispositifs magnétiques. Dans ce cas, la solution de précurseur de zinc a été dopée

avec des ions cobalt pour obtenir des films minces Co: ZnO tout en conservant la propriété d'écriture directe.

Plus précisément, le chapitre I fournit des informations générales sur les techniques de photostructuration des oxydes métalliques et leurs applications principales. Le chapitre II décrit les méthodes expérimentales utilisées dans cette étude, en particulier la lithographie par interférence DUV, et les méthodes de caractérisation du matériau pendant les différentes étapes de fabrication. Les chapitres III à V présentent les principaux résultats concernant la photostructuration de ZnO sous DUV et les propriétés électriques, optiques et magnétiques du matériau structuré. Le chapitre III décrit plus particulièrement les photoréactions provoquées par l'irradiation DUV et démontre l'intérêt des nanostructures ZnO dans des applications électroniques et pour la détection de gaz. Dans le chapitre IV a été menée une étude approfondie sur les effets de l'irradiation DUV et du recuit thermique sur les propriétés physiques et la forme structurale des motifs ZnO. Enfin, le chapitre V ouvre sur des perspectives sur les propriétés magnétiques des motifs ZnO dopés par des ions Co.

Introduction

Nanostructured metal oxide semiconductors have attracted during the last decades a great deal of attention in nanosciences and nanotechnology due to their various applications in the elaboration of nanoscale devices. Among all kinds of metal oxides, zinc oxide (ZnO) has known a fast growing interest for the fabrication of many devices including nanogenerator,^[1] gas sensors,^[2] biosensors,^[3] photodetectors,^[4] spintronic devices,^[5] and field-effect transistors.^[6] Furthermore, ZnO is transparent under visible light (the bandgap of ZnO is as wide as 3.3eV), making it a promising material for transparent electronics. Another important feature of ZnO is its controllable electrical, optical and magnetic performance by doping with small amount of elements: it was reported that doping ZnO with a little amount of group III element such as gallium,^[7] aluminum,^[8] and indium^[9] results in effective enhancement of conductivity. Also, many studies reported the observation of above-room-temperature ferromagnetism from transition-metal-doped ZnO.^[10] However, fabricating ZnO nanostructures on desired positions as building blocks for nanoscale devices remains a difficult problem.

Recently, metal oxide materials such as a-IGZO, ZnO, ZTO, ITO, ZrO₂ TiO₂, and HfO₂ derived from solution process combined with direct-patterning techniques including DUV lithography, EUV lithography, and e-beam lithography, have been demonstrated.^[11-15] Solution process has the advantages of low-cost and precise stoichiometric control. Through direct-patterning technologies, it is easy to fabricate sophisticated ZnO nanostructures on desired locations. M.S.M. Saifullah *et al.* demonstrated direct-patterned high-aspect-ratio ZnO nanostructures by using electron-beam lithography.^[13] Zinc naphthenate was chosen as precursor, and the solidification of zinc naphthenate under electron-beam irradiation was ascribed to crosslinking between $-C=O$ and/or $-(CH_2)_n-$, making it insoluble in toluene. Line-width as small as 5 nm was achieved after thermal annealing. However, electron beam lithography is very time consuming and requires expensive tool and fabrication condition (vacuum), which limits its interest for industrial applications.

V. Auzelyte *et al.* have performed a direct-patterning method to produce ZnO nanostructures as small as 10nm by extreme ultraviolet (EUV) light interference.^[14] Zinc naphthenate, again, was used as precursor. In this article, however, there is no detailed explanation about the photochemical reactions between zinc naphthenate and EUV light. Thanks to its extremely short wavelength (13.5 nm), EUV lithography has been proposed as a potential replacement for DUV lithography to achieve higher

resolution needed for the next generations of photolithography for microelectronics. However, many challenges prevent EUV lithography from being adopted in semiconductor industries, such as strong absorption of EUV wavelength by any material and low reliability of EUV sources.^[16] Moreover, any gas molecules in the path of EUV light should be avoided. Thus high-cost vacuum system is needed for EUV lithography.

This thesis aims to develop functional ZnO nanostructures with the use of photosensitive zinc oxide precursor, zinc methacrylate (ZnMAA), and DUV lithography. DUV lithography has several advantages over other lithography technologies, including that it is compatible with nanoscale patterning smaller than 50 nm, it is widely used in today's semiconductor industry and no vacuum system is needed. In addition, DUV-direct patterning avoids multistep processes, showing excellent controllability on dimension and position. ZnMAA was chosen as a photosensitive precursor due to its high stability and because C=C bond in the molecular structure was proven to be photosensitive to light in DUV range.^[15]

Solutions and thin films from ZnMAA precursor were characterized by various optical and chemical analyses in order to monitor the DUV-induced chemical reactions and the formation of ZnO from the precursor in various experimental conditions. In addition, DUV-patterned structures and the structural variations caused by thermal treatment were investigated by atomic force microscopy. In order to confirm that the photo-patterned ZnO structures are semiconducting, which is necessary for their applications in electronic devices, electrical measurements were performed. Magnetic properties were also successfully introduced into DUV-patterned ZnO structures, which is important for extending their applications in magnetic devices. In this case, the zinc precursor solution was doped with cobalt ions for obtaining Co:ZnO thin-films and nanostructures. Their magnetic properties were investigated by alternative field magnetometer and superconducting quantum interference device.

In more details, Chapter I provides background information about photo-patterning techniques, photo-induce polymerization and application of metal oxide devices. Chapter II describes experimental methods used in this study including DUV interference lithography which is able to pattern nanoscale metal oxide structures. Chapter III to V present and discuss the results of DUV-patterned ZnO structures and their electrical, optical and magnetic properties. Specifically, Chapter III describes photoreactions provoked by DUV irradiation and shows DUV-patterned ZnO nanostructures and their electrical and gas sensing performance. In Chapter IV, we carried out an in-depth investigation to the

effects of DUV-patterning and thermal annealing on physical properties and structural shape of ZnO patterns. In Chapter VI, we investigated the effects of DUV-patterning on electrical, optical and magnetic properties of Co-doped ZnO patterns. Summaries and outlooks are given in the end of each chapter.

- [1] X. Wang, J. Song, J. Liu, Z. L. Wang, *Science* 2007, 316, 102.
- [2] S. J. Chang, T. J. Hsueh, I. Chen, S. F. Hsieh, S. P. Chang, C. L. Hsu, Y. R. Lin, B. R. Huang, *IEEE Trans. Nanotechnol.* 2008, 7, 754.
- [3] A. Choi, K. Kim, H. I. Jung, S. Y. Lee, *Sens Actuators B Chem.* 2010, 148, 577.
- [4] S. Bai, W. Wu, Y. Qin, N. Cui, D. J. Bayerl, X. Wang, *Adv. Funct. Mater.* 2011, 21, 4464.
- [5] W. Liang, B. D. Yuhas, P. Yang, *Nano Lett.* 2009, 9, 892.
- [6] Y. W. Heo, L. C. Tien, Y. Kwon, D. P. Norton, S. J. Pearton, B. S. Kang, F. Ren, *Appl. Phys. Lett.* 2004, 85, 2274.
- [7] T. Minami, *Semicond. Sci. Technol* 2005, 20, S35.
- [8] P. K. Nayak, J. Yang, J. Kim, S. Chung, J. Jeong, C. Lee, Y. Hong, *J. Phys. D: Appl. Phys.* 2008, 42, 035102.
- [9] A. K. K. Kyaw, Y. Wang, D. W. Zhao, Z. H. Huang, X. T. Zeng, X. W. Sun, *phys. status solidi (a)* 2011, 208, 2635.
- [10] Z. Yang, *Appl. Phys. A* 2013, 112, 241.
- [11] Y. S. Rim, H. Chen, Y. Liu, S. H. Bae, H. J. Kim, Y. Yang, *ACS Nano* 2014, 8, 9680.
- [12] H. S. Lim, Y. S. Rim, H. J. Kim, *Sci rep.* 2014, 4, 4544.
- [13] M. S. Saifullah, K. R. Subramanian, D. J. Kang, D. Anderson, W. T. Huck, G. A. Jones, M. E. Welland, *Adv. Mater.* 2005, 17, 1757.
- [14] V. Auzelyte, H. Sigg, B. Schmitt, H. H. Solak, *Nanotechnology* 2010, 21, 215302.
- [15] F. Stehlin, F. Wieder, A. Spangenberg, J. M. Le Meins, O. Soppera, *J. Mater. Chem. C* 2014, 2, 277.
- [16] C. Wagner, N. Harned, *Nat. Photonics* 2010, 4, 24.

Chapter I:

Introduction

Résumé du Chapitre I.....	12
1.1. Metal-oxide thin films.....	13
1.1.1 Physical and chemical properties of metal-oxide thin films.....	13
1.1.2. Metal oxide thin film deposition	16
1.1.2.1 Vapor-phase deposition.....	16
1.1.2.2 Solution Processing	19
1.2. Direct-patterning techniques for metal oxide precursor	23
1.2.1. E-beam writing.....	24
1.2.2. E-jet printing	25
1.2.3. Micromolding	26
1.2.4. Selective surface wetting.....	26
1.3 Photo-induced patterning	27
1.3.2. Photo-induced crosslinking and decomposition of organic species in photosensitive metal-oxide precursor	28
1.3.3. Photopatterning of metal oxide precursor as negative tone resist.....	30
1.3.4. Photopatterning of metal oxide precursor as positive tone resist.....	32
1.4. Applications of solution-processed metal oxide films and patterns	34
1.4.1. Thin-film transistors	34
1.4.2. Transparent electrodes	37
1.4.3. Photodetectors	39
1.5. Applications nanostructured metal oxides	41
1.5.1. Gas sensors	41
1.5.2. Nanowire transistors.....	45
1.6. Transition metal doped metal oxide semiconductors for spin-based applications.....	46
1.7. Bibliography	49

Résumé du Chapitre I

Le Chapitre I est une étude bibliographique sur les propriétés des films minces d'oxydes métalliques micro et nanostructurés, et leurs principaux procédés d'élaboration. Cette revue est replacée dans le contexte d'applications en microélectronique, optique, photonique magnétiques et capteurs.

Ce chapitre débute par un rappel rapide des propriétés des oxydes métalliques et leurs principaux intérêts.

Les méthodes de mise en œuvre sont ensuite décrites. Elles sont principalement de deux natures : la préparation de films minces peut être réalisée par des méthodes physiques de dépôt sous vide ou des méthodes chimiques pour lesquelles des solutions d'un ou plusieurs précurseurs sont préparées avant d'être déposées sous forme de films minces par diverses techniques, dont celle utilisée dans ce travail, à savoir le spin-coating.

Un des challenges actuels qui est le cœur de ce travail est de pouvoir, à partir des procédés en solution obtenir des conditions pour l'écriture directe des structures oxydes métalliques. L'enjeu est de pouvoir lever le verrou que constitue l'intégration de ces matériaux fonctionnels dans des dispositifs plus ou moins complexes. Certaines de ces techniques mettent en jeu une radiation qui modifie la solubilité des précurseurs, un dépôt localisé (jet d'encre ou par démouillage) ou un moulage. Parmi les critères importants, le contrôle de la structure aux différentes échelles, la facilité de mise en œuvre et l'élimination de traitements thermiques sont des critères importants.

La solution retenue dans ce travail est la voie photochimique, et plus particulièrement sous irradiation UV-profond (193 nm). L'intérêt de cette voie est de combiner les propriétés originales de ce type de longueur d'onde (photons de grande énergie induisant des photolyses de complexes de métaux de transition, forte absorption) avec les perspectives en termes de résolution à l'échelle nanométrique. Les principaux exemples issus de la littérature qui aborde les mécanismes de photoréticulation dans des précurseurs d'oxydes métalliques sont décrits. Ces procédés reposent majoritairement sur un comportement de résine négative des matériaux. Dans certains cas, un comportement positif peut également être obtenu.

Enfin, les principales applications de ce type de structures sont décrites. Elles concernent les transistors à effets de champ (TFT), les électrodes transparentes et les photodétecteurs. La structuration à l'échelle nanométrique confère des propriétés extrêmement intéressantes trouvant des applications

dans les capteurs de gaz ou les transistors basés sur des nanofils. Enfin, les propriétés magnétiques sont également décrites. L'intérêt de la voie liquide de préparation des oxydes métalliques réside dans la possibilité d'adapter très facilement la composition du matériau pour moduler les propriétés finales (conductivité, mobilité, propriétés magnétiques, etc...).

1.1. Metal-oxide thin films

1.1.1 Physical and chemical properties of metal-oxide thin films

At the atomic scale, the basic structure of metal oxide (MO) is M-O-M network connected by ionic bonds. Because of the difference of electronegativity between M and O, the bonding is ionic and free electrons of metals are bound to oxygen. As a consequence, most of MOs are insulating. MO thin-films have been widely used in transistors and other electronic devices as insulators. Al_2O_3 , ZrO_2 , TiO_2 , Ta_2O_5 , and HfO_2 are known as high-k MO materials because their dielectric constants are higher than SiO_2 . These high-k materials can significantly improve the electrical performance of transistors when used as gate insulator. In addition, due to their wide bandgaps (2-8 eV),^[1] MO materials are transparent under visible light with relatively high refractive indexes and colors, which makes these materials also interesting for optical applications. They have been integrated into a variety of optical devices as lens, encapsulation layers, antireflection coatings, and optical filters.^[2-4] Moreover, electron-hole pairs can be generated in MOs under photoirradiation, which are able to reduce or oxidize organic compounds absorbed on the surface of MOs and gives rise to photocatalytic reactions for air purification, water purification and photoelectrochemical conversion.^[5]

Regarding electrical properties, in the last century, several MO semiconductors such as In_2O_3 , SnO_2 and ZnO having electrical properties were discovered, enabling MO materials to be used for making active layers of transistors. G. F. Boesen *et al.* and Akira Aoki *et al.* integrated Li-doped ZnO and SnO_2 films into thin-film transistors (TFTs) in 1968 and 1970 respectively, but poor electrical performances were observed as shown in Figure 1.1.^{[6],[7]} Until 2003, Nomura *et al.* suggested the use of single crystal $\text{InGaO}_3(\text{ZnO})_5$ (IGZO) for TFT material. High field-effect mobility of $80 \text{ cm}^2\text{V}^{-1}\text{s}^{-1}$ was achieved,^[8] which proved that high performance TFTs can be realized by oxide-based semiconductors. In the following year, Nomura *et al.* demonstrated fully transparent TFT on flexible substrate made by amorphous IGZO fabricated by pulsed laser deposition (PLD) as shown in Figure 1.2.^[9] Although the device performance is inferior than single crystal IGZO TFT, the field-effect mobility of amorphous IGZO TFT is still as high as $9 \text{ cm}^2 \text{ V}^{-1}\text{s}^{-1}$ which was explained by the unique conductive pathways formed by the overlap of the outer vacant s-orbitals of heavy metal cations (In^{3+}). Because s-orbitals are isotropic and insensitive to structural disorder or bond angle variation, the

field-effect mobility is not severely degraded in amorphous structure. In recent years, amorphous MO materials have been widely employed in electronic products, especially in flat panel displays.^[10] Amorphous MOs have several advantages over their crystalline counterparts in device fabrication such as low-temperature deposition, lack of grain boundaries which cause difficulties in etching and large-area uniformity.^[11] Besides used in TFTs, MO semiconductors have also been employed in various p–n junction devices as n-type materials and organic solar cells as charge-extracting interfacial layers.^{[12],[13]} In addition, because the conductivity of MO semiconductors can be affected by electron-hole pairs generated by photoirradiation and charge trapping/detrapping induced by chemisorbed molecules, MO semiconductors are promising sensing materials for photodetectors, gas sensors and biochemical sensors.^[14,15,16] Furthermore, MO-based resistive random access memories (RRAMs) have caught a lot of attention in recent years because of their low power consumption and high speed.^[17] The memory effect was explained by oxygen ion migration in MOs and strongly relies on the concentration of oxygen vacancies in MOs.

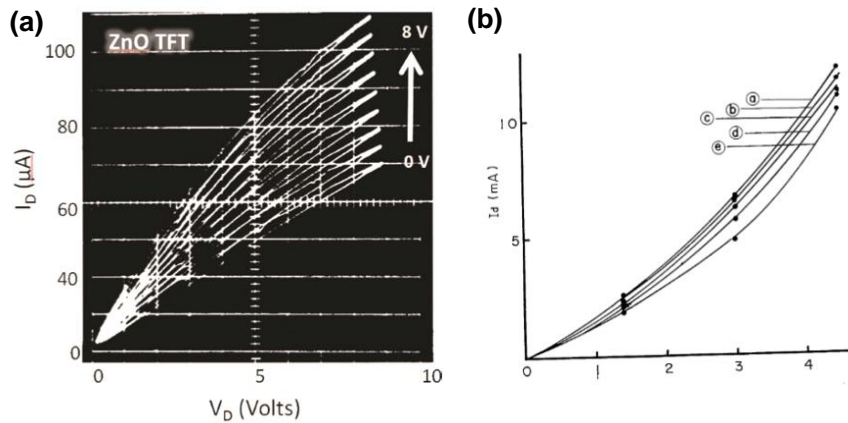


Figure 1.1. (a) I_D - V_D characteristics of Li-doped ZnO TFT. (b) I_D - V_D characteristics of SnO₂ TFT. (gate voltage: a: 0V, b: 2V, c: 4V, d: 6V, e: 10V) (Adapted from Ref. [6],[7])

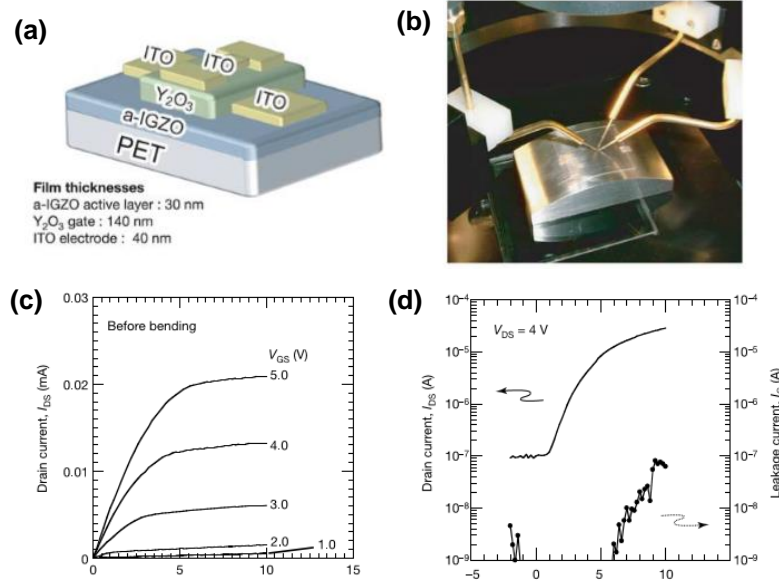


Figure 1.2. (a) The device structure of amorphous IGZO TFT. (b) A photograph of flexible IGZO TFT bent at $R = 30\text{mm}$. (c) I_D - V_D and (d) I_D - V_G characteristics of flexible IGZO TFT. (Adapted from Ref. [9])

It is fascinating that the optical, electrical properties of MOs can be modulated by mixing or doping. For example, as shown in Figure 1.3, the field-effect mobility and turn-on voltage of IGZO TFT can be tuned by changing the ratio of each components in the ternary system.^[18] Hyun-Suk Kim *et al.* has shown that optical bandgap and mobility of ZnO can be modulated by N doping.^[19] In addition, the conductivity of In_2O_3 and ZnO can be significantly improved by impurity-doping.^{[20], [21]} Highly conductive and transparent MO materials such as Sn-doped In_2O_3 and Al or Ga-doped ZnO can be used as electrode for various electronic devices.^[22] Furthermore, magnetic properties can be introduced into MO materials by doping transition metal ions.^[23] Figure 1.4 summarizes the material properties potential applications of MO materials, which shows MO materials play important roles in a wide range of science and technology.

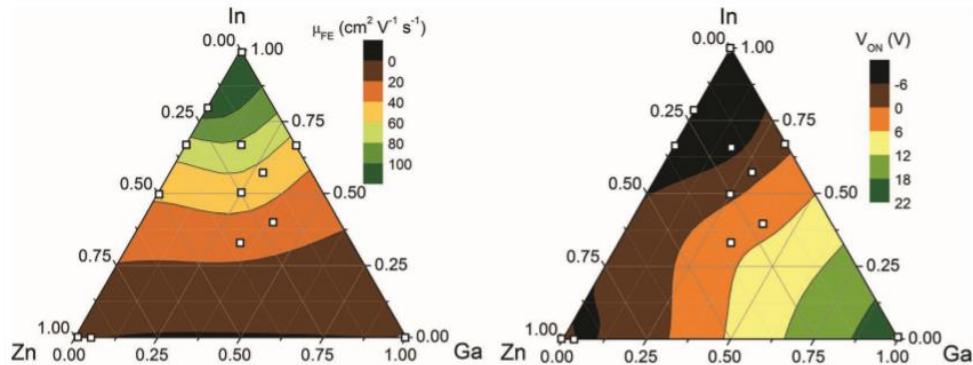


Figure 1.3. Variation of field-effect mobility and turn-on voltage of IGZO TFTs with different compositions. (Adapted from Ref.[18])

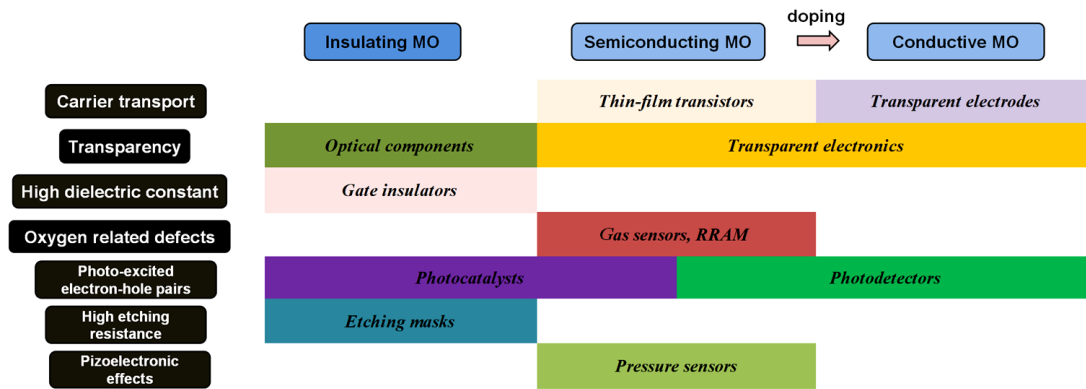


Figure 1.4. Summary of material properties and applications of MO materials.

1.1.2. Metal oxide thin film deposition

Various methods have been used to deposit metal oxide films. They can be categorized into two main categories: vapor-phase techniques and solution processing techniques. Vapor-phase techniques include thermal deposition, magnetron sputtering, pulsed-laser deposition and atomic layer deposition. Solution processing techniques include spin-coating, dip-coating and spray pyrolysis. These techniques generally require the preparation of a precursor solution by sol-gel reactions.

The details of the main deposition techniques are described in the following, and we discuss the advantages and drawbacks of these techniques.

1.1.2.1 Vapor-phase deposition

Thermal evaporation:

The source material is fed onto a semi-metal evaporator in vacuum and then electric current is induced to flow through evaporator to be heated up until the material start to evaporate to the substrate as shown in Figure 1.5. Thermal evaporation is also used to deposit high purity MO thin film with well-controlled deposition rate. However, because the evaporation procedure may also change the oxygen content in MO materials due to the escape of O_2 , the oxygen content adjustment is required after evaporation. In addition, to optimize the reactions between ionized species during deposition, substrate heating is necessary, which prevents the use of plastic substrates with low heat resistance. Moreover, the power consumption is large and costly.

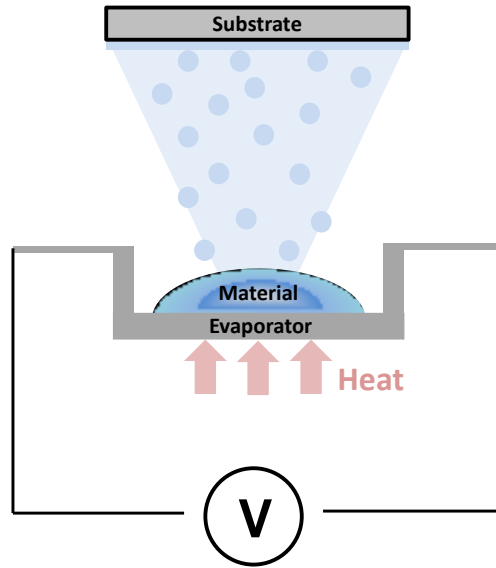


Figure 1.5. Schematic showing thermal evaporation deposition.

Magnetron sputtering:

Magnetron sputtering is the most widely used technique in industry for fabricating large scale MO films. The system of magnetron sputtering is illustrated in Figure 1.6, which consist a cathode, strong magnets and a MO target. As the chamber is pumped into high vacuum, argon gas is introduced into the vacuum chamber. After applying voltage bias to the cathode, the plasma gas is generated and ionized gases. Positively charged gas ions (Ar^+) are accelerated to the cathode and make bombardments to the target, which leads to MO vapor release from the target and coat on the substrate. The magnets under the target are used for enhancing the ion bombardment near the surface of the target. Compared to other deposition techniques, magnetron sputtering has the advantages such as room-temperature deposition which is compatible for thermally sensitive substrates, controllable morphology of MO materials from amorphous to crystalline and large area uniformity.

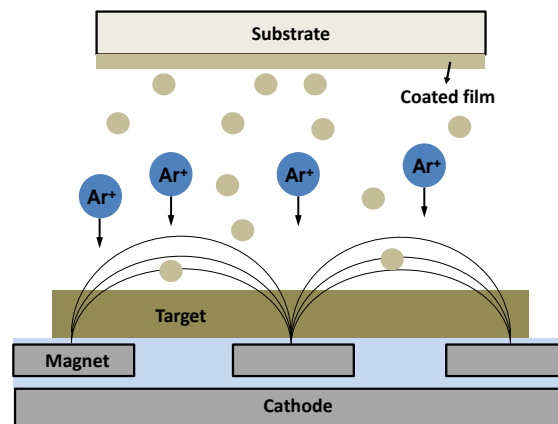


Figure 1.6. Schematic showing the magnetron sputtering deposition.

Pulsed Laser Deposition (PLD):

Figure 1.7 illustrates system of pulsed laser deposition. By irradiating a target with a high power pulsed laser beam, MO material on the target can be vaporized and deposit on the substrate. The process can be done in high vacuum or in O₂ environment. Although PLD is able to fabricate high quality MO films, it has some limitations such as large-area uniformity and high cost.

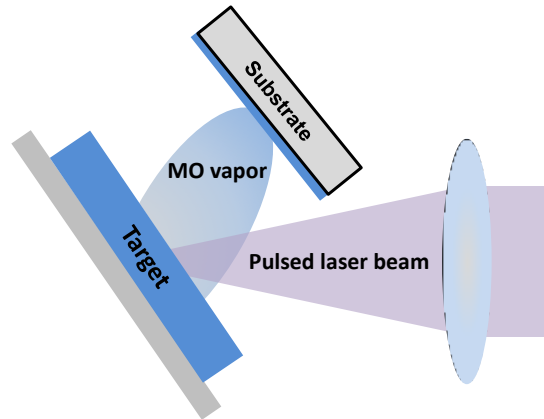


Figure 1.7. Schematic showing the PLD deposition.

Atomic Layer Deposition (ALD):

As shown in Figure 1.8, atomic layer deposition is a layer-by-layer growth technique by introduce different reagents into the chamber in cycles. The growth mechanism of ALD are governed by surface interactions. Reagents flow into the chamber in different deposition cycles, so they don't coexist at the same time, which avoids nucleation and crystallization and allows atomic-scale growth of high quality MO films on large and complex surfaces; however, the technique suffers from long reaction time and slow deposition rate.

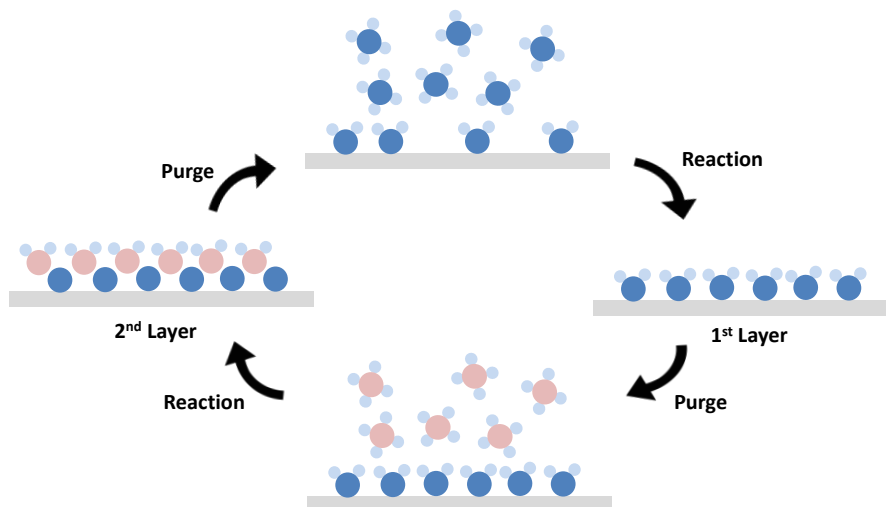


Figure 1.8. Schematic showing the ALD deposition process.

1.1.2.2 Solution Processing

Solution processing for MO thin film preparation has been proposed, with a major interest of considerably simplifying the process and the complexity of experimental setups, keeping the versatility of compositions of MO and equivalent properties. There are three major steps for depositing metal oxide thin-films via solution processing, which are (i) synthesis of metal oxide solution by sol-gel process, (ii) coating and (iii) thermal annealing. Each process step is discussed as follows.

(i) Synthesis of metal oxide precursor solution

Metal oxide precursor solutions are prepared by dissolving inorganic salts such as nitrates, chloride and hydroxide or organic salts such as alkoxides, carboxylates in proper solvents. After dissolution of metal salts in solvent, the precursor solution usually stirred vigorously for more than 24 hours to reach stabilization of precursor solution. During this aging period, precursor solutions undergo a slow transformation, known as sol-gel process. In a salt-water-alcohol system, the transformation can be described as following steps: (i) hydrolysis reactions with water molecules in the solution; (ii) condensation and dehydration; (iii) nucleation; and (iv) growth of metal oxide particles. The speed of the transformation is related to many factors such as the intrinsic property of precursors, solution concentration, PH value, amount of water and aging time. Sometimes precipitation occurs in solution due to rapid growth of oxide particles and particle-particle aggregation. To avoid precipitation, complexing agents such as ethanolamine (MEA) are added into solutions. The -OH group in MEA can coordinate with metal cations in alkoxides, improving the solubility and stability of precursor. Figure 1.33 illustrated chemical equilibrium reactions between zinc acetate, water and MEA proposed by Lamia Znaidi.^[67] The Zn-oxo particles are formed by the hydrolysis-condensation reactions between Zn^{2+} ions and OH^- ions. As mentioned before, the speed of hydrolysis-condensation reactions is decreased due to the interaction between Zn^{2+} and organic complexes such as MEA and acetate which also compete for Zn^{2+} in solution. As shown in Figure 1.33, the ZnO particle is protected by the acetate molecules, which prevent particle-particle aggregation. The particle size and concentration can be observed by absorption spectrum. For instance, Figure 1.34a shows time-dependent absorption spectra of $ZnCl_2$ solution composing $ZnCl_2$, H_2O , ethanol and NaOH.^[68] Clear absorption bandgaps in the spectra indicates the existence of ZnO particles in the $ZnCl_2$ solution. The absorption maximum (A_{max}) increases with the increase of aging time (Figure 1.34b), implying the number of ZnO nanoparticles increased with time. The absorption maximum became stable after aging for 50 minutes, implying the number of ZnO particles stop increasing. The $\lambda_{1/2}$ and λ_g indicated in the spectrum correspond respectively to wavelength at half of the absorption maximum and absorption edge which gradually

increase with the aging time as shown in Figure 1.34c, suggesting ZnO particles in solution grew bigger with time.

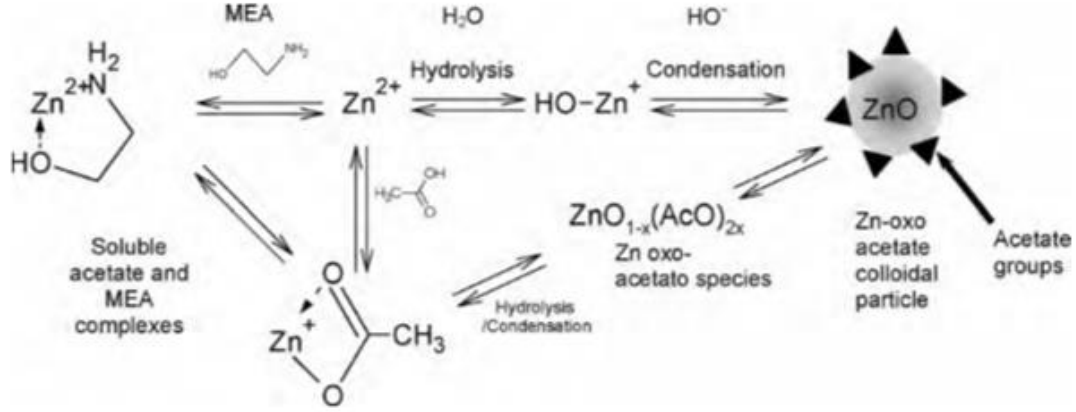


Figure 1.33. Schematic showing the chemical equilibrium taking place in a ZnO precursor solution. (Adapted from Ref. [41])

The distribution of particle size ($N(r)$) can be estimated by differentiating of absorption intensity (A) with particle radius (r) as the following equation.^[68]

$$N(r) \propto \frac{dA(r)}{\frac{4}{3}\pi r^3} \quad (\text{equation 1.1})$$

$A(\lambda)$ obtained from the absorption spectrum can be changed to $A(r)$ by equation 1.6, where E_g is the bandgap corresponding to the absorption wavelength λ , E_g^{bulk} is the bandgap of ZnO, h is plank constant, m_0 is the electron rest mass, m_e and m_h are the effective electron and hole masses, ϵ is the dielectric constant of ZnO and ϵ_0 is the permittivity of vacuum.^[68]

$$\Delta E_g = E_g - E_g^{bulk} = \frac{h^2}{8\epsilon r^2} \left(\frac{1}{m_e m_0} + \frac{1}{m_h m_0} \right) - \frac{1.8e}{4\pi\epsilon\epsilon_0 r} \quad (\text{equation 1.2})$$

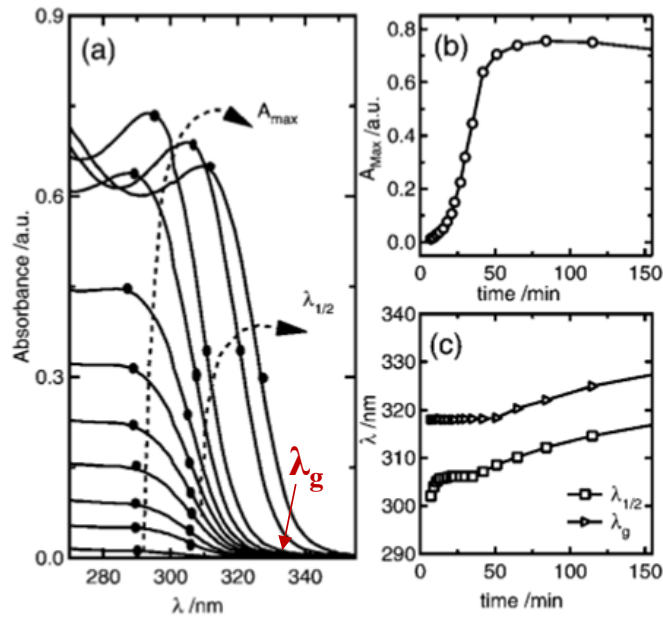


Figure 1.34. (a) The time-dependent evolution of absorption spectra of a ZnCl_2 precursor solution. A_{\max} and $\lambda_{1/2}$ correspond to the absorption maximum and the wavelength at the half of absorption maximum respectively. (b) The evolution of A_{\max} versus time. (c) The evolution of $\lambda_{1/2}$ and λ_g (absorption edge) versus time. (Adapted from Ref.[68])

(ii) Thin film coating from solution

Spin coating:

Spin-coating is a simple method for preparing homogeneous films on flat substrate from solutions. The schematic of a spin-coater is shown in Figure 1.9. Precursor solution was first deposited on the surface of the substrate that is attached to the spin-coater. After fast-speed rotation, excess solution is removed from the substrate by centrifugal force, leading to the formation of a uniform gel-film on the substrate. The thickness of spin-coated film is related to the viscosity of precursor solution and the spinning-speed. Acceleration and spinning duration are also parameters to control to obtain reproducible results.

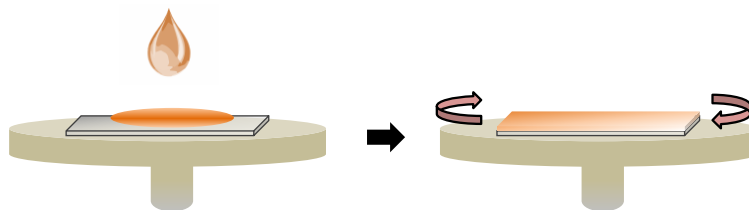


Figure 1.9. Schematic showing spin-coating procedure.

Dip-coating:

Dip-coating technique is suitable for covering both side of the substrate with flat or irregular shape of surface. The procedure of dip-coating is shown in Figure 1.10. The substrate is firstly immersed into a pool of precursor solution and then drawn out with controlled rate. Although it has been known that the thickness of the coated film can be controlled by the withdrawal speed, the mechanisms of thin-film formation is still under investigation.

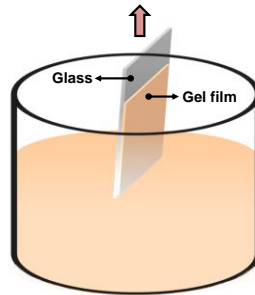


Figure 1.10. Schematic showing dip-coating procedure.

Spray pyrolysis:

As shown in Figure 1.11, in spray pyrolysis the MO film is deposited by spraying MO precursor solution on the substrate. Air blasting or ultrasonic method/electronic methods are used in the sprayer to spray the precursor solution. The technique is inexpensive and suitable for large-area and rapid deposition, which is particularly useful and has been employed in industry for fabricating conductive MO materials on glass. However, spray-coated films are more porous and uniform in comparison to spin-coated films, which required further optimization of process parameters.

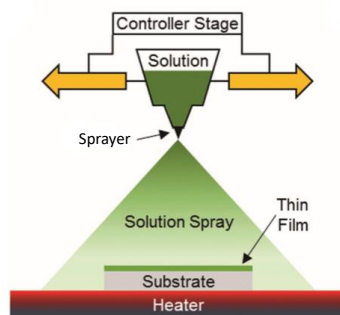


Figure 1.11. Schematic showing the system of Spray pyrolysis. (Adapted from ref. [24])

(iii) Thermal annealing

Thermal annealing has several objectives: First, thermal annealing is necessary to completely decompose organic species embedded in precursor films (from precursor, complexant agent and

solvent). In thin film, this usually occurs at relatively low temperatures ($T=150$ to 250°C). Secondly, after low temperature annealing, porous structures with high concentration of hydroxide functions (M-OH) are generated. Such functions are usually defects for the final properties (especially electrical properties). For some applications, crystallinity is required and thermal annealing is also required to obtain the suitable crystalline phase. So high-temperature thermal annealing ($T > 300^{\circ}\text{C}$) is required as a final step. However, annealing at high temperature may cause deformation of glass substrate and melting or burning of substrates with low heat resistance such as plastic foils, metal foils, papers and textiles.

Deposition of metal-oxide films at low temperature ($< 300^{\circ}\text{C}$) via solution processing is thus a research topic that has drawn a lot of attention in recent years and several research groups have successfully converted metal oxide precursors to oxide films by using low-temperature annealing. In 2011, Myung-Gil Kim *et al.* used a self-energy generating combustion chemistry method which effectively lowers the annealing temperature to $\sim 200^{\circ}\text{C}$ for fabricating indium zinc oxide (IZO) films.^[25] By mixing oxidizers ($\text{In}(\text{NO}_3)_3 \cdot 2.85 \text{H}_2\text{O}$ and $\text{Zn}(\text{NO}_3)_2 \cdot 6 \text{H}_2\text{O}$) and fuel (acetylacetone or urea), local heating can be generated, which facilitates the conversion of IZO precursor to IZO films. In the same year, K.K.Banger *et al.* proposed a 'sol-gel on chip' method that alkoxide precursors can be transformed into metal oxide films by annealing in water vapor at low temperatures ($< 250^{\circ}\text{C}$).^[26] The low-temperature conversion of metal oxide precursors was due to the enhanced hydrolysis condensation reactions in water vapor.

1.2. Direct-patterning techniques for metal oxide precursor

For many applications, metal oxide micro- and nanopatterns are required. Conventional photolithography, as shown in Figure 1.12a, is usually adopted to obtain oxide films to micro- or nanoscale dimension. Recently, various solution-based direct-patterning techniques have been developed such as micromolding,^[27] selective surface wetting,^[28] inject-printing,^[29] and photopatterning.^[30] As shown in Figure 1.12b, in comparison to conventional photolithography, direct-patterning techniques have fewer process steps and avoid using toxic chemical etching and photoresists, which is more efficient and environmental friendly. Moreover, etching of metal oxide is usually relatively difficult to control. In the following sections, we will introduce several important direct-patterning techniques.

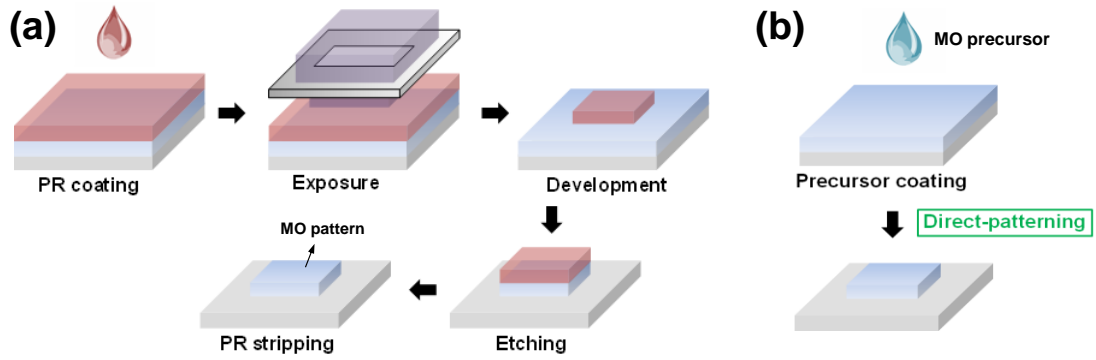


Figure 1.12. Schematic showing the processes of (a) conventional photolithography and (b) direct-patterning.

1.2.1. E-beam writing

It has been known that precursors with long-chain hydrocarbons can be polymerized by e-beam irradiation.^[31] For example, zinc naphthenate ($C_{22}H_{14}O_4Zn$) can be polymerized via e-beam irradiation because of the crosslinking at $-C=O$ and/or $-(CH_2)_n-$, which makes the zinc naphthenate insoluble in developer just as a negative tone resist.^[32] M. S. M. Saifullah *et al.* have demonstrated ZnO nanostructures by using zinc naphthenate as precursor and e-beam direct-writing.^[19,32] Figure 1.13(a) illustrates the process of e-beam direct-writing. Figure 1.13(b) shows sub-10 nm zinc naphthenate structures written by e-beam. After thermal annealing (500 °C for one hour), organic compounds in the zinc naphthenate structures were removed, leading to the formation of ZnO nanostructures of ~5 nm line-width. (Figure 1.13(c)) Resolution of e-beam at the nanoscale makes this technique with no equivalent when high resolution is the most important feature. However, this technique is limited to the fabrication of very small objects on limited area due to very long writing times required for bigger structures.

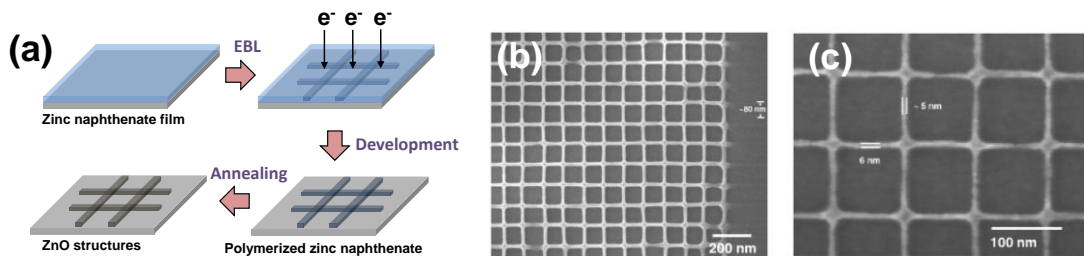


Figure 1.13. (a) Schematic showing ebeam lithography processes. The SEM images of e-beam-written zinc naphthenate structures before (b) and after (c) thermal annealing. (Adapted from Ref. [32])

1.2.2. E-jet printing

The schematic of the e-jet printing system is illustrated in Figure 1.14a.^[33] Ink (metal oxide precursor) is delivered from a reservoir to a metal nozzle by pressure controller, forming a pendent hemispherical shape liquid drop. By applying a DC voltage bias between the metal nozzle and substrate, ink can be ejected on the substrate. S.-Y. Kim *et al.* has patterned In_2O_3 films by using e-jet printing.^[34] Indium nitrate hydrate was used as precursor. The authors showed that thickness of the film can be increased by increasing the number of printing passes. In the article, the smallest line-width achievable by e-jet printing is $2\ \mu\text{m}$ as shown in Figure 1.14b. After annealed on a hotplate at $250\ ^\circ\text{C}$ for 150 minutes in air, these e-jet-printed patterns were converted to In_2O_3 films which can be integrated into TFTs and showed excellent electrical performance with high field-effect mobility $\sim 230\ \text{cm}^2/\text{Vs}$ and on-off ratio $\sim 10^7$.

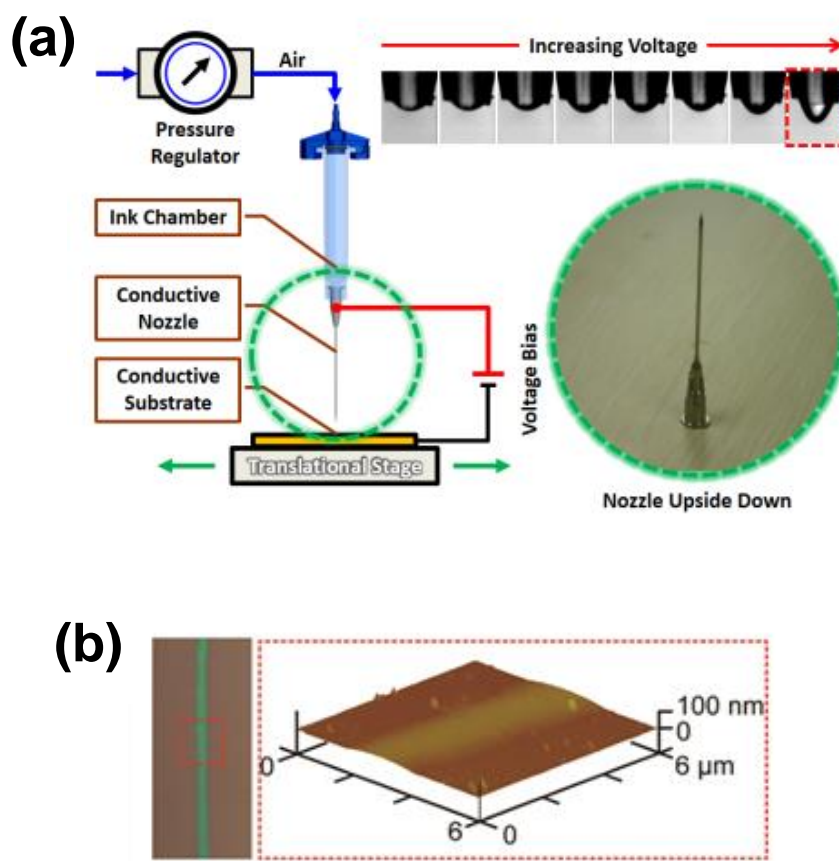


Figure 1.14. (a) Schematic showing the e-jet printing system (b) e-jet printed In_2O_3 lines of $2\ \mu\text{m}$ line-width.

(Adapted from Ref. [33], [34])

1.2.3. Micromolding

The schematic of the micromolding procedure is shown in Figure 1.15a. PDMS mold was first placed on precursor solution pool with patterned side down. Due to capillary forces, solution is drawn into the channels and formed patterned thin films after dried. Figure 1.15b shows high resolution $\text{Pb}(\text{Zr}_{0.52}\text{Ti}_{0.48})\text{O}_3$ (PZT) lines from 2 μm to 10 μm fabricated by micromolding demonstrated by C. R. Martin.^[27] However, in comparison to other techniques which can form isolated patterns easily, micromolding usually suffers from residue layer due incomplete removal of excess liquid underneath the protruding parts of the mold. In addition, it is time consuming for pattern transformation and mold preparation, which prevents micromolding from being adopted for large area manufacturing process.

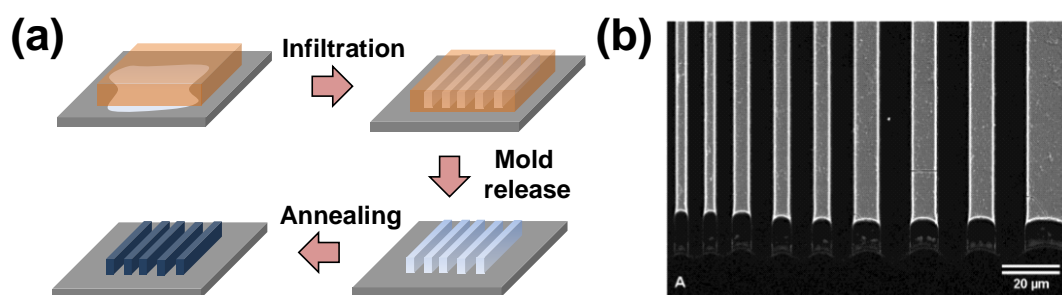


Figure 1.15. (a) Schematic showing the micromolding procedure (b) PZT lines fabricated by micromolding.

(Adapted from Ref. [27])

1.2.4. Selective surface wetting

Finally, we introduce direct-patterning via selective surface wetting. The method has been successfully used to pattern IGZO precursor.^[28] The fabrication procedure was shown in Figure 1.16. A thin hydrophobic self-assembled layer (n-Octadecyltrichlorosilane, OTS) was grown on SiO_2 substrates by immersing the substrates in OTS solution for 30 minutes. Then, the OTS layer was patterned by O_2 plasma etching through a shadow mask with $1.2 \times 1.2 \text{ mm}^2$ opening. The regions with OTS layer are hydrophobic and the regions without OTS are hydrophilic. After hydrophilic IGZO solution was spin-coated on the substrate, the solution was repulsed by hydrophobic surface and flowed into hydrophilic regions, forming IGZO precursor patterns which can be converted to IGZO patterns after thermal annealing at 350 $^\circ\text{C}$ for 90 min in ambient conditions. Besides patterning semiconducting IGZO films, the method can also be applied to pattern insulating AlO_x films as dielectric layer for TFTs. The IGZO TFTs patterned by selective surface wetting exhibited good electrical properties of

field-effect mobility $\sim 0.94 \text{ cm}^2/\text{Vs}$, threshold voltage 90 mV, on-off ratio 10^5 , and subthreshold swing 122 mV/decade. Moreover, Yuzhi Li *et al.* have shown that selective surface wetting can avoid precursor spreading during the inject-printing.^[29]

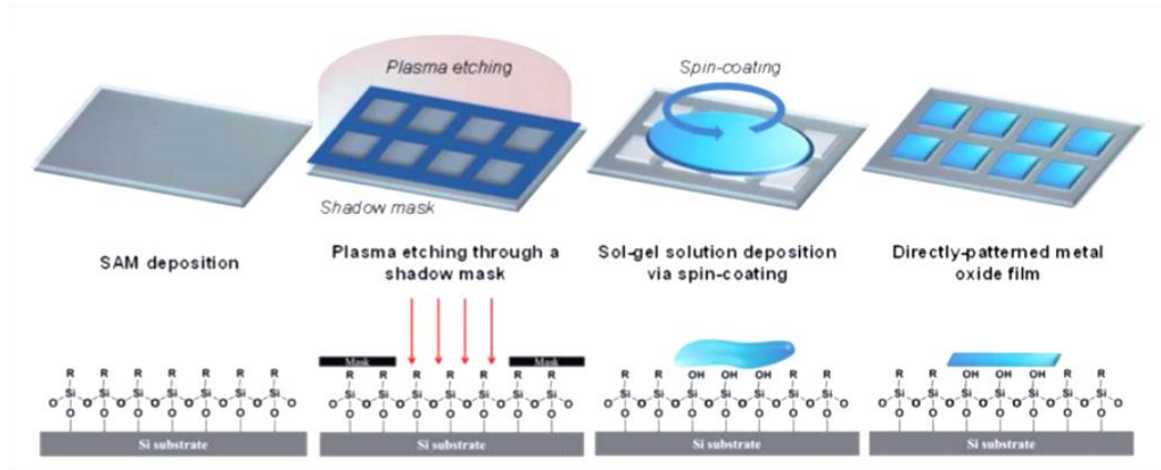


Figure 1.16. Schematic showing direct-patterning of metal oxide films via selective surface wetting. (Adapted from Ref. [28])

1.3 Photo-induced patterning

1.3.1. Interest of photopatterning

Various kinds of photosensitive organic materials which can be decomposed (positive tone photoresist) or crosslinked (negative tone photoresist) by photoirradiation have been widely used in the conventional photolithography process for pattern transfer. With the progress of optical system and material properties, the feature line-width of photo-patterned organic resist can be down to a few nanometers. If metal oxide precursors can be crosslinked or dissolved just like organic photoresist, they are expected to form fine metal oxide structures in more easy and efficient way than other techniques which uses molding, shaping or printing to form patterns, because the intensities of light and irradiated regions are well-controlled by modern semiconductor technologies for pattern transfer. Furthermore, since photolithography systems are commonly used in industry, it is expected that photo-patterned metal oxide structures can be integrated into various semiconductor devices directly without purchasing new tools or machines. Before adopting photolithography to pattern metal oxide precursor, it is necessary to first understand the photo-induced chemical reactions in photosensitive metal oxide precursors, which will be discussed in the next section.

1.3.2. Photo-induced crosslinking and decomposition of organic species in photosensitive metal oxide precursor

Recently, various photosensitive metal oxide precursors have been developed. It was discovered that two reactions can take place in metal oxide precursor under photo-irradiation : i) crosslinking reaction and ii) decomposition of embedded organic species.

In 2012, Yong-Hoon Kim *et al.* developed a photosensitive indium gallium zinc oxide (IGZO) precursor.^[35] The precursor was synthesized by mixing $\text{In}(\text{NO}_3)_3 \cdot x\text{H}_2\text{O}$, $\text{Ga}(\text{NO}_3)_3 \cdot x\text{H}_2\text{O}$, and $\text{Zn}(\text{CH}_3\text{CO}_2)_2 \cdot 2\text{H}_2\text{O}$ together in 2-methoxyethanol. Under UV irradiation, hydrolysis-condensation reactions occurred, leading to the formation of M-O-M networks. Furthermore, carbon species in the-gel films can be completely removed after 30 minutes UV irradiation without additional thermal treatment. The authors suggest that photochemical cleavage of alkoxy groups in the metal oxide precursor is responsible for the formation of M-O-M networks and removal of embedded organic species. However, the authors also suggest that only photoirradiation might not be sufficient to completely remove organic compounds. Although the IGZO precursor can be directly converted to IGZO film after long-time photoirradiation (photo-annealing) and exhibited good electrical properties in electronic devices, it was found that an unintentional thermal heating up to 150 °C occurred during photoirradiation. In addition, poor electrical properties were observed if the unintentional heating was eliminated by performing photo-annealing on a cooling stage, which implies that a lot of organic compounds still embedded in the oxide films and hindered carrier transport. The photo-induced decomposition of organic species was not investigated deeply in this study. An in-depth study of photo-annealing in metal oxide precursors was carried out by Sungjun Park *et al.* in 2015.^[36] The authors suggest that the M-O-M crosslinking and the decomposition of organic species are due to the OH radicals created by the photodecomposition of nitrate salt in the precursor as the following equation.



OH radicals can mediate the reactions of condensation and decomposition of organic species as shown in Figure 1.17. The DUV irradiation accompanied with a moderate heating (150 °C) was found to be the most efficient way to eliminate organic impurities in the oxide films. These results indicate that nitrate salts are promising candidates for the preparation of metal oxide precursors which can be

converted to metal oxide films by using photo-irradiation accompanied with low-temperature thermal annealing.

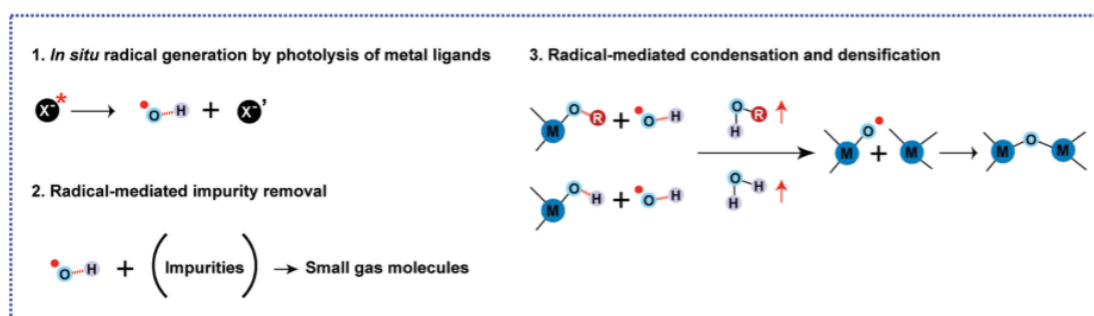


Figure 1.17. Physicochemical mechanism of the low-temperature decomposition of embedded organic compounds and formation of metal oxide films proposed by Sungjun Park *et al.*. (1. direct photodecomposition of impurities. 2. *in situ* radical formation. 3. enhancement of rapid condensation and densification). (Adapted from Ref. [36])

Photo-induced decomposition of organic species may also be related to the metal cations of precursors. Fabrice Stehlin *et al.* have studied the photochemical conversion of methacrylate (MAA) modified zirconium, hafnium and titanium tetraisopropoxide.^[37] It was discovered that under DUV irradiation, MAA ligands were rapidly decomposed in titanium precursor, leading to the formation of TiO₂ thin films at room temperature. In contrast, only a little amount of MAA ligands were decomposed in zirconium and hafnium precursors after a long-time DUV irradiation; thus, a high-temperature thermal annealing (> 400 °C) is required for the removal of organic compounds in zirconium and hafnium precursors. The difference in organic ligand (MAA) decomposition might be related to metal cations (titanium, zirconium and hafnium) in precursors but is still unclear, which could be important for the development of metal oxide precursors convertible at room temperature via photo-irradiation. It's noteworthy that room-temperature decomposition of organic species in titanium-based precursor was also investigated by Patrick C. With *et al.*^[38] Titanium (IV) ethoxide was used to prepare precursor. Same with MAA-modified titanium tetraisopropoxide, titanium ethoxide is able to be converted to TiO₂ film completely via UV irradiation at room temperature. The authors suggest that Ti-OCO-ring was formed as intermediate compounds during photochemical conversion. However, no further discussion in terms of the relation between the room-temperature organometallic decomposition and the formation of Ti-OCO-ring structure was presented in the article.

Although many studies reported the observation of low-temperature photo-induced solidification and decomposition of organic compounds embedded in metal oxide precursors, the mechanism is still

unclear. Only a few works have made a comprehensive investigation to the photochemical conversion and characterized the intermediate compounds generated by decomposition of metal oxide precursors. More investigations are required to have in-depth understanding of photochemical conversion of metal oxide precursors, which is important for establishing a general rule for preparing metal oxide precursors that can be completely converted to metal oxide films only by photoirradiation.

1.3.3. Photopatterning of metal oxide precursor as negative tone resist

As mentioned in previous section, M-O-M crosslinking can be generated in photosensitive metal oxide precursor via photo-irradiation. It was discovered that crosslinked precursors have a much lower solubility in polar solvents such as ethanol, 1-propanol and cyclohexanol compared to non-crosslinked precursor. Non-irradiated precursor can be washed away, leaving photo-irradiated regions (photo-crosslinked regions) on the substrate by using polar solvents. The behavior of metal oxide precursor is therefore just like a negative tone photoresist. The molecular size of metal oxide precursors makes them suitable for nanoscale lithography.

Various kinds of photosensitive metal oxide precursors have been proposed with different molecular structures. Generally, the molecule structure of photosensitive metal-oxide precursors contains chelating bonds connecting to the metal cations which can be prepared by mixing nitrate salts or alkoxides precursors and photosensitizers such as acetylacetone or benzoylacetone. As shown in Figure 1.18, the chelating bonds are formed automatically between nitrate salts and photosensitizers when they are mixed together.^{[39],[40]} Carboxylic acids are also known to form stable complexes with metal cations. Another way to prepare photosensitive precursors is to use organic salts which have chelating ligands in their molecular structures such as zinc acrylate, zinc methacrylate.^{[41],[42]}

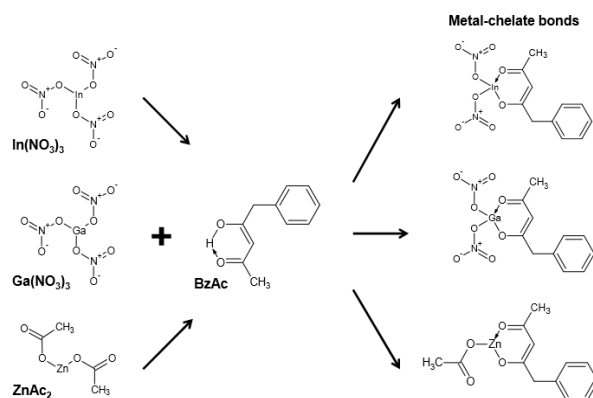


Figure 1.18. Formation of metal-chelate bonds between metal precursors and benzoylacetone (BzAc). (Adapted from Ref. [30])

The procedure of photopatterning is illustrated in Figure 1.19. Photosensitive metal oxide precursor was first coated on the substrate then prebaked for a few minutes to remove excess solvent. The gel-film is then exposed to UV light through a photomask. In irradiated regions, crosslinking occurs in the precursor due to partial or complete cleavage of chelating organic ligands. After exposure, the gel-film is dipped into developer and the precursor in non-exposed regions are removed. To completely remove organic compounds embedded in metal oxide films, a thermal annealing is usually required as a final step.

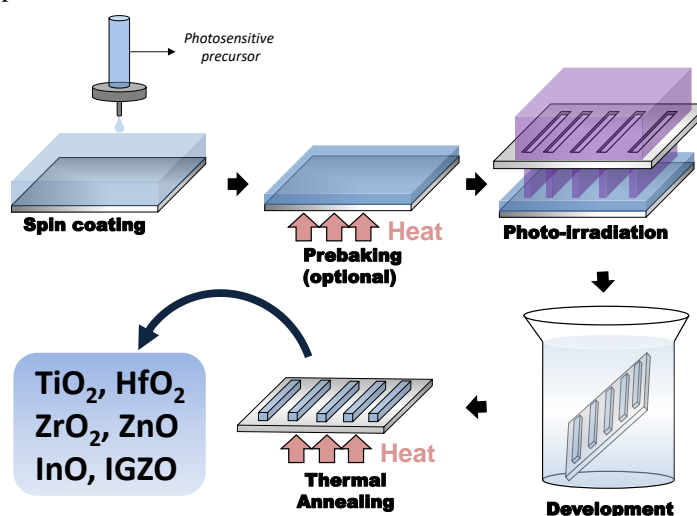


Figure 1.19. Schematic showing the photopatterning procedure.

Photopatterning of IGZO precursor with microscale dimensions was demonstrated by You Seung Rim *et al.* in 2013. Benzoylacetone (BzAc) was added into metal oxide precursor to enhance the photosensitivity.^[30] Under UV-irradiation, due to the π to π^* transition, chelated BzAc rings were cleaved from metal cations, which gives rise to crosslinking reactions as shown in Figure 1.20a. However, an additional thermal treatment at 350 °C was required in order to completely remove embedded organic species. The smallest line-width demonstrated in this study is 10 μm . (Figure 1.20b)

In recent years, many researches are devoted to reduce the line-width of photo-patterned metal oxide structures which may have various applications in nanoscale electronic and optical devices. Table 1.1 shows the feature line-widths of photo-patterned metal oxide structures demonstrated by different groups. From Table 1.1, we can see that the line-widths are related to the wavelength of light sources. As expected, shorter wavelength can pattern smaller structures, because the diffraction effects can be decreased with the decrease of wavelength. The smallest line-width was ~10 nm made by using EUV lithography ($\lambda = 13.5$ nm) and zinc naphthenate photoresist.

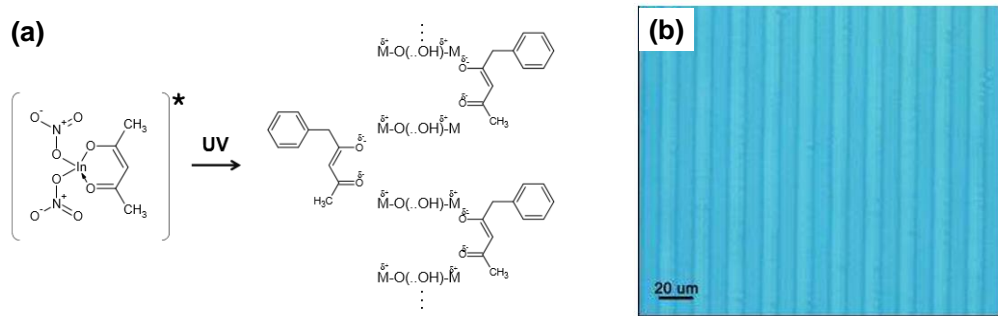


Figure 1.20. (a) Photo-induced crosslinking and cleavage of metal-chelate bonds. (b) Photo-patterned IGZO lines of 10 μm line-width. (Adapted from Ref. [30])

Table 1.1 minimum feature line-width of metal oxide patterns formed by photosensitive metal oxide precursors and DUV or EUV lithography.

Material	Precursor	Photosensitizer	line-width	Wavelength	Annealing temperature	Ref.
ZnO	zinc diacrylate	—	20 μm	254 nm	450 $^{\circ}\text{C}$	11
ITO	$\text{In}(\text{NO}_3)_3 \cdot x\text{H}_2\text{O}, \text{SnCl}_2$	benzoylacetone	5 μm	365 nm	500 $^{\circ}\text{C}$	12
IGZO	$\text{In}(\text{NO}_3)_3 \cdot x\text{H}_2\text{O}, \text{Ga}(\text{NO}_3)_3 \cdot x\text{H}_2\text{O}, \text{Zn}(\text{NO}_3)_2 \cdot x\text{H}_2\text{O}$	acetylacetone	3 μm	184.9 nm	200 $^{\circ}\text{C}$	13
IGZO	$\text{In}(\text{NO}_3)_3 \cdot x\text{H}_2\text{O}, \text{Ga}(\text{NO}_3)_3 \cdot x\text{H}_2\text{O}, \text{Zn}(\text{CH}_2\text{CH}_3\text{COO})_2$	—	300 nm	193 nm	300 $^{\circ}\text{C}$	14
ZrO_2	$\text{Zr}_4(\text{OCH}_3)_{16}$	methacrylic acid	100 nm	193 nm	500 $^{\circ}\text{C}$	15
ZnO	$\text{C}_{22}\text{H}_{14}\text{O}_4\text{Zn}$	—	10 nm	~ 13.5 nm	850 $^{\circ}\text{C}$	16
HfO_2	HfO_2 nanoparticles	—	30 nm	~ 13.5 nm	—	17

1.3.4. Photopatterning of metal oxide precursor as positive tone resist

In most reports, metal oxide precursors are used as negative tone resist in the photopatterning process. Only a few studies reported positive tone behavior of metal oxide precursors. Ober and Giannelis group at Cornell have investigated dual-tone behavior of metal oxide precursors and showed the feasibility of using metal oxide precursor as positive tone resist.^[43] By changing the developer to tetramethyl ammonium hydroxide (TMAH) and adding an additional post exposure baking (PEB) step, positive tone resist behavior were observed in metal oxide precursors. The authors suggested that photo-crosslinked oxo bridges in the exposed region are more soluble in TMAH than unexposed region which are protected by organic ligands (carboxylic acid), leading to a positive tone behavior. Figure 1.21(a) shows fine patterns formed by using ZrMAA precursor used as positive tone resist. Small patterns of ~ 250 nm line-width were demonstrated. The authors indicate PEB is an important step for the occurrence of positive tone behavior. Figure 1.21(b) shows the effect of PEB time on the ratio of the thicknesses of exposed and unexposed films, indicating increasing PEB time enhanced the positive tone behavior of metal oxide precursor.

It's noteworthy that Clotaire Chevalier-César *et al.* also reported the positive tone behavior of metal oxide material (ZnO) by using photodissolution method.^[44] As shown in Figure 1.22(c), under photoillumination in NaCl solution, electron hole-pairs are generated in the exposed region of ZnO film. Photo-excited holes (h^+) can replace Zn^{2+} in Zn-O-Zn network, leading to the emission of O_2 gas and release of zinc ions which later form $ZnCl_2$ molecules in the NaCl solution. The exposed region is therefore gradually dissolved in solution just like a positive tone resist. The authors demonstrated that by using a laser interference system, fine patterns of ~ 450 nm line-width can be obtained as shown in the OM (1.22(a)) and SEM images (1.22(b)). Furthermore, due to the enhanced charge separation, the dissolution speed can be accelerated by applying additional voltage bias to the ZnO film.

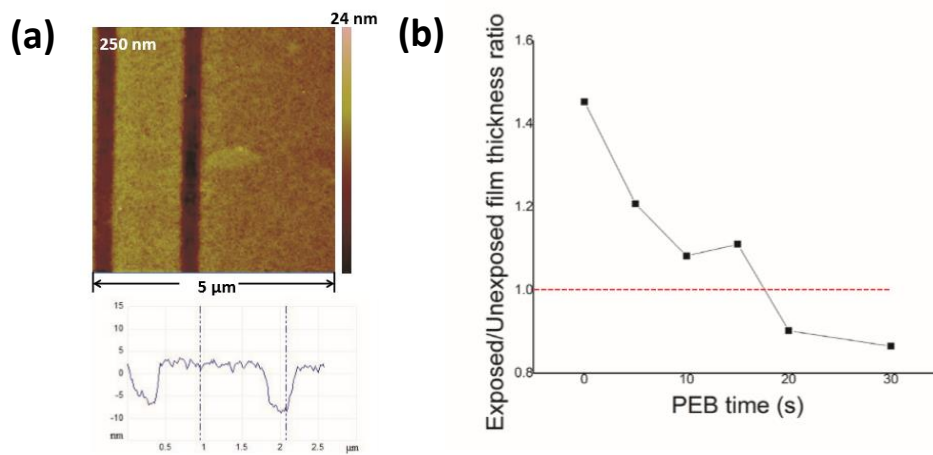


Figure 1.21. (a) ZrMAA patters of ~ 250 nm line-width patterned by DUV lithography as a positive tone resist. (b)The thickness ratio of exposed/unexposed ZrMAA resist films after developing by using 0.26N TMAH for 10 s. (Adapted from Ref.[43])

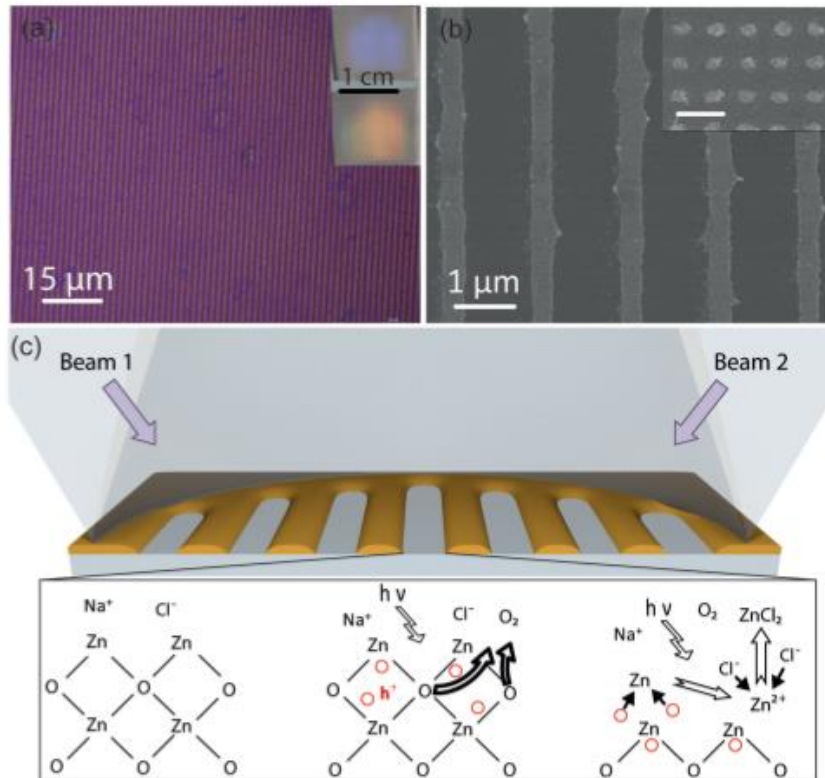


Figure 1.22. (a) OM image and (b) SEM images of ZnO lines patterned laser interference and photodissolution.. (c) Schematic showing the chemical reactions taking place in the photo-irradiation regions. (Adapted from ref.[44])

1.4. Applications of solution-processed metal oxide films and patterns

Solution processing and metal oxide precursors have been widely used to fabricate functional oxide films that can be integrated into various electro-optical devices such as TFTs, transparent electrodes, sensors, solar cells, optical filters etc.. As mentioned before, with proper modification of metal oxide solution, oxide films can be fabricated by using photopatterning techniques; however, besides TFTs, only a few reports demonstrated other functional devices with photo-patterned oxide films. In the following sections, the author will introduce several metal oxide devices which have been successful fabricated by solution-based techniques. The potential of using photopatterning to fabricate these devices warrant further investigation.

1.4.1. Thin-film transistors

Thin-film transistor (TFT) is a three terminal electronic device and the most basic component for driving displays. The common structures of TFT are shown in Figure 1.23a-1.23d. Under TFT operation, the source thermal (S) is applied 0 V ($V_s = 0V$) and a constant voltage V_D is applied to the

drain terminal (D). Current between source terminal and the drain terminal is control by gate terminal with voltage bias V_G . Figure 1.23e shows a typical transfer characteristic (drain current versus gate voltage) of n-type (the majority carriers are electrons) TFT. We can see that the device can be switched on, current flowing from source to drain, by increasing gate bias and switched off by decreasing gate bias. The mechanism is explained as follows. Under positive gate bias, electrons in the semiconductor layer can be accumulated at the semiconductor/insulator interface, which forms a conductive channel from source terminal to drain terminal. Therefore, the drain current (I_D) increases. An opposite behavior can be observed in p-type (the majority charge carriers are holes) transistor. The performance of TFT device can be evaluated by field-effect mobility (μ) and subthreshold swing (S.S.) which are shown in the following two equations.

$$\mu = \frac{L}{C_G W V_D} \left(\frac{\partial I_D}{\partial V_G} \right) \quad \text{(equation 1.4)}$$

$$S.S. = \frac{\partial V_G}{\partial (\log I_D)} \quad \text{(equation 1.5)}$$

μ is an important parameter for TFT devices, because using TFTs with high μ can reduce the power consumption. Under the same V_D , TFT with high μ exhibits higher drain current than TFT with low μ . The S.S. represents how effective a conductive channel forms under gate bias. It is highly related to the quality of semiconductor/insulator interface.

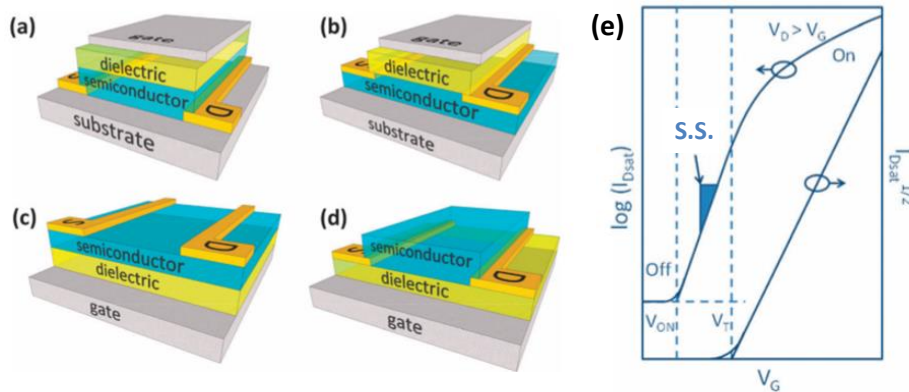


Figure 1.23. Common TFT device structures (a) staggered, top-gate; (b) coplanar, top-gate; (c) staggered, bottom-gate; and, (d) coplanar, bottom-gate. (e) Transfer characteristic of a n-type TFT. (Adapted from Ref. [45])

The first TFT device was demonstrated by Weimeer at RCA laboratory in 1962 as shown in Figure 1.24a. Later on 1979, W. F. Spear suggested the use of hydrogenated amorphous silicon (a-Si:H) for TFT devices, which revolutionized flat panel display technology. Until now, a-Si TFTs are still

widely used for driving active matrix LCDs. However, the field effect mobility of a-Si TFT is $< 0.5 \text{ cm}^2/\text{Vs}$ due to its anisotropic disorder covalent sp^3 bonding structure (Figure 1.24b). Localized trapping states are formed in the bandgap which affects carrier transport and decrease the field-effect mobility of a-Si TFTs. On the other hand, indium-based or tin-based amorphous metal oxide semiconductors such as indium zinc oxide (IZO), indium gallium zinc oxide, (IGZO), indium tin zinc oxide (ITZO), tin zinc oxide (TZO) have showed much higher field effect mobility ($> 10 \text{ cm}^2/\text{Vs}$) and better stability than a-Si TFTs, so they have been considered as promising candidates to replace a-Si for next generation LCDs and OLED displays. The high field-effect mobilities observed in amorphous metal oxide semiconductors is attributed to their electronic configurations which are insensitive to distortion of M-O-M bonds. As shown in Figure 1.24c, due to the overlapping of ns orbitals of heavy metal cations such as In^{3+} , Sn^{4+} , carrier transport is insensitive to structural disorder, which leads to high field-effect mobility in TFT operation. Electronic companies such as Samsung and Sharp have already launched several display products driven by metal oxide TFTs.

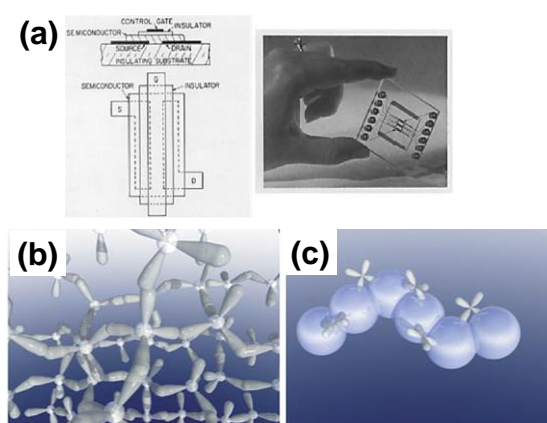


Figure 1.24. (a) The photograph of the first thin-film transistor. (b) Illustration of conduction paths in amorphous silicon and (c) amorphous metal oxide. (Adapted from Ref. [45])

For TFT fabrication, sol-gel techniques appear very appealing due to their advantages such as cost-effectiveness or large-area uniformity when associated to spin-coating. Other techniques such as dip-coating, slit coating, spray pyrolysis and inkjet printing have also been used to coat/deposit precursor solutions for TFT fabrication. As mentioned previously, a high-temperature ($> 500 \text{ }^\circ\text{C}$) thermal annealing is usually required to completely decompose embedded organic compounds in the precursors because organic residue embedded in metal oxide films can strongly affect carrier transport, which degrades the electrical performance of the metal oxide devices. However, high temperature annealing limits the applications of solution processed metal oxide films on flexible substrates such as

plastic substrate, paper, metal foil and textile. Various methods have been reported for fabricating metal oxide films via solution processing techniques at low temperatures (< 300 °C). TFT devices made by these low-temperature solution-processed metal oxide films have exhibit good electrical performance as summarized in Table 1.2.

Table 1.2. Overview of electrical performance of low-temperature solution-processed metal oxide TFT devices.

Channel material	Annealing temperature	Field-effect mobility [cm ² /Vs]	On-off ratio	Subthreshold voltage [V/decade]	Ref.
IZO	250 °C	0.91	$\sim 10^6$	—	25
IZO	275 °C	12	$\sim 10^8$	< 0.5	26
IZO	~ 150 °C	5	$\sim 10^8$	—	35
In ₂ O ₃	250 °C	2.24	$\sim 10^8$	0.45	30
In ₂ O ₃	250 °C	3.37	$\sim 10^7$	—	25
In ₂ O ₃	~ 150 °C	10	$\sim 10^8$	—	35
IGZO	275 °C	9	$\sim 10^8$	< 0.5	26
IGZO	~ 150 °C	9	$\sim 10^8$	—	35
F-doped IZO	250 °C	16.4	$\sim 10^7$	0.32	46

1.4.2. Transparent electrodes

Transparent conductive metal oxide films have been widely used in various kinds of devices such as transistor, solar cells and organic emitting diodes as electrodes. Indium tin oxide (ITO) film is a commercially available transparent conductive oxide (TCO) with a very low resistivity of 1×10^{-4} Ωcm; however, due the expensive price and scarcity of indium, indium-free alternative materials such as impurity doped ZnO (doped with Ga, Al, B), impurity doped SnO₂ (doped with Sb, F, As, Nb, Ta) and other composition have drawn a lot of attention.^[47] For increasing the n-type conductivity of TCO films, the dopant ions should have more valence electrons than the host materials; thus, each dopant can generate one or more free electrons in the host materials. For instance, group III elements such as Ga, B, Al are usually used to dope ZnO. 1-2% of dopant could lead to 2-5 times decrease of resistivity as shown in Table 1.3.^[47]

For the usefulness of TCO films, both optical and electrical properties have to be considered. Their sheet resistivity of TCO films should be $< 10^{-3}$ Ωcm and the average transmittance should be > 80 %.^[47] PLD (pulse laser deposition) or MSP (magnetron sputtering) are commonly used to deposit high quality TCO films. However, PLD and MSP have disadvantage such as low deposition rate and high equipment cost. In recent years, solution processed TCO films have drawn a lot attention due to the low-cost and large-area uniformity. However, it was often discovered that sol-gel processed TCO

films have higher resistivity than those deposited by PLD or MSP. The reason is still unclear because many factors could affect the resistivity such as film thickness, crystalline structure, depositional environment and defects. To improve sol-gel processed TCO films, several methods such as post-annealing in a reducing atmosphere, H₂ plasma treatment and UV irradiation were used to decrease the resistivity of sol-gel deposited TCO films as shown in Table 1.4.

In recent years, several studies have adopted direct-patterning methods as discussed in section 1.2 to pattern TCO films. Ole F. Göbel *et al.* have used micromolding to pattern Al:ZnO (~1% of Al) films.^[52] The smallest line-wide of Al:ZnO patters is ~5 μm as shown in Figure 1.25a. However, very high resistivity ~10 Ωcm was observed from these Al:ZnO films. Hyun Soo Lim *et al.* have applied UV direct-patterning to fabricate ITO lines.^[39] The smallest line-width shown in the article is ~5μm as shown in Figure 1.25b. However the resistivity of photo-patterned ITO films is higher than 10⁻² Ωcm and the resistivity was found to increase with the increase of photosensitizer (benzoylacetone) added into the precursor. The result implies that incomplete decomposition of the organic ligands and insufficient volatilization of benzoylacetone from the ITO thin films could be the main reasons for the high resistivity.

Table 1.3. Summary of resistivity and carrier concentration of ZnO films doped with different impurities. (Adapted from Ref. [24])

Dopant	Dopant content (wt%)	Resistivity × 10 ⁻⁴ (Ω cm)	Carrier concentration × 10 ²⁰ (cm ⁻³)
Al ₂ O ₃	1–2	0.85	15.0
Ga ₂ O ₃	2–7	1.2	14.5
B ₂ O ₃	2	2.0	5.4
Sc ₂ O ₃	2	3.1	6.7
SiO ₂	6	4.8	8.8
V ₂ O ₅	0.5–3	5.0	4.9
F	0.5 (at%)	4.0	5.0
None	0	4.5	2.0

Table 1.4. Summary of additional treatments used for reducing the resistivity of sol-gel fabricated TCO films.

Material	Additional treatment	Decrease of sheet resistance or resistivity	Ref.
AZO	Hydrogen annealing	~1 M → 435 (Ohm/square)	21
AZO	H ₂ plasma treatment	9 → 6 × 10 ⁻¹ (Ωcm)	51
AZO	UV irradiation	6 × 10 ⁻¹ → 7.0 × 10 ⁻² (Ωcm)	51

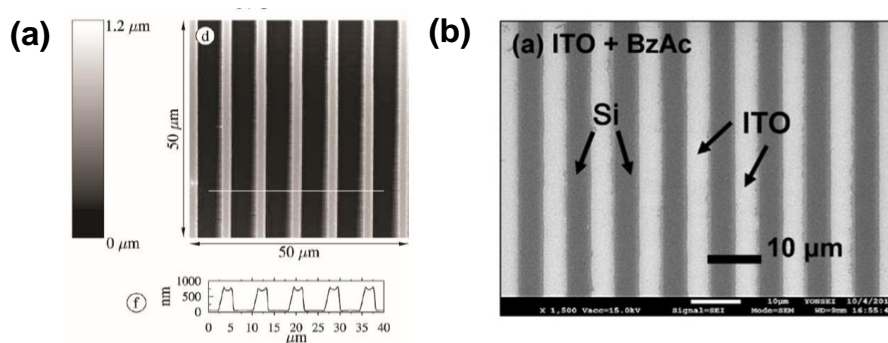


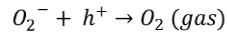
Figure 1.25. (a) AZO lines direct-patterned by micromolding. (b) ITO lines direct-patterned by photosensitive precursor and DUV lithography. (Adapted from Ref. [39] and [52])

1.4.3. Photodetectors

Electrons in the valence band of metal oxide semiconductors can be excited to conduction band (CB) by photo-irradiation, leaving holes in the valence band (VB). Because most of metal oxide semiconductors have wide bandgaps (> 3 eV), only UV light has enough energy to excite electrons to the conduction band. Figure 1.26a shows a typical metal oxide photodetector. During photo-irradiation, electrons in the valence are excited to conduction and transport to electrode under an applied voltage bias. The additional current resulted from photo-excited carriers is called photocurrent. After switching off the light, electrons in the conduction band recombine with holes in the valence band and the photocurrent decreases. ZnO is one of the most widely used metal oxide semiconductors for making photodetectors. The bandgap of ZnO is around ~ 3.3 eV. Figure 1.26b shows a typical real-time response of a sol-gel processed ZnO photodetector.^[53] The current increased $\sim 10^5$ times under UV irradiation due to photo-generated electro-hole pairs as discussed before. After switching off the UV light, current decreased due to electron-hole recombination.

Several reports show clear photoresponse of ZnO thin films to visible light. For instance, Qiang Geng *et al.* showed real-time photoresponse of sol-gel synthesized ZnO thin-film to visible light in N_2 and in air as shown in Figure 1.27a.^[54] Because visible light doesn't have enough energy to excite electrons from conduction band to valence band directly, the photoresponse was explained by two-photon excitation process through a virtual level as shown in the Figure 1.27b.^[54] Cheng-Liang Hsu *et al.* suggested that virtual level is form by deep level traps related to oxygen vacancies.^[55] The energy of blue (465 nm, 2.67 eV) or green light (520 nm, 2.38 eV) is sufficient to excite electrons from conduction band to valence band through these defect levels.

At room temperature, oxygen molecules from atmosphere can be adsorbed at the surface of metal oxide to form O_2^- and decreases the conductivity of metal oxide due to the electron trapping.^[56] Under photo-irradiation, photo-generated holes can react to O_2^- (equation 1.4) and cause oxygen desorption, which increases the conductivity of the metal oxide.



(equation 1.6)

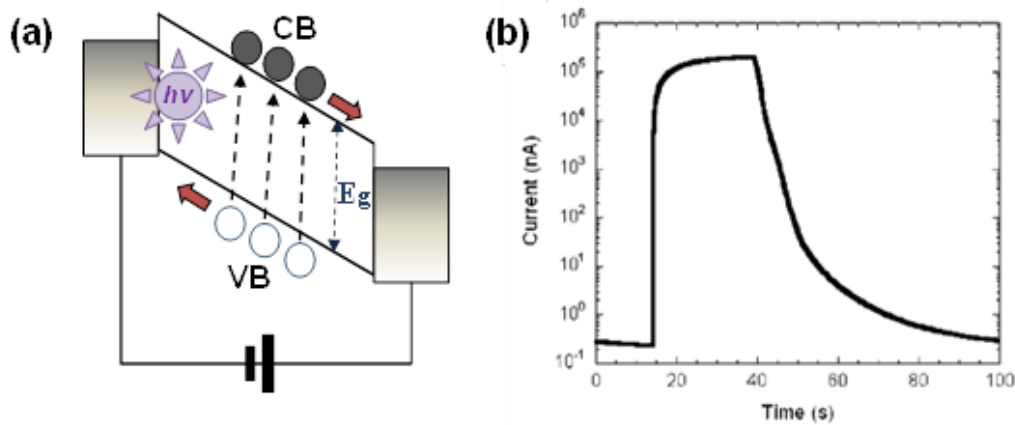


Figure 1.26. (a) Schematic showing excitation of electron-hole pairs in a photodetector. (b) Real-time response of a ZnO photodetector to UV light. (Adapted from Ref. [53])

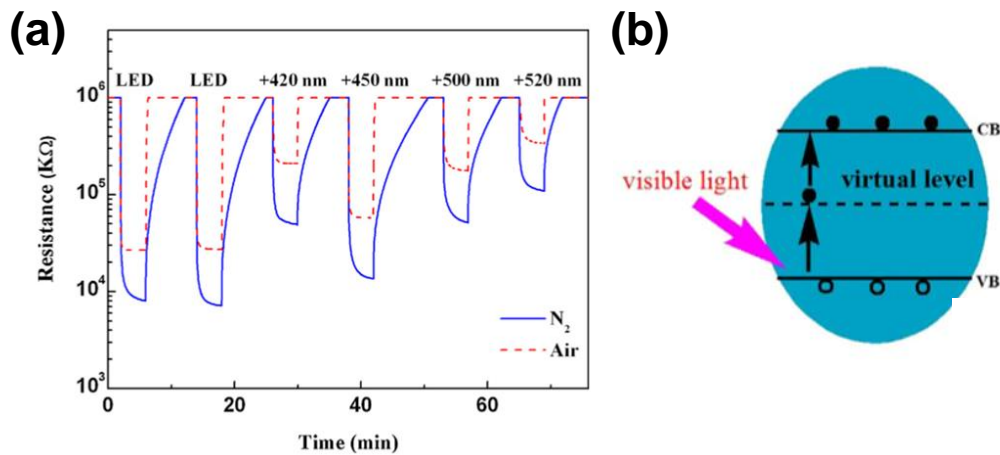


Figure 1.27. (a) The photo response of a ZnO sensor to visible light in N_2 and in air. (b) Schematic showing electrons excited from valence band to conduction band via two-photon excitation. (Adapted from Ref. [54])

1.5. Applications nanostructured metal oxides

In the past few decades, various metal oxide nanostructures such as nanowires, nanoparticles, nanosheets, nanobelts, nanorods have been successfully synthesized via chemical vapor deposition (CVD) and integrated into bottom up devices such as transistors, gas sensors, biochemical sensors, and photodetectors. Because of their large surface-to-volume ratio and nearly defect-free crystalline structures, oxide nanostructures, especially nanowires, have showed remarkable electrical properties as building blocks for electronic devices. However, oxide nanostructures synthesized by CVD suffer from problems such as uniformity and post-growth assembly. On the other hand, photopatterning has the advantage of fabricating high resolution oxide patterns at nanoscale dimensions on precise positions by using photolithography. In the following sections, we will introduce several kinds of nanostructured oxide devices and we believe the potential of using photopatterning to fabricate functional metal oxide nanostructures warrants further investigation.

1.5.1. Gas sensors

Metal oxide semiconductors are widely used as sensing materials to detect various gases and biochemical compounds because of their superior conductivity and stability compared to organic materials. The gas sensing mechanisms can be described by charge trapping/detrapping or oxidation/reduction on the surface of metal oxide semiconductors. The variation of carrier concentration in the metal oxide causes change in its resistivity and current value in sensing devices. As shown in Figure 28a, after an electron is trapped by gas molecule, a depletion region appears on the surface of metal oxide film which has higher resistivity than other region. During gas sensing, a lot gas molecules are absorbed on the surface of the metal oxide thin films or nanostructures, which largely increase their resistivity and decrease the current flow in the sensing device. By monitoring the current change, one can estimate or calculate the concentration of the target gases.

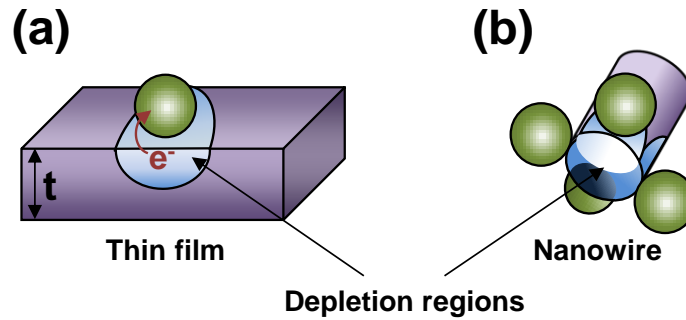


Figure 1.28. Depletion regions caused by absorbed gas molecules on a metal oxide (a) thin film and (b) nanowire.

Metal oxide nanostructures are expected to have higher sensitivity than thick films because of their high surface-to-volume ratio. As shown in Figure 1.28b, high surface-to-volume ratio nanostructures such as nanowires can be fully depleted by chemisorbed gas molecules; therefore, the current flowing in the nanowires is effectively affected by the depletion region. Many studies have been dedicated to fabricate nanowire devices and investigate their gas sensing properties. It has been reported that nanowire devices have very high sensitivity down to several ppm level.^[57] However, the fabrication of nanowire devices is very challenging. It is difficult to align and connect nanowires properly on the substrate. Although several methods have been developed to align nanowires, the assembly is not good enough in uniformity and precision, which makes it difficult to integrate chemically synthesized nanowires into bottom up devices and circuits. Figure 1.29a shows nanowire array aligned by anchoring proposed by Jun Yao *et al.*^[58] We can see that although most of the nanowires are placed precisely on the metal contact pads, some nanowires are outside the contact pads. Figure 1.29b shows nanowires array aligned by using PDMS fluidic channel proposed by Yu Huang *et al.*^[59] The positioning is not good enough. Due to the fact that it is very challenge to make post-growth assembly of nanowires, another type of nanowire device has been proposed for sensing applications. The fabrication process of the sensing device is very simple as shown in Figure 1.29c.^[60] Grown nanowires are directly integrated into the sensing device without assembly or alignment, so the nanowires are vertical. During gas sensing, the current is flowing from one electrode through nanowires and their inter contacts to reach another electrode.

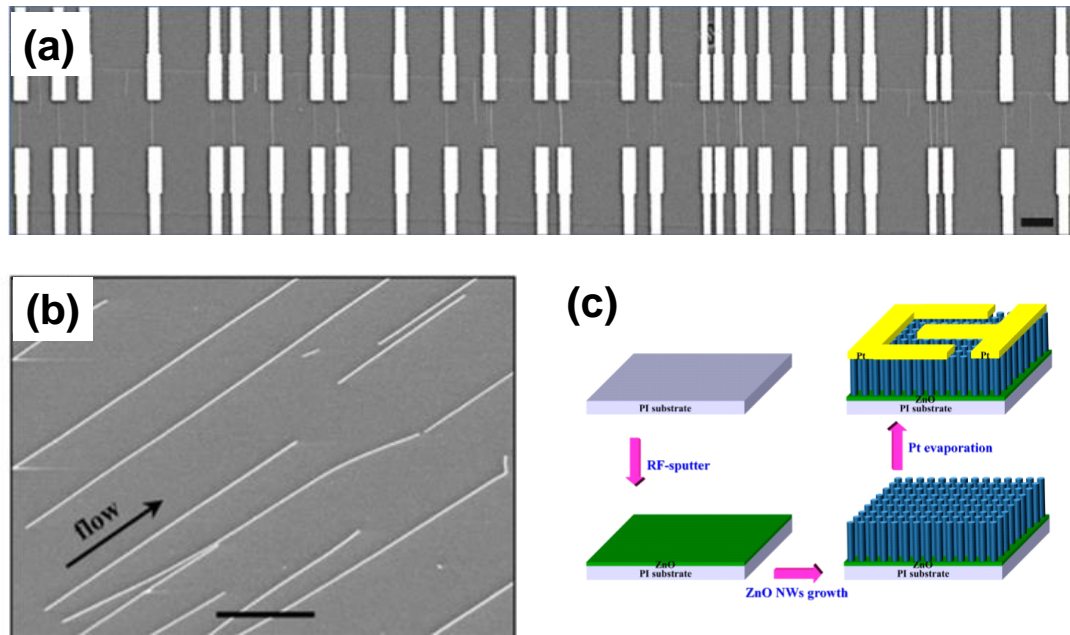


Figure 1.29. (a) Nanowires aligned by anchoring. (b) Nanowires aligned by PDMS fluidic channel. (c) Fabrication process of vertical nanowire device. (Adapted from Ref. [58]-[60])

To show that nanowire devices have better gas sensing performance than thin-film devices, Hyun-Wook Ra *et al.* used nanoscale spacer lithography to fabricate ZnO nanowires of 70 nm width and compared their sensing performance to a 100-nm thick ZnO film.^[61] The SEM image of the well-aligned ZnO nanowires of 70 nm width and 100 nm height fabricated by nanoscale spacer lithography is shown in Figure 1.30a. Under H₂ and CO sensing, the nanowire gas sensor showed a sensitivity that is ~5 times higher than the thin-film counterpart. The better sensing performance was explained by the higher surface-to-volume of the ZnO nanowires. (Figure 1.30b and 1.30c) Gas sensing performances of metal oxide nanowire and thin-film were also compared by E. Brunet *et al.*^[62] The authors used vapor-liquid-solid technique to synthesize SnO₂ nanowires (~200 nm at diameter) and spray pyrolysis to deposit SnO₂ thin-films (~300-nm thick). SnO₂ nanowire device showed a much inferior sensing response than SnO₂ thin-film for sensing 260 ppm of CO gas, which is contradictory to our expectation. Detail comparison is shown in Table 1.5. When exposed to CO, the sensing response (change in resistance) is ~1% (decrease) for nanowire device, which is much lower than the response of thin film ~34%. The authors argue that if we suppose that CO molecules absorbed uniformly on the surface of SnO₂ and sensing response is proportional to the number of chemisorbed CO molecules in the sensing areas for both devices, nanowire device has ~30 times sensing efficiency compared to thin-film device, which is explained as follows. For nanowire device, only 86 CO gas molecules is required to release an trapped electron on the surface of SnO₂ but 2760 gas molecules is required for

the thin-film device. In other words, each CO molecule absorbed on the surface of the nanowire device causes greater change of resistance than each CO molecule on thin-film device. Because surface area of the nanowire device is much smaller than the thin-film, the total number of the absorbed CO molecules and overall change of resistance is smaller than the thin-film device.

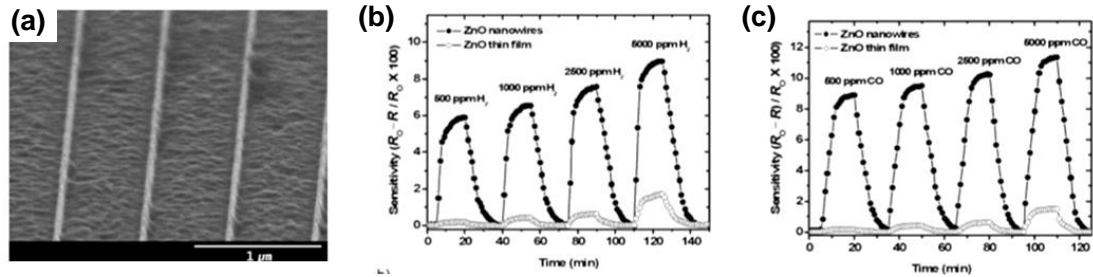


Figure 1.30 (a) SEM image of ZnO well-aligned nanowires fabricated by spacer lithography. (b) The sensing responses of the ZnO nanowires and thin-film to H₂. (c) The sensing responses of the ZnO nanowires and thin-film to CO. (Adapted from Ref. [51])

If the assumptions are correct, one may expect the sensing response can be doubled by doubling the sensing area because the sensing area is proportional to the number of gas molecules absorbed on the surface which is proportional to the sensing response. G.C. Mutinatiaa *et al.* have compared the sensing performance of two SnO₂ thin-film gas sensor with different sensing areas of 100 μm x 100 μm and 100 μm x 5 μm (area ratio = 20 : 1) as shown in Figure 1.31a.^[63] Their sensing responses to H₂ are shown in Figure 1.31b. However, the device of 100 μm x 100 μm area only showed a sensing response that is ~1.2 times higher than the device of 100 μm x 5 μm area, indicating that sensing performance cannot be effectively evaluated by sensing area. Therefore, for E. Brunet's study, instead of concluding that the SnO₂ nanowire sensor has sensing efficiency that is 30 times higher than the thin-film counterpart, other factors and mechanisms have to be investigated for explaining the observation.

Table 1.5. Comparison of the sensing performances of SnO₂ nanowire and thin-film sensors to 260 ppm CO gas. (Adapted from Ref. [61])

Notation	Definition	Thin film	Nanowire	Ratio
A	Exposed surface area (m ²)	2×10^{-8}	2.5×10^{-11}	~800
N_{CO}	Number of CO molecules impinging the sensor surface per second	1.2×10^{16}	1.5×10^{13}	~800
n	Number of electrons flowing in 2 μA/s	1.3×10^{13}	1.3×10^{13}	1
S_{CO}	Sensor response in the presence of CO	33.8%	1.4%	~25
n_e	Number of electrons detected per second	4.2×10^{12}	1.7×10^{11}	~25
N_{CO}/n_e	Number of CO molecules impinging the sensor surface required to detect one electron per second	2760	85	~30

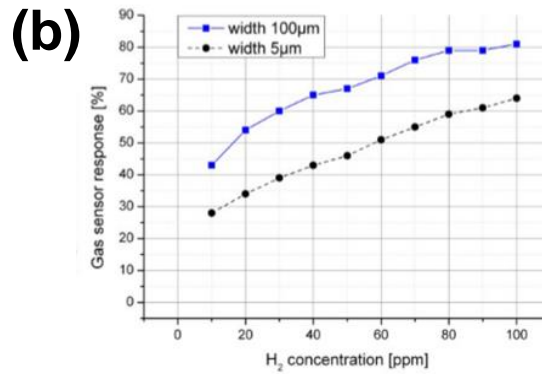
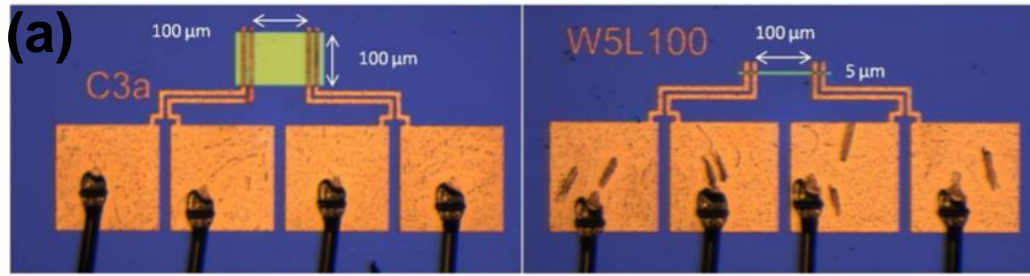


Figure 1.31. (a) OM image of SnO₂ thin-film sensors of different sensing areas. (b) The gas sensing response of SnO₂ sensors of sensing area (100 μm x 100 μm and 100 μm x 5 μm) (Adapted from Ref. [62])

The chemical sensitivity of metal oxide nanowires can be enhanced by doping various kinds of impurities. For instance, Shouou-Jinn Chang *et al.* enhanced the sensitivity of ZnO nanowire to acetone by doping Au nanoparticles.^[56] Cheng-Liang Hsu *et al.* enhanced the sensitivity of ZnO nanowire to ethanol by doping Ti ions.^[64] The enhancement of sensing property was explained by the dopant-induced defects such as oxygen vacancies and trapping sites on the surface nanowires which have strong interactions to the target gases.

1.5.2. Nanowire transistors

Nanowire transistors have emerged as a promising candidate for the next generation very-large-scale integration (VLSI) technology. Nanowires have three dimensional cross-sectional profiles which are able to make omega-shaped gate or gate-all-around structures as shown in Figure 1.32. Furthermore, nanowire transistors with omega-shaped gate or gate-all-around structures have been known to have lower leakage current than conventional single or double-gate transistor due to better gate controllability over the channel region. The gate controllability is very important as the size of transistor becomes smaller. Low level of gate control may cause short channel effects which increases leakage current and power consumption. In recent years, various kinds of nanowire transistors have been fabricated by different lithography methods. Both n-type and p-type nanowire transistors are available. For n-type transistor, the channel material can be Si, Ge, SiGe, or III-V

material such as InAs. For p-type transistor, the channel can be Si, Ge, or SiGe.

Metal oxide nanowires can also be used as channel materials in nanowire transistors because of their good electrical properties and three-dimensional profiles. Chemically synthesized ZnO nanowires are single crystal and nearly defect-free. It has been report that with proper passivation, the field-effect mobility of ZnO nanowires can exceed $1000 \text{ cm}^2/\text{Vs}$.^[65] To shown the potential of using metal oxide nanowires for making nanowire transistors. Kihyun Keem *et al.* have demonstrated an omega-shaped gate ZnO nanowire transistor and compared the device performance with a single back-gate ZnO nanowire transistor.^[66] The results showed that omega-shaped gate geometry and the passivation due to the coverage of gate dielectric (Al_2O_3) effectively enhanced the device performance. The field-effect mobility increased from 8.6 to $30.2 \text{ cm}^2/\text{Vs}$ and, due to a better gate controllability, the on-off ratio increased from 1.09 to 10^7 .

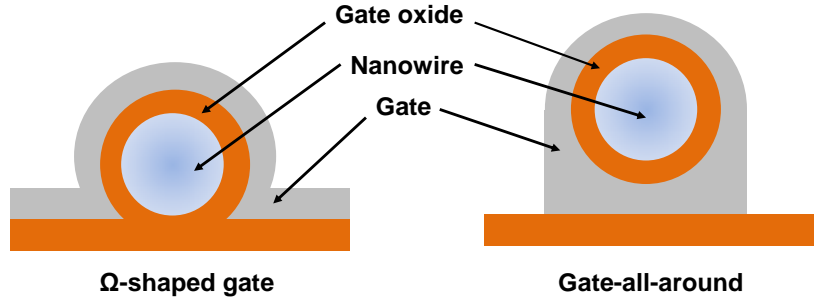


Figure 1.32. Cross-sectional profiles of Ω -shaped gate and gate-all-around structures of nanowire transistor.

1.6. Transition metal doped metal oxide semiconductors for spin-based applications

After the discovery of giant magnetoresistance (GMR) effect, many spin-based devices such as spin LEDs, spin transistors and memories have been invented. Spin-based data storage is expected to have lower power consumption, higher data processing speed and better stability. A standard GMR device is shown in Figure 1.35a. By manipulating the magnetization of ferromagnetic contacts, the resistance of the GMR device can be changed. The overall resistance of the GMR device is lower when the two contacts are in parallel magnetization and is higher when the two contracts are in antiparallel magnetization. The difference of resistances between these two states is ΔR , ($R_{\text{antiparall}} - R_{\text{parallel}}$), which can be expressed by the following equation.^[69]

$$\frac{\Delta R}{R_{\text{parallel}}} = \frac{\beta^2 R_{FM}^2}{1 - \beta^2 R_{SC}^2} \frac{4}{(2 \left(\frac{R_{FM}}{R_{SC}}\right) + 1)^2 - \beta^2} \quad (\text{equation 1.7})$$

β is spin polarization defined as $(n_{\uparrow} - n_{\downarrow})/(n_{\uparrow} + n_{\downarrow})$ in the contacts. R_{FM} and R_{SC} are the resistances of ferromagnetic (FM) contacts and non-magnetic (NM) semiconducting interlayer respectively.

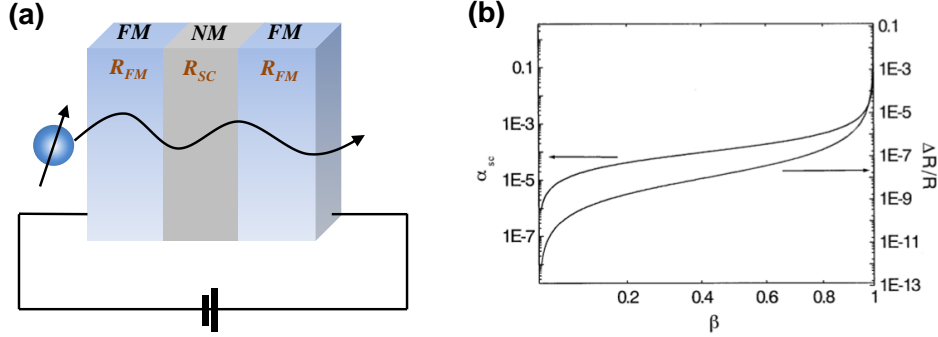


Figure 1.35. (a) Schematic showing a GMR device. (b) Spin polarization of current $\alpha_{sc}[(j_{\uparrow} - j_{\downarrow})/(j_{\uparrow} + j_{\downarrow})]$ and resistance change ($\Delta R/R_{parallel}$) plotted versus β for a GMR device. Detailed assumptions are described in Ref. [43]. (Adapted from Ref. [69])

In previous studies, GMR device used ferromagnetic metals (Fe, Co Ni) as contacts. However, the GMR effect is too small to be convincing. According to equation 1.7, we can see that $\Delta R/R_{parallel}$ is highly dependent on the factor $(R_{FM}/R_{SC})^2$. Because the resistance of metal contact (R_{FM}) is much smaller than the resistance of semiconductor layer (R_{SC}), the factor $(R_{FM}/R_{SC})^2$ is very small and the change of resistance due to GMR effect is difficult to be observed. One possible solution to this problem is to use diluted magnetic semiconductors (DMS) as contact materials. Because the resistivity of DMSs are close to the NM semiconducting interlayer, the factor $(R_{FM}/R_{SC})^2$ is big enough for the GMR effect. The spin polarization in DMS materials is also important. The relation of $\Delta R/R_{parallel}$ versus spin polarization β is shown in Figure 1.35b. GMR effect is increased with the increase of spin polarization in the contacts. The α_{sc} shown in Figure 1.35b represent the spin polarized current, $(j_{\uparrow} - j_{\downarrow})/(j_{\uparrow} + j_{\downarrow})$, in the GMR device.

In 1980s, a variety of DMS materials have been developed based on Mn-doped II-VI semiconductors; however, these DMS materials can only operate at very low temperatures, which hinders their applications in spintronic devices. In recent years, wide-bandgap transition metals (TM) doped wide-bandgap metal oxide semiconductors have drawn a lot of attention because of their room-temperature ferromagnetism (RTFM).^[70] The origin of RTFM is still unclear. Many theories and models have been proposed to explain the origin of RTFM. Shallow donor model proposed by Coey *et al.* is the most widely used theory to explain the RTFM observed in TM-doped metal oxide

semiconductors.^[23] Coey suggested that the exchange coupling between oxygen vacancies and TM cations forms bound magnetic polarons (BMPs) as illustrated in Figure 1.36a and the hybridization of dopant's 3d states with defect states at Fermi level lead to RTFM. Coey introduced a factor $(r_c^{\text{eff}}/r_o)^3$ to the exchange parameter (J_{sd}) for the hybridization of orbitals, where r_c^{eff} the effective cation radius and r_o is the radius of oxygen.

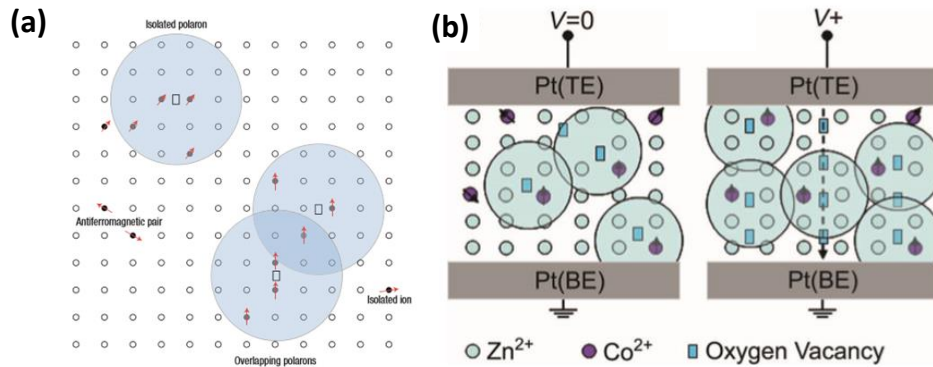


Figure 1.36. (a) Schematic showing bound magnetic polarons and their interaction. (b) Schematic showing the oxygen vacancies in a Co:ZnO RRAM are aligned vertically under positive bias, which enhances the ferromagnetism of the device. (Adapted from Ref. [23], [71])

Although many reports have demonstrated TM-doped MO films or structures showing RTFM via vapor-phase deposition or solution processing, until now, only a few reports demonstrated successful applications in spintronic devices, which may be due the following reasons. Since RTFM is strongly dependent on the formation of defects, the magnetic properties are sensitive to preparation methods and experimental environments. In addition, it is difficult to control the uniformity of TM dopants in the host materials. TM dopants can easily aggregate and form very small clusters during deposition. It noteworthy that in 2012, Cuang Chen *et al.* have demonstrated one successfully application of TM-doped metal oxide DMS.^[46,71] The team integrated Co-doped ZnO films into resistive random access memory (RRAM) structure as storage medium. Besides showing good resistive switching between high resistive state and low resistive state, the device has exhibited memory effects in magnetic properties. The magnetization and coercive field can be modulated by the applied voltage bias. In the article, the magnetic memory effect was explained by the migration of oxygen vacancies which affects the interactions between BMPs as shown in Figure 1.36b, which provide an additional dimension for the resistive random access memory.

1.7. Bibliography

- [1] A. Facchetti, T. J. Marks, *Transparent Electronics* (Wiley, 2010).
- [2] Y. Yang, Y. Q. Li, S. Y. Fu, H. M. Xiao, *J. Phys. Chem. C*, 2008, 112, 10553.
- [3] D. Zhang, W. Yu, D. Hao, L. Li, H. Liu and Z. Lu, *J. Mater. Chem.*, 2012, 22, 17328.
- [4] Y. Huang, L. Liu, M. Johnson, A. C. Hillier, M. Lu, *Nanotechnology*, 2016, 27, 095302.
- [5] K. Mondal, A. Sharma, *RSC Adv.*, 2016, 6, 83589.
- [6] G. F. Boesen, J. E. Jacobs, *Proceedings of the Institute of Electrical and Electronics Engineers* 1968, 56, 2094.
- [7] A. Aoki, H. Sasakura, *J. J. Appl. Phys.*, 1970, 9, 582.
- [8] K. Nomura, H. Ohta, K. Ueda, T. Kamiya, M. Hirano, H. Hosono, *Science*, 2003, 300, 1269.
- [9] K. Nomura, H. Ohta, A. Takagi, T. Kamiya, M. Hirano, H. Hosono, *Nature* 2004, 432, 488.
- [10] T. Matsuo, S. Mori, A. Ban, A. Imaya, *SID Symp. Dig. Tech. Pap.*, 2014, 45, 83.
- [11] D.B. Buchholz, Q. Ma, D. Alducin, A. Ponce, M. José-Yacamán, R. Khanal, J. E. Medvedeva, R.P.H. Chang. 2014, 26, 5401.
- [12] A. B. Djurišić, X. Chen, Y. H. Leung, A. M. C. Ng, *J. Mater. Chem.*, 2012, 22, 6526.
- [13] X. Yu, T. J. Marks, A. Facchetti, *Nat. Mater.*, 2016, 15, 383.
- [14] S. Bai, W. Wu, Y. Qin, N. Cui, D. J. Bayerl, Wang, X. *Adv. Funct. Mater.*, 2011, 21, 4464.
- [15] L. Filipovic, S. Selberherr, *Sensors*, 2015, 15, 7206.
- [16] A. Choi, K. Kim, H. I. Jung, S. Y. Lee, *Sens. Actuators B Chem.*, 2010 148, 577.
- [17] M.-S. Kim, Y. H. Hwang, S. Kim, Z. Guo, D.-I Moon, J.-M. Choi, M.-L. Seol, B.-S. Bae, Y.-K. Choi. *Appl. Phys. Lett.*, 2012, 101, 243503.
- [18] E. Fortunato, P. Barquinha, R. Martins, *Adv. Mater.*, 2012, 24, 2945.
- [19] H. S. Kim, S. H. Jeon, J. S. Park, T. S. Kim, K. S. Son, J. B. Seon, S. J. Seo, S. J. Kim, E. Lee, J. G. Chung, H. Lee, S. Han, M. Ryu, S. Y. Lee, and K. Kim, *Sci. Rep.*, 2013, 3, 1459.
- [20] Y. Shigesato, D. C. Paine, *Thin Solid Films*, 1994, 238, 44.
- [21] H. Damm, P. Adriaenssens, C. De Dobbelaere, B. Capon, K. Elen, J. Drijkoningen, B. Conings, J. V. Manca, J. D'Haen, C. Detavernier, P. C. M. M. Magusin, J. Hadermann, A. Hardy, M. K. V. Bael, *Chem. Mater.* 2014, 26, 5839.
- [22] J. Owen, M. S. Son, K. H. Yoo, B. D. Ahn, S. Y. Lee, *Appl. Phys. Lett.*, 2007, 90, 033512.
- [23] J. M. D. Coey, M. Venkatesan, C. B. Fitzgerald, *Nat. Mater.*, 2005, 4, 173.
- [24] C. Glynn, C. O'Dwyer, *Adv. Mater. Interf.*, 2016, 4, 1600610.
- [25] M. G. Kim, M. G. Kanatzidis, A. Facchetti, T. J. Marks, *Nat. Mater.*, 2011, 10, 382.
- [26] K. K. Banger, Y. Yamashita, K. Mori, R. L. Peterson, T. Leedham, J. Rickard, H. Sirringhaus, *Nat. Mater.*, 2011, 10, 45.
- [27] C. R. Martin and I. A. Aksay, *J. Phys. Chem. B*, 2003, 107, 4261.
- [28] S. Sung, S. Park, S. Cha, W. J. Lee, C. H. Kim, M. H. Yoon, *RSC Adv.*, 2015, 5, 38125.
- [29] Y. Li, L. Lan, S. Sun, Z. Lin, P. Gao, W. Song, E. Song, P. Zhang, J. Peng, *ACS Appl. Mater.*

Interfaces, 2017, 9, 8194.

- [30] Y. S. Rim, H. S. Lim, H. J. Kim, ACS appl. Mater. Interfaces, 2013, 5, 3565.
- [31] B. Radha, S. Kiruthika, G. U. Kulkarni, J. Am. Chem. Soc., 2011, 133, 12706.
- [32] M. S. Saifullah, K. R. Subramanian, D. J. Kang, D. Anderson, W. T. Huck, G. A. Jones, M. E. Welland, Adv. Mater. 2005, 17, 1757.
- [33] E. J. ASutanto, K. Shigeta, Y. K. Kim, P. G. Graf, D. J. Hoelzle, K. L. Barton, A. G. Alleyne, P. M. Ferreira, . Rogers, J. Micromech. Microeng., 2012, 22, 045008.
- [34] S.-Y. Kim, K. Kim, Y. H. Hwang, J. Park, J. Jang, Y. Nam, Y. Kang, M. Kim, H. J. Park, Z. Lee, J. Choi, Y. Kim, S. Jeong, B.-S. Bae, J.-U. Park, Nanoscale, 2016, 8, 17113.
- [35] Y. H. Kim, J. S. Heo, T. H. Kim, S. Park, M. H. Yoon, J. Kim, M. S. Oh, G. R. Yi, Y. Y. Noh, S. K. Park, Nature 2012, 489, 128.
- [36] S. Park, K.-H. Kim, J.-W. Jo, S. Sung, K.-T. Kim, W.-J. Lee, J. Kim, H. J. Kim, G.-R. Yi, Y.-H. Kim, M.-H. Yoon, S. K. Park, Adv. Funct. Mater. 2015, 25, 2807.
- [37] F. Stehlin, F. Wieder, A. Spangenberg, J. M. Le Meins, O. Soppera, J. Mater. Chem. C 2014, 2, 277.
- [38] P. C. With, U. Helmstedt, S. Naumov, A. Sobottka, A. Prager, U. Decker, R. Heller, B. Abel, L. Prager, Chem. Mater., 2016, 28, 7715.
- [39] H. S. Lim, Y. S. Rim and H. J. Kim, Sci Rep., 2014, 4, 4544.
- [40] Y. S. Rim, H. Chen, Y. Liu, S. H. Bae, H. J. Kim, Y. Yang, ACS Nano, 2014, 8, 9680.
- [41] Y. J. Jeong, T. K. An, D.-J. Yun, L. H. Kim, S. Park, Y. Kim, S. Nam, K. H. Lee, S. Hyun Kim, J. Jang, C. E. Park, ACS appl. Mater. Interfaces, 2016, 8, 5499.
- [42] H.-C. Lin, F. Stehlin, O. Soppera, H.-W. Zan, C.-H. Li, F. Wieder, A. Ponche, D. Berling, B.-H. Yeh and K.-H. Wang, Sci Rep., 2015, 5, 10490.
- [43] M. Yu, H. Xu, V. Kosma, J. Odent, K. Kasahara, E. Giannelis, C. Ober, J. Photopolym. Sci. Tec., 2016, 29, 509.
- [44] C. Chevalier-César, K. Nomenyo, A. Romyantseva, A. Gokarna, A. Gwiazda, G. Léron del, Adv. Funct. Mater. 2016, 26, 1787.
- [45] S. R. Thomas, P. Pattanasattayavong, T. D. Anthopoulos, Chem. Soc. Rev., 2013, 42, 6910.
- [46] J. S. Seo , J. H. Jeon, Y. H. Hwang, H. Park, M. Ryu, S. H. K. Park, B. S. Bae, Sci. Rep., 2013, 3, 2085.
- [47] T. Minami, Semicond. Sci. Technol.. 2005, 20, S35.
- [48] F. Stehlin, Y. Bourgin, A. Spangenberg, Y. Jourlin, O. Parriaux, S. Reynaud, F. Wieder and O. Soppera, Opt. Lett., 2012, 37, 4651.
- [49] V. Auzelyte, H. Sigg, B. Schmitt, H. H. Solak, Nanotechnology 2010, 21, 215302.

- [50] P. G. Reddy, N. Mamidi, P. Kumar, S. K. Sharma, S. Ghosh, K. E. Gonsalves and C. P. Pradeep, *RSC Adv.*, 2016, 6, 67143.
- [51] S. Vunnam, K. Ankireddy, J. Kellar, W. Cross, *Nanotechnology*, 2014, 25, 195301.
- [52] O. F. Göbel, D. H. Blank, J. E. ten Elshof, *ACS Appl. Mater. Interfaces*, 2010, 2, 536.
- [53] Y. Jin, J. Wang, B. Sun, J. C. Blakesley, N. C. Greenham, *Nano Lett.*, 2008, 8, 1649.
- [54] Q. Geng, Z. He, X. Chen, W. Dai, X. Wang, *Sens. Actuators B*, 2013, 188, 293-297.
- [55] C. L. Hsu, Y. H. Lin, L. K. Wang, T. J. Hsueh, S. P. Chang, S. J. Chang, *ACS Appl. Mater. Interfaces*, 2017, 9, 14935.
- [56] S.-J. Chang, T.-J. Hsueh, I.-C. Chen, S.-F. Hsieh, S.-P. Chang, C.-L. Hsu, Y.-R. Lin, B.-R. Huang, *IEEE Trans. Nanotechnol.*, 2008, 7, 754.
- [57] A. Kolmakov, Y. Zhang, G. Cheng, M. Moskovits, *Adv. Mater.*, 2003, 15, 997.
- [58] J. Yao, H. Yan, C. M. Lieber, *Nat. Nanotechnol.*, 2013, 8, 329.
- [59] Y. Huang, X. Duan, Q. Wei, C. M. Lieber, *Science*, 2001, 291, 630.
- [60] C. L. Hsu, H. H. Li, T. J. Hsueh, *ACS Appl. Mater. Interfaces*, 2013, 5, 11142.
- [61] H. W. Ra, K. S. Choi, J. H. Kim, Y. B. Hahn, Y. H. Im, *Small*, 2008, 4, 1105.
- [62] E. Brunet, T. Maiera, G.C. Mutinatia, S. Steinhauera, A. Köcka, C. Gspanb, W. Groggerb, *Sens. Actuators B*, 2012, 165, 110.
- [63] G.C. Mutinatiaa, E. Bruneta, S. Steinhauera, A. Köcka, J. Tevab, J. Kraftb, J. Siegertb, F. Schrankb, E. Bertagnollic, *Proc. Eng.*, 2012, 47, 490.
- [64] C. L. Hsu, Y. D. Gao, Y. S. Chen, T. J. Hsueh, *Sens. Actuators B*, 2014, 192, 550.
- [65] P.-C. Chang, Z. Fan, C.-J. Chien, *Appl. Phys. Lett.*, 2006, 89, 133113.
- [66] K. Keem, D.-Y. Jeong, S. Kim, *Nano Lett.*, 2006, 6, 1454.
- [67] L. Znaidi, (2010). *Mater. Sci. Eng. B*, 2010, 174, 18.
- [68] A. G. Vega-Poot, G. Rodriguez-Gattorno, O. E. Soberanis-Dominguez, R. T. Patiño-Díaz, M. Espinosa-Pesqueira, G. Oskam, *Nanoscale*, 2010, 2, 2710.
- [69] G. Schmidt, L. W. Molenkamp, *Physica E*, 2001, 10, 484.
- [70] I. Djerdj, Z. Jagličić, D. Arčon, M. Niederberger, *Nanoscale*, 2010, 2, 1096.
- [71] G. Chen, C. Song, C. Chen, S. Gao, F. Zeng, F. Pan, *Adv. Mater.* 2012, 24, 3515.

Chapter II: Experimental Methods

Résumé du Chapitre II	56
2.1. Solution preparation.....	57
2.2. Thin film deposition.....	58
2.3. DUV-patterning.....	58
2.4. Development procedure.....	59
2.5. Thin film characterization	61
2.5.1. X-ray photoelectron spectrometry (XPS)	61
2.5.2. Fourier Transform Infrared (FTIR)	62
2.5.3. Raman spectroscopy	63
2.5.4. X-ray diffraction (XRD)	64
2.5.5. Temperature- Programmed Desorption (TPD).....	65
2.5.6. Optical measurements	65
2.6. Thin-film transistor fabrication and electrical measurements....	66
2.7. Gas sensing and micro-fluid gas sensing system.....	66
2.8. Magnetic measurements.....	67
2.9. Bibliography	68

Résumé du Chapitre II

Le chapitre II décrit les principales techniques expérimentales utilisées dans ce travail pour la mise en forme et la caractérisation des micro-nano-structures ZnO.

En premier lieu, les méthodes de préparation des solutions sont décrites. La préparation de la solution de référence à base de ZnMAA est tout d'abord explicitée. Puis, les protocoles de préparation des solutions dopées en ions Al^{3+} et Co^{2+} , respectivement pour des propriétés électriques et magnétiques sont donnés.

Les films minces sont préparés par la méthode de spin-coating. Ces films sont ensuite caractérisés par différentes techniques adaptées aux films minces : la spectroscopie de photo-électrons X (XPS) permet d'obtenir une analyse élémentaire à différents stades de la préparation. Les spectroscopies FTIR et Raman permettent de compléter cette étude, notamment en suivant la présence du complexant et également en détectant des éventuelles phases cristallines dans le matériau. L'étude du caractère cristallin est complétée par la diffraction des rayons X (DRX). Enfin, l'étude de propriétés optiques (indice de réfraction, absorption) menée par ellipsométrie spectroscopique et absorption UV-visible fournit des informations complémentaires sur la nature du matériau. Ces techniques d'analyse sont utilisées pour caractériser les matériaux après chacune des étapes de préparation et en faisant varier les conditions expérimentales.

Deux dispositifs de micro-nano-structuration ont été utilisés : une technique classique de projection de masque et une technique de nanofabrication par lithographie interférométrie. Les dimensions latérales caractéristiques des structures sont alors respectivement de 800 nm et 300 nm. Ces structures peuvent être aisément mesurées par Microscopie à Force Atomique (AFM).

Enfin, les propriétés électriques et magnétiques des matériaux ont été caractérisées. Une description des configurations utilisées est donnée dans la fin de ce Chapitre.

2.1. Solution preparation

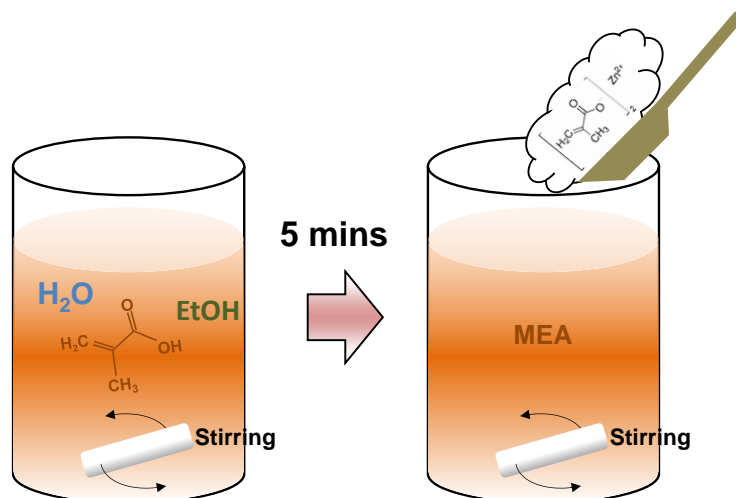


Figure 2.1. Schematic showing the process of solution preparation.

Figure 2.1. shows the procedure of solution preparation as follows. 4 ml ethanol, 4 ml methacrylic acid (99% Aldrich) and 1.8ml acid water (0.37 M) were mixed together and stirred for 5 minutes. Then, 1.06 g of zinc methacrylate ($\text{Zn}(\text{CH}_2\text{CH}_3\text{COO})_2$, Aldrich) and 0.27 ml of ethanolamine (MEA, Aldrich, 99.5%) were added into the mixture in sequence. The molar ratio between zinc methacrylate and MEA was fixed at 1:1. Finally, the ZnMAA precursor was stirred vigorously for 24 hours before use. In this work, different concentrations of ZnMAA precursors were prepared by adjusting the amount of zinc methacrylate powder added into the solutions.

For Co-doped ZnMAA precursor, 4 ml ethanol, 4 ml methacrylic acid and 1.8 ml HCl (0.37 M) were mixed together and stirred for 5 minutes. Then, 0.168 g of cobalt acetate powder (Aldrich, 99.995%) and 1.06 g of zinc methacrylate powder were added into the mixture which formed a homogeneous precursor without precipitation. The molar ratio of $[\text{Co}/\text{Co}+\text{Zn}]$ is 0.15. Finally, the Co-doped ZnMAA precursor was stirred vigorously for 24 hours before use.

For Al-doped ZnMAA precursor, 4 ml ethanol, 3 ml methacrylic acid, 1 ml acetylacetone (Aldrich, 99%) and 1.8 ml HCl (0.37 M) were mixed together and stirred for 5 minutes. Then, we added 0.043 g of aluminum acetylacetonate powder (Aldrich, 99%) and 1.06 g of zinc methacrylate powder into the mixture which formed a homogeneous precursor without precipitation. The molar ratio of $[\text{Al}/\text{Al}+\text{Zn}]$ is 0.02. Finally, the Al-doped ZnMAA precursor was stirred vigorously for 24 hours before use.

2.2. Thin film deposition

As shown in Figure 2.2, the precursor solution was filed into a syringe with a Teflon filter with pores of 0.2 μm . The solution was then deposited onto a piece of silicon wafer fixed on the spin-coater. The thin film was formed by spin-coating, with typical rotation speed between 2000 rpm and 6000 rpm (60 sec. rotation), giving rise to films with thickness typically between 150 and 80 nm. To remove excess solvent, the sample is put on hot plate at 50 $^{\circ}\text{C}$ for 5 mins.

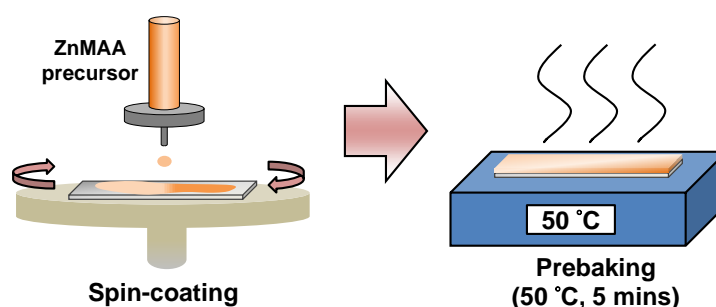


Figure 2.2. Schematic showing the formation of uniform gel-film by using spin-coating and prebaking.

2.3. DUV-patterning

After photosensitive zinc precursor was spin-coated on a Si substrate, DUV irradiation was conducted using Braggstar ArF laser (Coherent) emitting at 193 nm. Two optical setups were used in this work. One is DUV lithography with a photomask as shown in Figure 2.3a, another is DUV interference system as shown in Figure 2.3b. The period of photomask is $\sim 1.63 \mu\text{m}$ with a line-width of $\sim 833 \text{ nm}$. We used spacers (125 microns thickness) to separate the gel film and the photomask to avoid possible contamination.

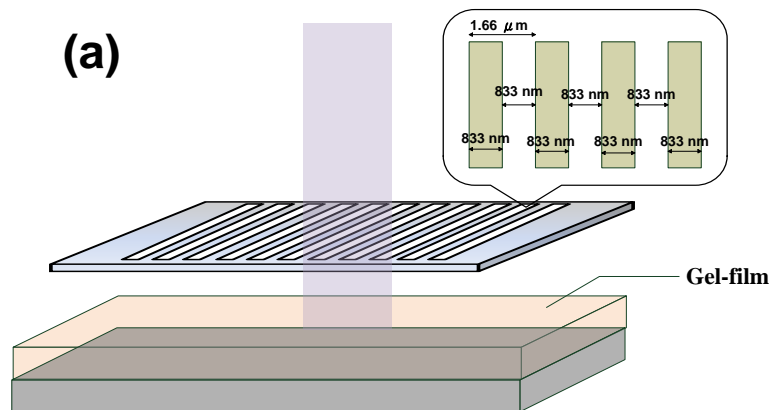
Smaller pattern-size can be achieved by using DUV interference system. As shown in the Figure 2.3b, after the DUV light beam passed through the first diffraction grating, the raw light beam from the laser source was split into three light beams by the first diffraction grating, order +1, order -1 and order 0. The order 0 was blocked by a piece of metal. After passing through the second grating, the +1 order of first light beam converged with the -1 order of the second light beam, which generated interference patterns. The periods of the first and second grating used in this work are 400 nm and 300 nm respectively, the interference patterns are of 600 nm period. Ideally, $\sim 300 \text{ nm}$ line-width can be obtained by using this system. The laser power was kept at 3.6 mw and the irradiation time was

controlled by the software (Labview) in the computer. The raw beam size emitted from the laser is approximately a rectangular of 1 cm X 0.5 cm. For improving the quality interference patterns, we used a circle pin hole of 2 mm diameter to block inhomogeneous regions of the laser beam.

2.4. Development procedure

After DUV irradiation, we developed the sample in polar solvents (developer) such as 1-propanol, ethanol and cyclohexanone to remove unexposed regions as shown in Figure 2.4 and the DUV crosslinked regions can be revealed on the substrate. Figure 2.5 shows the AFM images of TiO_2 , ZrO_2 and HfO_2 nanostructures irradiated by DUV interference light and developed in cyclohexanone for 30s. Fine patterns of 300 nm periodic lines can be obtained.^[1]

Photopatterned films are characterized by Atomic Force Microscopy in resonant mode. The AFM equipment used here is a Picoscan system from Molecular Imaging. In this case, Si_3N_4 tips with a typical resonance frequency of 285 kHz (stiffness 42 N/m) were used.



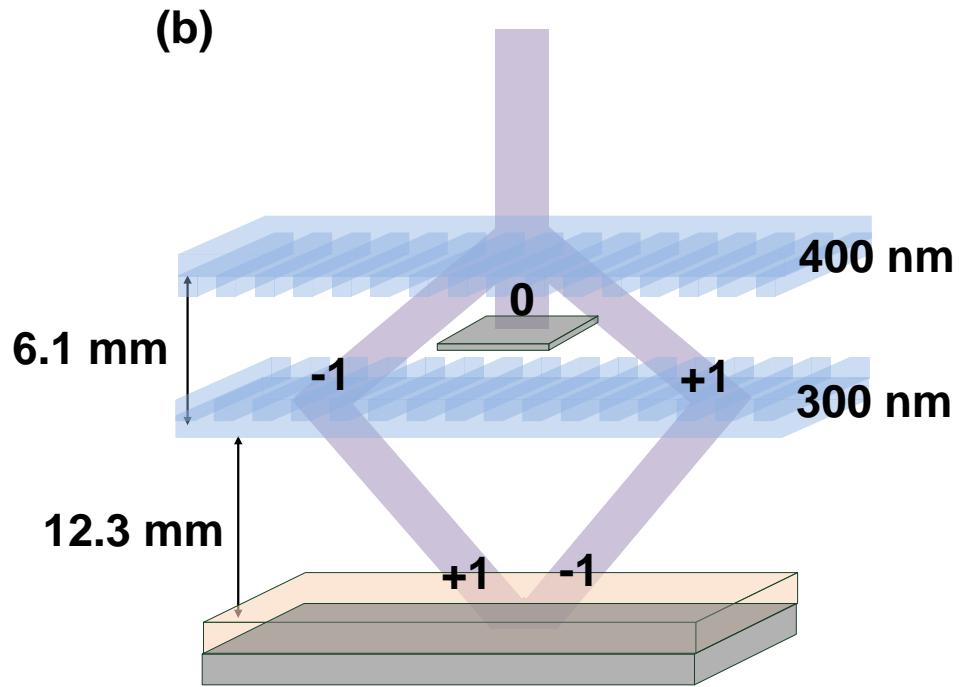


Figure 2.3. (a) Schematic showing the DUV-patterning through a binary photomask. (b) Schematic showing DUV-interference patterning.

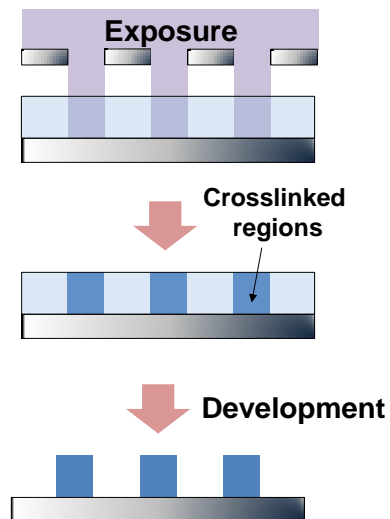


Figure 2.4. Schematic showing the development procedure which removed the non-irradiated regions of the precursor film.

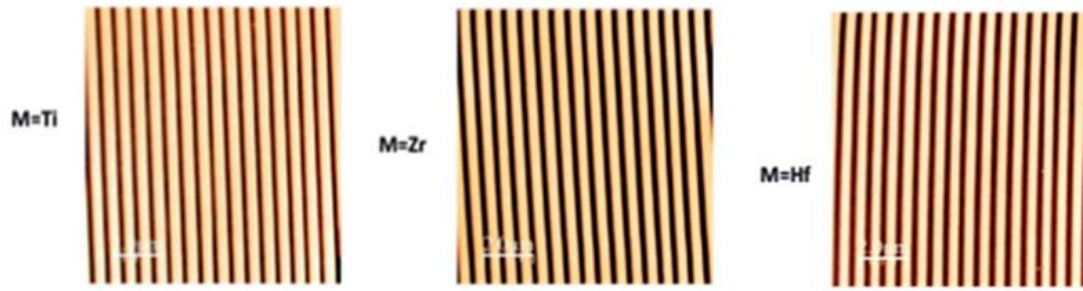


Figure 2.5. AFM images of periodic TiO_2 , ZrO_2 and HfO_2 lines patterned by the DUV interference system. (Adapted from reference [1])

2.5. Thin film characterization

2.5.1. X-ray photoelectron spectrometry (XPS)

XPS is a very interesting technique for investigating metal oxide thin films since it gives access to a quantitative atomic composition analysis of the material. XPS is a surface analysis technique (the depth of penetration is around 10 nm) but since thin films are used here, we assumed that the composition did not vary along the film thickness. XPS analysis was performed on a Gammatdata Scienta (Uppsala, Sweden) SES 200-2 X-ray photoelectron spectrometer under ultra-high vacuum ($P < 10^{-9}$ mbar). The monochromatized AlK α source (1486.6 eV) was operated at a power of 420W (30 mA and 14 kV) and the spectra were acquired at a take-off angle (TOA) of 90° (angle between the sample surface and photoemission direction). During acquisition, the pass energy was set to 500 eV for wide scans and to 100 eV for high-resolution spectra. CASAXPS software (Casa Software Ltd, Teignmouth, UK, www.casaxps.com) was used for all peak fitting procedures and areas of each component were corrected according to classical Scofield sensitivity factors (Si 2p: 0.817, C 1s: 1.00 and O 1s: 2.93) and transmission function of the spectrometer. All components on high-resolution spectra were referenced according to the CH_x component at 285.0eV.

Figure 2.6 shows a typical XPS spectrum of ZnO derived from ZnMAA precursor. The O 1s spectrum located at 531 eV provides information about Zn–O bonding. In general, the O 1s peak can be deconvoluted into three components as shown in Figure 2.7. 532.2 eV is assigned to oxygen in surface hydroxides, 531.4 eV corresponds to oxygen related defects, and 530.1 eV corresponds to oxygen in ZnO lattice. ^[2]

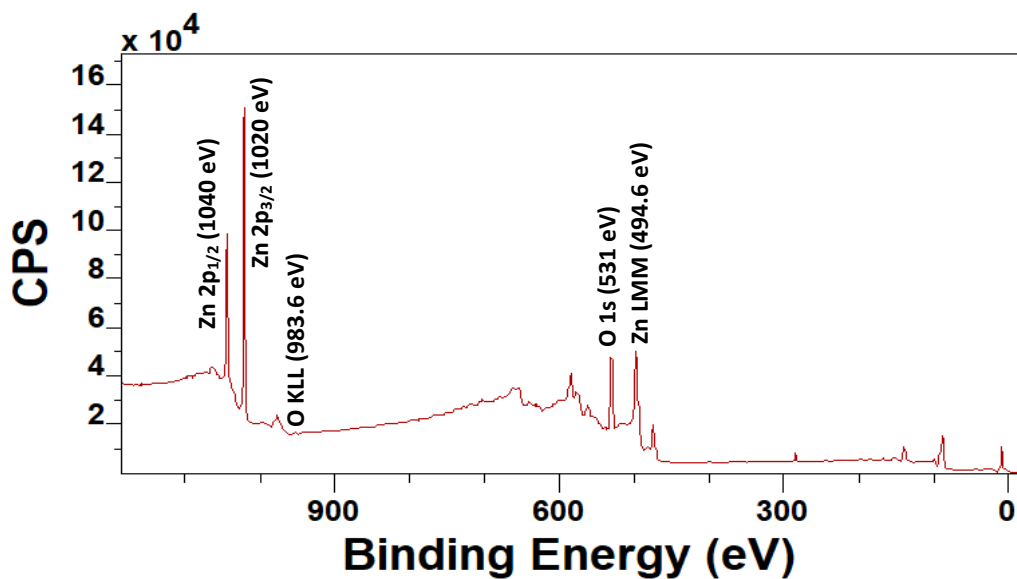


Figure 2.6. A wide scan image of ZnO film derived from ZnMAA precursor.

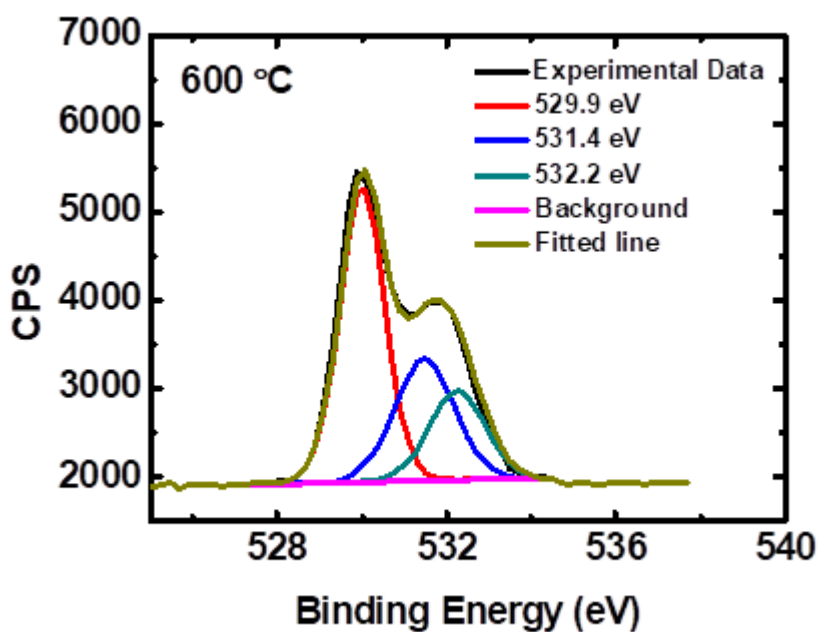


Figure 2.7. Three components peaked at 529.9 eV, 531.4 eV and 532.2 eV are extracted from XPS O 1s spectrum.

2.5.2. Fourier Transform Infrared (FTIR)

Infrared Spectroscopy brings additional information on the chemical functions within the material film by monitoring the vibration modes of molecules. We used here FTIR in a transmission configuration, directly on thin silicon wafer that exhibit suitable transparency in the analysis energy range and Raman

spectroscopy on glass substrates. The FTIR spectrophotometer is a Thermo Scientific Nicolet 8700 FT-IR. Si wafer (thickness = 0.25 μm) were used as substrates. We used a DUV lamp (Hamamatsu high intensity mercury-xenon lamp) equipped with a light guide to proceed the irradiation of the sample so that the optical properties could be measured immediately, in situ, without moving the sample.

Figure 2.7 shows a typical FTIR spectrum of ZnMAA precursor. The broad absorption band ranging from 3200 cm^{-1} to 3700 cm^{-1} corresponding to hydroxyl groups and a small absorption band peaked at 2960 cm^{-1} corresponding to C-H bonding.^[3] The two absorption bands peaked at 1410 cm^{-1} and 1570 cm^{-1} are attributed to COO^- ligands of MAA bond to zinc cations.^[4] The later peaks can thus be used to monitor the presence of the ligands in the thin film.

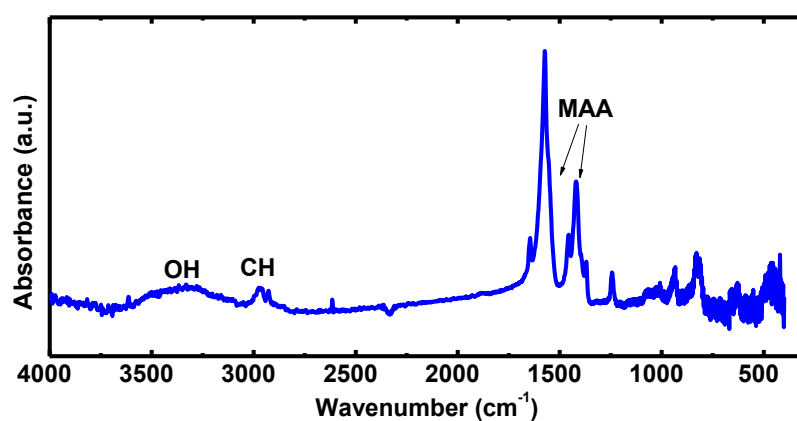


Figure 2.7. A typical FTIR spectrum of ZnMAA precursor.

2.5.3. Raman spectroscopy

Raman spectroscopy analysis was carried out to analyze the lattice and phonon vibration modes in ZnO by using Spectrometer Labrum HR with excitation wavelength of 532 nm. Figure 2.8 shows a typical Raman spectrum of crystalline ZnO film derived from ZnMAA precursor. A sharp peak at 440 cm^{-1} corresponds to ZnO lattice vibration.^[5]

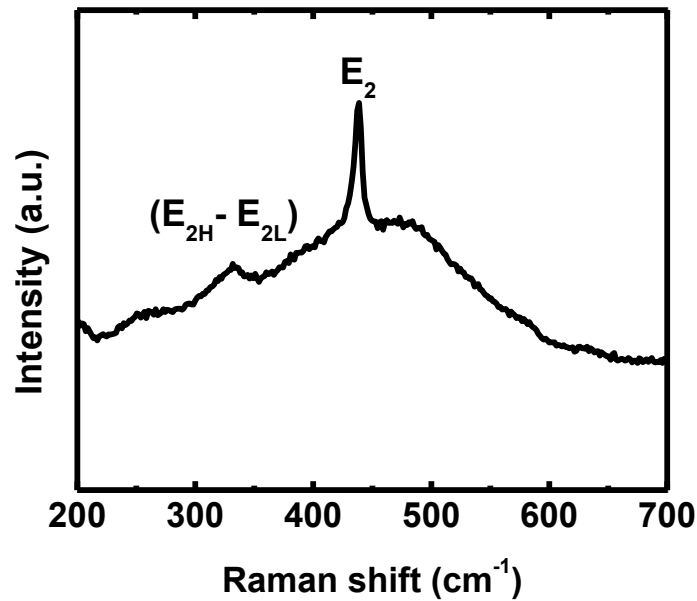


Figure 2.8. A typical Raman spectrum of crystalline ZnO derived from ZnMAA precursor.

2.5.4. X-ray diffraction (XRD)

The crystalline structures of ZnO films were characterized by X-ray diffraction. XRD analysis were performed by using X'Pert MPD PANalytical Bragg Brentano diffractometer (reflexion mode), equipped with a proportional counter, rear graphite (002) monochromator and Cu anode (λ $K\alpha_1$ and $K\alpha_2$). Data were collected in grazing incidence mode, with incidence angle $\omega = 0.5^\circ$. The following acquisition conditions were used: range from $20^\circ 2\theta$ up to $70^\circ 2\theta$, step $0.05^\circ 2\theta$, time per step: 1.8s. Some XRD analysis was also performed by using D8 Discover X-ray diffraction system (Bruker) with Cu K-alpha radiation (1.54 \AA wavelength). Figure 2.9 shows a typical XRD spectrum of poly crystalline ZnO. Diffraction peaks at 2θ values of 31.74° , 34.37° , 36.2° , 47.46° , 56.55° , 62.8° , and 67.96° correspond to the reflection from: 100, 002, 101,102, 110, 103 and 112 crystal planes, respectively.^[6]

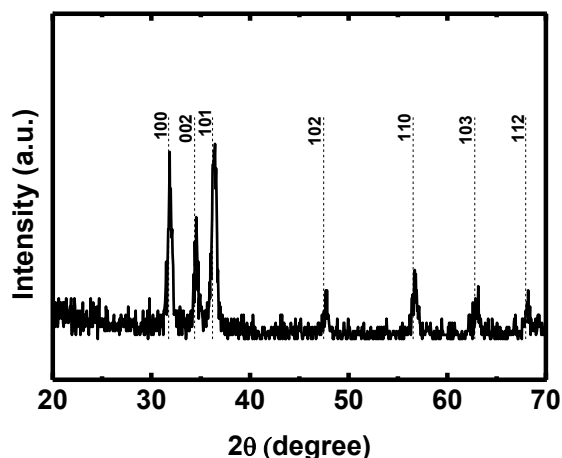


Figure 2.9. A typical XRD spectrum of ZnO film derived from ZnMAA precursor.

2.5.5. Temperature- Programmed Desorption (TPD)

To investigate the modification of the thin film under thermal treatment, we used a homemade temperature- programmed desorption coupled to mass spectrometry analysis (TPD-MS) setup. The samples were placed in a quartz tube in a furnace and heat-treated with a linear heating rate in vacuum. A heating rate of 10 °C/min in the temperature range 25-800 °C was selected. The gases evolved during the heating process were continuously analyzed quantitatively by a mass spectrometer. The total pressure of the gas released during the heat treatment was measured as a function of the temperature using a Bayard-Alpert gauge. This total pressure was then compared with the sum of the partial pressure of the species deduced from the quantitative analysis by mass spectrometry. The total amount of each gas released was computed by time integration of the TPD curves.

2.5.6. Optical measurements

The thicknesses and optical parameters such as refraction index (n) and absorption coefficient (k) were determined by ellipsometer from Horiba-Jobin-Yvon (190 nm-830 nm). For ZnO thin films, the data were fitted with a modified ZnO model. The irradiation was led either by DUV laser or using a DUV lamp (Hamamatsu high intensity mercury-xenon lamp) equipped with a light guide to proceed in situ. Absorption and transmission spectra were obtained by using UV-visible spectroscopy (Lambda 950 UV/VIS Spectrometer from PerkinElmer).

2.6. Thin-film transistor fabrication and electrical measurements

Figure 2.9 shows the structures of thin-film transistors (TFT). ZnMAA precursor solution was spin-coated on a 100nm SiN_x insulator grown on doped Si substrate. After photopatterning and thermal annealing at 500°C in air for one hour, ZnMAA patterns were transformed to ZnO patterns with electrical properties. Al electrodes were then thermally deposited through a shadow mask. The distance between source and drain was defined as 200 μm. The width was approximately equal to the diameter of laser spot (2 mm).

The electrical performance was measured by Agilent E5270B semiconductor parameter analyzer. Threshold voltage (V_T) and field-effect mobility (μ) are extracted from the plot of square root of drain current ($\sqrt{I_D}$) versus gate voltage (V_G) in saturation region according to the equation: $I_D = W/(2L)C_i\mu(V_G - V_T)^2$, where C_i is the capacitance per unit area of the gate dielectric layer ($5.31 \times 10^{-8} \text{F/cm}^2$).

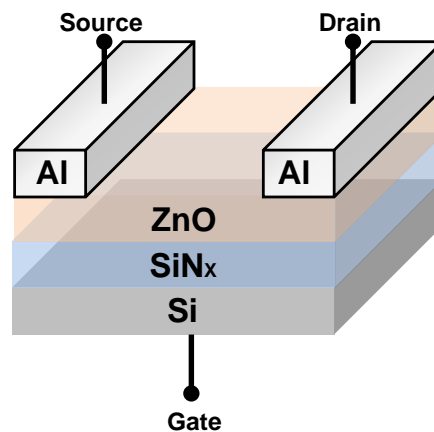


Figure 2.9. Schematic showing the structure of a ZnO TFT device.

2.7. Gas sensing and micro-fluid gas sensing system

As shown in Figure 2.10, the gas sensing properties was measured in a micro-fluid gas sensing chamber. N₂ gas was kept at a fixed flow rate controlled by a mass flow controller. Therefore, the background ambient of the sensing chamber is N₂. The injection and concentration of target gas was controlled by an electrical syringe pump. During gas sensing, the devices were heated up to 200 °C and the electrical properties was monitored by Keithley 2400.

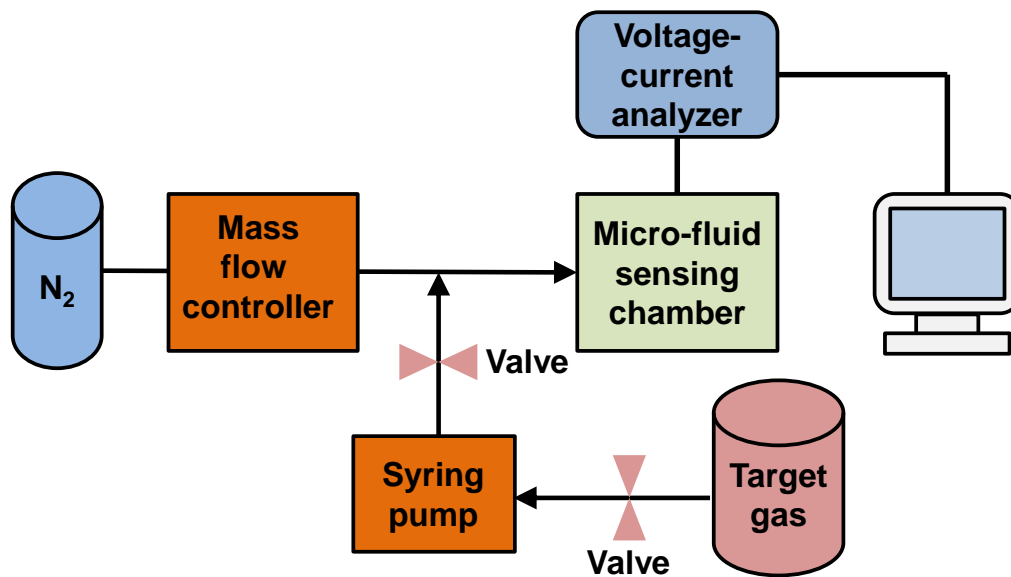


Figure 2.10. Schematic showing the micro-fluid sensing system.

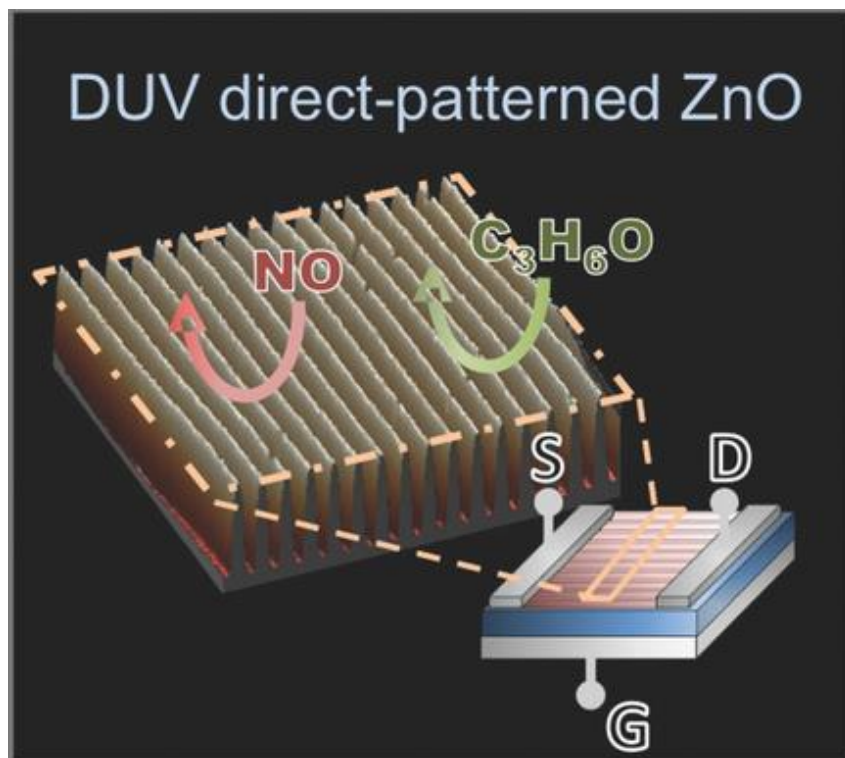
2.8. Magnetic measurements

The magnetic measurements were carried out at IPCMS, by Dr. Silviu Colis. The room temperature magnetic measurement (magnetization loops) were carried out using an alternative gradient field magnetometer (AGFM). The temperature dependent magnetic measurements were performed with a MPMS SQUID-VSM (Quantum Design) magnetometer. The magnetization was recorded at constant field of 500 Oe after a cooling the sample from room temperature under zero magnetic field (ZFC – zero field cooling procedure) or under a field of 500 Oe (FC – field cooling procedure).

2.9. Bibliography

- [1] F. Stehlin, F. Wieder, A. Spangenberg, J. M. Le Meins and O. Soppera, *J. Mater. Chem. C*, 2014, 2, 277.
- [2] Y. H. Hwang, S. J. Seo, J. H. Jeon, B. S. Bae, *Electrochem. Solid-State Lett.* 2012, 15, H91.
- [3] Y. S. Rim, H. Chen, Y. Liu, S. H. Bae, H. J. Kim and Y. Yang, *ACS nano*, 2014, 8, 9680
- [4] L. Li, S. Chakrabarty, K. Spyrou , C. K. Ober, and E. P. Giannelis, *Chem. Mater.*, 2015, 27, 5027
- [5]. M. Marie, S. Mandal , O. Manasreh, *Sensors*, 2015, 15, 18714
- [6] D. Ledwith, S. C. Pillai, G. W. Watson, J. M. Kelly, *Chem. Commun.* 2004, 20, 2294.

Chapter III: DUV-patterned ZnO micro- and nanostructures for electronic applications



Résumé du chapitre III	73
3.1. Introduction.....	74
3.2. Solution synthesis and chemical characterization of photosensitive zinc methacrylate precursor	74
3.2.1. Ellipsometry characterization of DUV-induced photoreaction	75
3.2.2. FTIR characterization	76
3.2.3. XPS characterization	79
3.2.4. Raman spectroscopy	81
3.2.5. XRD analysis	82
3.2.6. TPD.....	83
3.3. DUV-patterned ZnO nanostructures	85
3.4. Electrical and gas sensing properties of DUV-patterned ZnO structures	87
3.4.1. Electrical properties.....	87
3.4.2. Sensor properties.....	89
3.5. Enhancing conductivity of ZnO structures by doping group III elements.....	92
3.6. Conclusion and perspective	93
3.7. Bibliography	94

Résumé du chapitre III

L'objectif principal du Chapitre III est de démontrer la possibilité de micro et nanostructurer le précurseur pour obtenir des micro et nanostructures fonctionnelles de ZnO.

Bien que plusieurs rapports aient démontré que des précurseurs de ZnO pouvaient être mis en œuvre par e-beam ou EUV, aucune propriété électrique n'a été montrée dans les structures, bien qu'elle soit nécessaire pour son application dans des dispositifs électroniques.

Dans ce travail, nous avons développé un précurseur à base de ZnMAA qui présente une excellente photosensibilité à la lumière DUV et permet de produire des motifs haute résolution jusqu'à 300 nm. Les photoréactions induites par la lumière DUV sur le précurseur à base de ZnMAA ont été étudiées par ellipsométrie spectroscopique in situ, analyse FTIR, XPS in situ et des mesures électriques. Les résultats indiquent que l'irradiation DUV est efficace pour générer la réticulation nécessaire pour la structuration mais la conversion en réseau M-O-M est incomplète et une forte concentration de composés organiques subsiste, ce qui explique que les propriétés électriques ne sont pas bonnes.

Après un recuit thermique à une température supérieure à 400 ° C à l'air pendant une heure, la partie organique peut être complètement éliminée et les réactions de condensation sont suffisamment avancées pour obtenir ZnO avec des propriétés semi-conductrices. Pour montrer que la technique proposée peut être utilisée dans la fabrication de dispositifs, nous avons démontré la fabrication d'un transistor à base de nanofils ZnO avec une mobilité de 0,45 cm² / Vs, une tension de seuil de 3,4 V et une oscillation sous-seuil de 0,46 Vdec⁻¹.

Nous avons également montré que les nanofils ZnO peuvent être utilisés comme capteurs de gaz. Une réponse en courant a été observée lors de l'exposition à l'acétone et au NO.

Enfin, nous avons amélioré la conductivité du ZnO par dopage avec 2% de Al³⁺. Ces résultats suggèrent le potentiel de cette approche pour la production de dispositifs et de systèmes intégrant ZnO à l'échelle nanométrique, en utilisant de tels précurseurs à base de ZnMAA et la lithographie DUV.

3.1. Introduction

Although several reports demonstrated high resolution ZnO patterns by e-beam or EUV lithography, no electrical property was shown. No experimental proof of semiconducting properties of these structures is demonstrated, although it is necessary for its applicability in electronic devices. In this study, an in-depth investigation to photochemical reactions is carried out. Electrical properties, and gas sensing behaviors of ZnO micro-and nanostructure are shown to illustrate the potential of this approach for practical applications. Structures are obtained by direct-patterning by DUV laser (193 nm wavelength).

DUV lithography has several advantages over other lithography technologies, including that it is compatible with nanoscale patterning smaller than 50 nm, it is widely used in today's semiconductor industry, and no vacuum system is needed. Furthermore, DUV direct patterning avoids multistep processes, showing excellent controllability on dimension and position. Zinc methacrylate (ZnMAA) was chosen as a photosensitive precursor due to its high stability and because C=C bond in the molecular structure which was proven to be photosensitive to light in DUV range.^[1] In this chapter, we used ZnMAA to form ZnO structures from microscale to nanoscale dimension by a direct-patterning method. Detailed chemical analysis including X-ray photoelectron spectroscopy (XPS) analysis, *in situ* Fourier transform infrared (FTIR) spectroscopy analysis, temperature programmed desorption (TPD) analysis and *in situ* ellipsometry analysis were performed to investigate the photoreactions in ZnMAA precursor induced by DUV irradiation. Material final structure was also studied by Raman spectroscopy and X-ray diffraction (XRD). In addition, electrical measurements were carried out to characterize electrical properties of DUV-patterned ZnO structures.

3.2. Solution synthesis and chemical characterization of photosensitive zinc methacrylate precursor

Figure 3.1 shows the schematic diagram of the formation of ZnO patterns starting from the sol-gel based on ZnMAA precursor used here. In solution, zinc ions are chelated with methacrylic acid (MAA) and monoethanolamine (MEA). These ligands act as stabilizer to decrease the kinetics of condensation reactions leading to the growth of ZnO, thus preventing precipitation. Their role is also important to insure a limited size grain and a resulting low surface roughness after spin-coating. Indeed, without MEA, high growth rate of ZnO results in roughness up to several micrometers once the

solution was spin-coated on the substrate, making the subsequent DUV-patterning impossible.

After spin-coating, the sol-gel films are exposed to DUV light. Although no previous study illustrated the underlying photoreactions of ZnMAA irradiated by DUV light, based on other studies focusing on the effect of DUV to transition metals complexed with acid carboxylic compounds, we establish the assumptions as follows.^[1] The energy of DUV light is absorbed by ZnMAA causing π to π^* electronic transition in the complex. A dissociative state can be reached, and Zn-MAA bonds are gradually decomposed (photocleavage reaction). Hydroxyl (-OH) groups formed from reaction of unprotected metal center with water are able to connect zinc via oxo-bridges. As a result, the ZnMAA gel film is transformed into amorphous ZnO thin film which is insoluble in developer (1-propanol), making it possible to direct pattern ZnO by DUV lithography. To obtain crystallized ZnO, a thermal annealing in air is required as a final step.

The aim of this section is to further investigate the DUV-induced modifications leading to ZnO thin film.

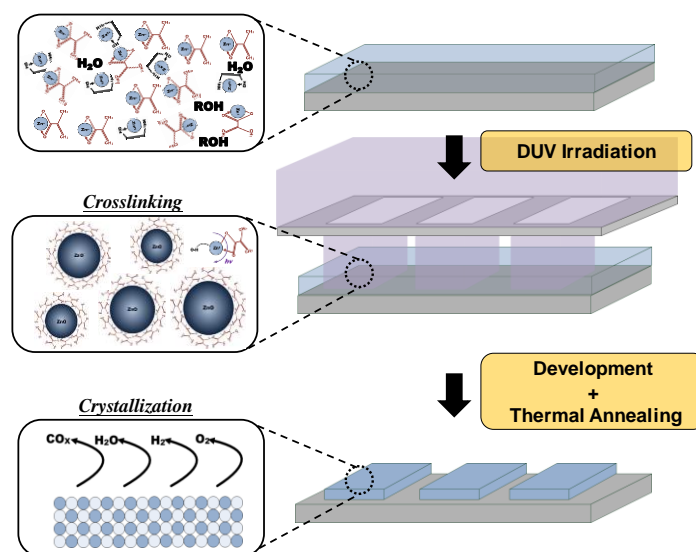


Figure 3.1. (The process of DUV-direct patterning; the solution is spin-coated on the substrate, irradiated by DUV light, developed in 1-propanol for 30 s and annealed at 600 °C in air for one hour.)

3.2.1. Ellipsometry characterization of DUV-induced photoreaction

In order to verify these assumptions and to clarify the photoreactions provoked by DUV irradiation, ellipsometry analysis was performed. The light induced modification was studied *in situ* since the sample could be irradiated in the ellipsometer by a DUV lamp (90% 254 nm and 10% 193

nm). Figure 3.2a shows film thickness and refractive index (n at 633 nm) as a function of DUV irradiation time. Film thickness was gradually decreasing, and, at the same time, the refraction index was increasing, showing a photo-induced densification. In addition, as shown in Figure 3.2b, the sol-gel film absorbance in the DUV range, related to the Zn-MAA bond was decreasing with DUV exposure, confirming the photolysis of metal-ligand bond. To understand whether the decrease of k is owing to formation of ZnO, we compared the results obtained from thermally annealed samples. Absorption spectra corresponding to different annealing temperatures are shown in Figure 3.2c. As the annealing temperature increased, absorption spectrum gradually extended to higher wavelength. After annealing at 600 °C in air for one hour, a clear bandgap of ~ 3.3 eV indicates a ZnO thin film, and the absence of optical bandgap after DUV irradiation (Figure 3.2b) implies these changes were not due to the growth of crystalline ZnO.

3.2.2. FTIR characterization

To clarify the photoreaction taking place in ZnMAA gel film under DUV irradiation, in situ FTIR analysis was performed to investigate the change of bonding between Zn and MAA. As shown in Figure 3.2d, two bands were observed before DUV irradiation: the first one is centered at 1570 cm^{-1} and second one around 1416 cm^{-1} . They are referred respectively to the asymmetric and symmetric stretching mode of COO^- group bonded to Zn^{2+} .^[2] FTIR can thus be used to follow the photocleavage of Zn-MAA bond under DUV irradiation. The absorption bands were reduced rapidly of 30% in the first 200 s of DUV irradiation. As the irradiation time was extended to 2000 s, only a slight decrease of absorption band was observed for an irradiation interval between 200 s to 2000 s, implying that DUV light is unable to fully cleave the bonding between Zn and MAA. Figure 3.3b shows the decrease of O-H band ($2500\text{-}3300\text{ cm}^{-1}$) under DUV exposure, which is owing to the occurrence of DUV-induced condensation reactions. Figure 3.3c shows FTIR spectra obtained from gel films annealed at different temperatures. Through a comparison between Figure 3.3a and 3.3c, we found that the effect of 100 °C thermal annealing is similar to a 200 s DUV irradiation. A 2000 s DUV irradiation has an effect similar to 200 °C. As annealing temperature is further increased to 400 °C, the absent of absorption bands indicates Zn-MAA bonds in the gel film were cleaved completely.

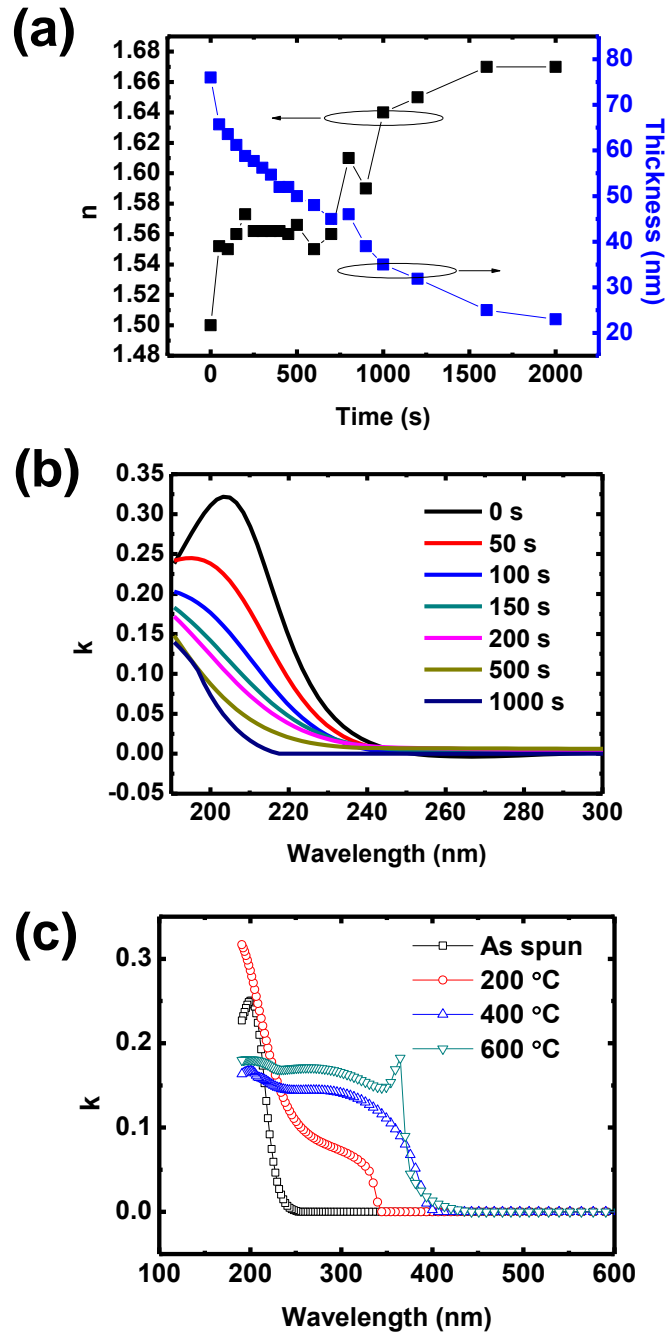


Figure 3.2. (a) Evolution of refractive index at 633 nm (n) and thickness of the ZnMAA thin film as a function of DUV irradiation time. (b) Evolution of extinction coefficient (k) with different DUV irradiation times (c) Evolution of extinction coefficients (k) with different annealing temperatures.

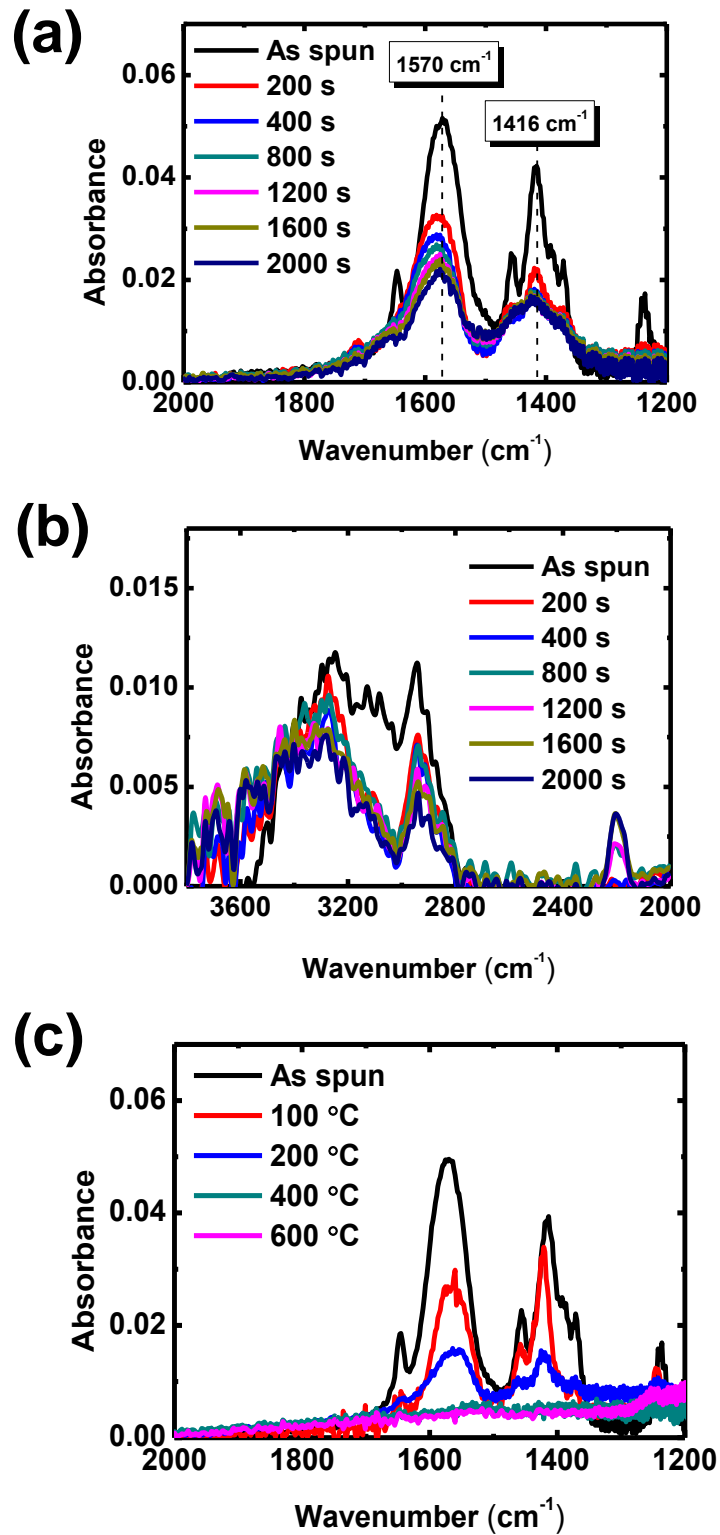


Figure 3.3. (a) Evolution of FTIR spectrum (2000 cm⁻¹ to 1200 cm⁻¹) with different DUV irradiation times. (b) Evolution of FTIR spectrum (3800 cm⁻¹ to 2000 cm⁻¹) with different DUV irradiation times. (c) Evolution of FTIR spectrum (2000 cm⁻¹ to 1200 cm⁻¹) with different annealing temperatures.

3.2.3. XPS characterization

To have an in-depth understanding of metal-oxygen (M-O) bonds variations due to DUV irradiation as well as thermal treatment, XPS analysis was performed. All binding energies were calibrated to C1s peak at 284.6 eV. O1s spectrum provides information about local-bonding environments around oxygen in metal oxide film. In metal oxides, O1s spectrum can be deconvoluted in three components at 532.2 eV, 531.4 eV and 530.1 eV. 532.2 eV is assigned to oxygen in surface hydroxides, 531.4 eV corresponds to oxygen related defects, and 530.1 eV corresponds to oxygen in M-O lattice.^[3] The XPS results are given in Figure 3.4 and Table 3.1. For all samples treated by DUV, the main contribution is linked to oxygen related defects (531.4 eV). DUV irradiation leads to poorly condensed oxide materials. For the sample treated with 600 s DUV irradiation, due to the occurrence of condensation reactions, all surface hydroxides (531.4 eV) were eliminated; however, high proportion of defective M-O lattice (89.62%) indicates that DUV irradiation has a limited ability to generate well-connected M-O lattice for carrier transport. In comparison, in thermally-annealed samples, the proportion of well-connected M-O lattice is increased with annealing temperature. The ratios of well-connected M-O lattice are 22.32%, 50.93% and 64.63% for the samples annealed at 200 °C, 450 °C and 600 °C respectively. Atomic concentrations of Zn, O, C, and N in percentage were also extracted from XPS spectra (Figure 3.5). After 600 s DUV irradiation, the content of C was largely reduced from 50.16% to 21.611%. Fabrice Stehlin *et al.* described a reaction pathway of DUV-mineralization process for MAA modified titanium tetraisopropoxide (TiOMAA) as follows.^[1] Under DUV irradiation, MAA dissociates from TiOMAA and then decomposes into CO₂ and carbon alkane radicals. We suppose the same reaction of MAA decomposition occurred in ZnMAA gel film during DUV irradiation and the decrease in carbon content can be explained by the escape of CO₂. For the thermally-annealed samples, C content decreases with the increase of annealing temperature as shown in Figure 3.5. In addition, as revealed by the FTIR analysis, Zn-MAA bonds can be cleaved thoroughly after annealing at temperature above 400 °C. As shown in Figure 3.5, 7.93% of C was observed from the sample annealed at 600 °C, which implies that those dissociated MAA molecules were not completely removed from the thin film.

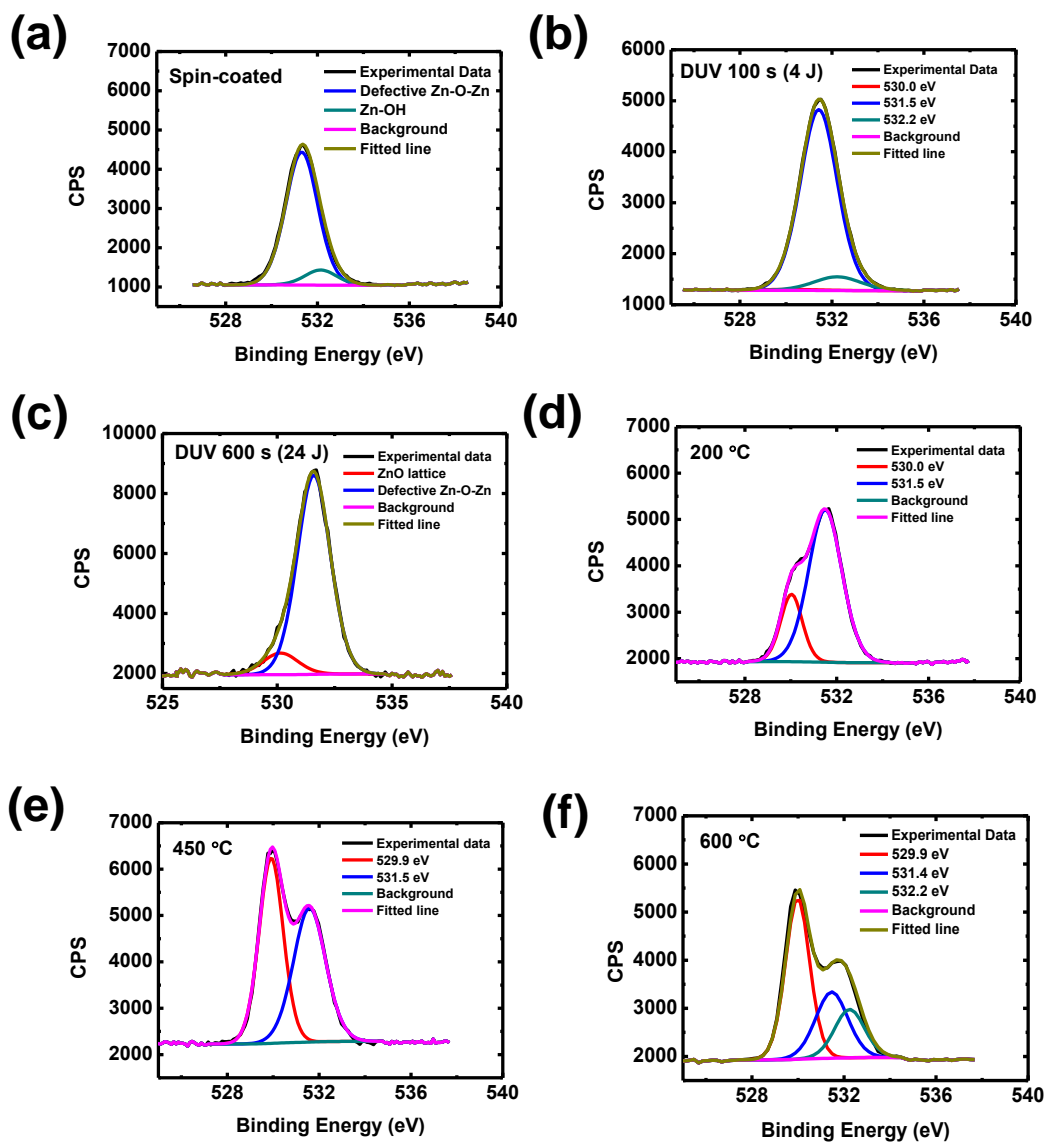


Figure 3.4. XPS O1s spectrum of (a) spin-coated ZnMAA gel film, (b) ZnMAA gel film after 100 s DUV irradiation, (c) ZnMAA gel film after 600 s DUV irradiation, (d) ZnMAA gel film after annealing at 200 °C in air for one hour and (e) ZnMAA gel film after annealing at 450 °C in air for one hour. (f) ZnMAA gel film after annealing at 600 °C in air for one hour.

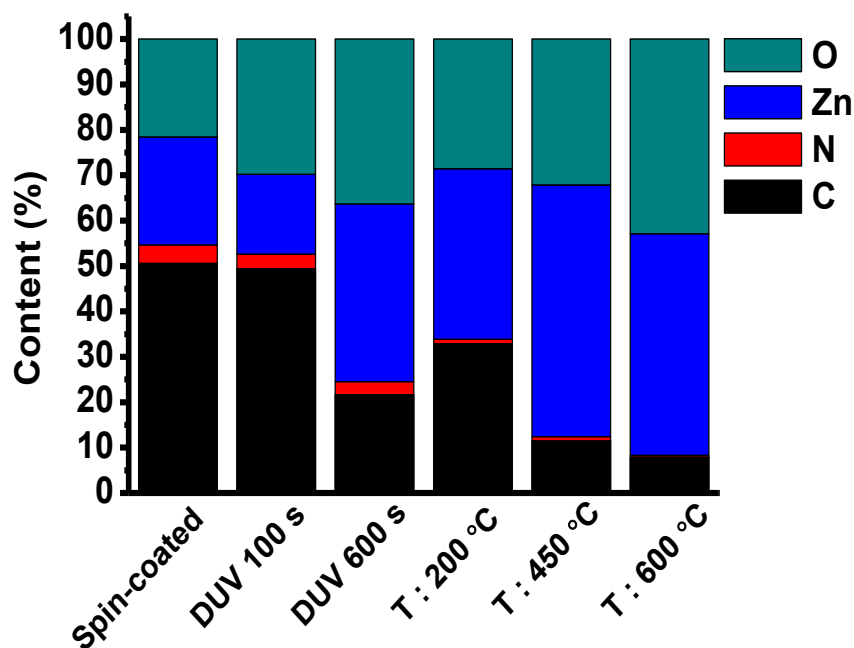


Figure 3.5. Percentage atomic concentrations of O, C, N and Zn extracted from the XPS spectra.

Table 3.1. Analysis of oxygen in DUV-irradiated and thermally-annealed ZnMAA gel films are extracted from XPS spectra and presented in percentage (%) for comparison.

Sample	Metal oxide lattice (530.1 eV)	Vacancy and lattice defect (531.4 eV)	Surface hydroxide (532.2 eV)
Spin-coated	0%	89.79%	10.21%
DUV 100 s (4 J)	0.82%	90.44%	8.74%
DUV 600 s (24 J)	10.38%	89.62%	0%
200 °C/air/1h	22.32%	77.68%	0%
450 °C/air/1h	50.93%	49.07%	0%
600 °C/air/1h	52.07%	28.49%	19.44%

3.2.4. Raman spectroscopy

Raman spectroscopy analysis was performed to confirm the formation of ZnO derived from ZnMAA precursor. As shown in Figure 3.6, four distinct peaks at 850 cm^{-1} , 938 cm^{-1} , 1005 cm^{-1} and 1074 cm^{-1} in the spectrum of spin-coated ZnMAA film were observed, which can be attributed to the vibration of organic species. After 600 s DUV irradiation, no peak can be observed in the spectrum. It thus confirms the decomposition of organic compounds under DUV irradiation. However, no peak indicates the formation of crystalline ZnO, implying no nucleation and growth of ZnO crystal occurred

during DUV irradiation. On the other hand, for ZnMAA film annealed at 500 °C for one hour, a clear peak appears in at 434 cm^{-1} , confirming the formation of crystallized ZnO.^[4]

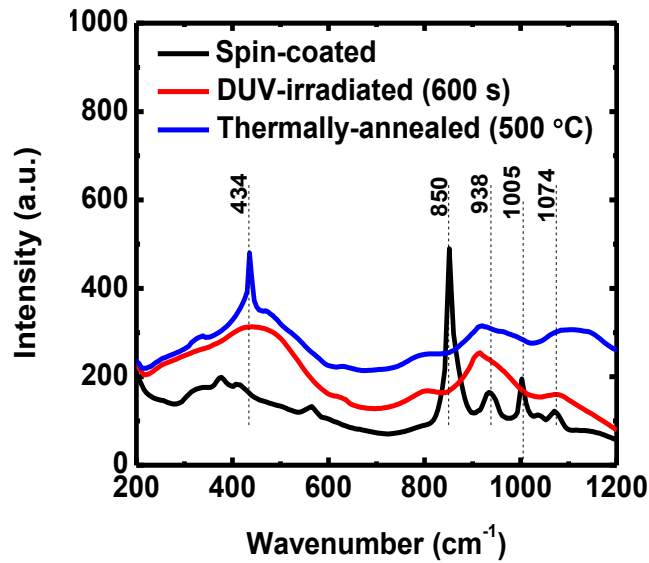


Figure 3.6. Raman spectra of spin-coated ZnMMA gel film, DUV-irradiated ZnMAA gel film (600 sec) and thermally-annealed ZnMAA gel film.

3.2.5. XRD analysis

The crystalline structure was further analyzed by XRD. As shown in Figure 3.7, grazing incidence X-ray experiment confirmed the presence of crystallized ZnO (ICDD PDF N°00-036-1451) indicating ZnMAA film was transformed into polycrystalline ZnO film with Wurzite 2H crystal structure type.

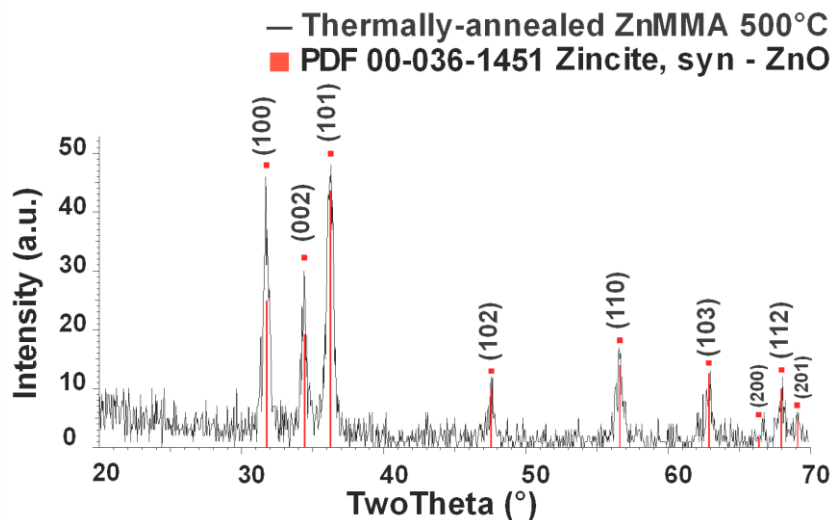


Figure 3.7. XRD pattern of thermally-annealed ZnMAA gel film.

3.2.6. TPD

All ellipsometry analysis, FTIR analysis, XPS analysis and Raman spectroscopy analysis revealed that thermal annealing at temperature above 400 °C is necessary to remove organic part in ZnMAA gel films. To further investigate the decomposition of organic compounds within ZnMAA gel films during thermal annealing, TPD (temperature programmed desorption) analysis was performed on a spin-coated ZnMAA gel film. As shown in Figure 3.8a, two peaks indicate organic compounds thermally decomposed into gaseous substances. One small peak is observed at 190 °C and another much higher peak is at 465 °C. Hypothetically, the small peak at 190 °C is attributed to unbonded or weakly-bonded MAA molecules which can easily dissociate from the thin film and turn into small volatile species. To verify this assumption, we extracted TPD diagram of MAA as shown in Figure 3.8b. A desorption peak of MAA reaching its maximum at 211 °C supports our assumption that unbonded and weakly-bonded MAA molecules were thermally decomposed at ~200 °C. Another peak at 465 °C might be attributed to well-bonded MAA molecules which decomposed at a much higher temperature. To investigate the effect of DUV irradiation, we performed TPD analysis on a spin-coated ZnMAA gel film that had been irradiated by DUV light for 600 s (Figure 3.8c). At the beginning of heating, H₂O resulting from DUV-induced condensation reactions was released and reached its maximum at ~300 °C. To clarify if MAA still present in the sample, we extracted MAA from TPD data; however, no MAA can be characterized, which can be explained as follows. After a 600 s DUV irradiation, MAA was decomposed into CO₂ and carbon alkane radicals; thus, no intact MAA of molar mass 86 (g/mol) was detected by the mass spectrometer. In addition, DUV irradiated sample shows most of its desorption peaks at temperatures lower than 465 °C, which implies organic compounds irradiated by DUV light were easier to be thermally decomposed than those without DUV irradiation. However, a high CO₂ desorption peak appears at 550 °C. It could be assigned to CO₂ produced by photochemical decomposition of MAA and complexed to Zn. Several studies focusing on photochemical activation of metal oxide sol-gel films indicated that a moderate heating during DUV irradiation is helpful to remove volatile organic compounds and the formation of M-O-M network.^[5,6] Since we performed DUV irradiation at room temperature without unintentional heating, some products resulting from MAA decomposition, might be alkane radicals, kept staying in the gel film, tending to bond with nearby molecules. The interaction is complicated and would require a more detailed investigation to correlate each desorption peaks to each type of chemical bonding.

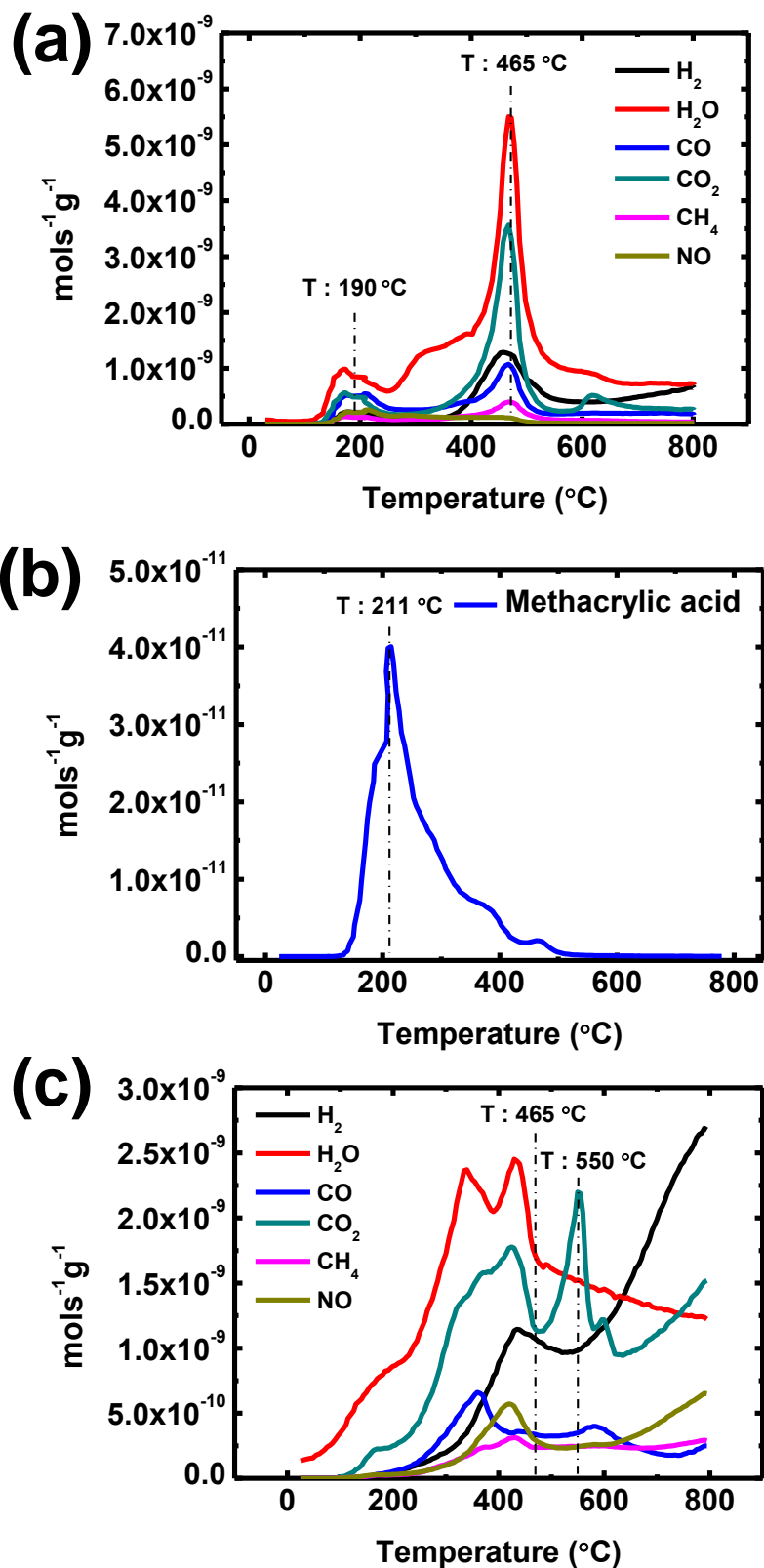


Figure 3.8. (a) TPD spectrum of spin-coated ZnMAA gel film. (b) MAA evolution curve as a function of temperature. (c) TPD spectrum of DUV-irradiated ZnMAA gel film.

3.3. DUV-patterned ZnO nanostructures

To evaluate the performance of ZnMAA precursor used as a negative tone resist for DUV lithography, we firstly synthesized ZnMAA solution and spin-coated on silicon substrates. Then, the homemade optical system was employed to produce DUV laser interference patterns. The period of interference patterns was as small as 600 nm. Top view atomic force microscopy (AFM) images and cross-sectional profiles of ZnMAA nanostructures patterned by DUV with different energy doses from 200 mJ/cm² to 400 mJ/cm² are shown in Figure 3.9. No distortion or residue between lines was observed. The results show excellent photo-patterning ability of the ZnMAA precursor and the potential of using ZnMAA precursor combined with DUV lithography for nanofabrication. However, as revealed by XPS analysis, DUV irradiation is unable to create well-connected M-O-M network for carrier transport, so ZnMAA patterns produced by DUV lithography are insulating. In order to remove organic compounds and construct well-connected M-O-M network for carrier transport, thermal annealing is required as a final step. The structural change of DUV-patterned nanowires after thermal annealing is shown in Figure 3.10a. The height of ZnMAA nanowires shrank drastically from ~70 nm to ~10 nm after thermal annealing, which is owing to removal of organic compounds inside the structures. The top view AFM image of ZnO nanowire array is shown in Figure 3.10b. The detailed study of the photopatterning process will be given in the next Chapter.

Nanowires with three-dimensional cross-sectional profile can be integrated into high-performance FETs such as trigate FET, wrap-gate FET, and gate-all-around FET.^[7-9] In comparison to ZnO nanowires synthesized by metal-organic chemical vapor deposition or chemical vapor transport,^[10,11] ZnO nanowires fabricated by DUV light interference show a thin-film like cross-sectional profile with height to width ratio far less than 1. These structures are unable to show the potential of DUV direct patterning for fabricating three-dimensional devices. We therefore made an initial attempt to fabricate three-dimensional ZnO nanowires with ZnMAA precursor and DUV lithography. In order to increase the aspect ratio, the thickness of ZnMAA gel film was increased to ~250 nm for DUV-patterning. Thickness of ZnMAA gel film could not be increased to more than 250 nm due to the absorption in the material at 193 nm. Because the intensity of DUV light attenuates from the top to the bottom of the film, there is a thickness limitation for ZnMAA gel films that can be performed by DUV-patterning. When DUV-patterning is applied to a gel film thicker than 300 nm, owing to not enough crosslinking at the bottom region of the film, most of the DUV irradiated parts are inevitably being removed from the substrate during the development. We then patterned ZnMAA gel

films by DUV light passing through a binary mask of 1 μm period. The top view AFM image of ZnMAA structures are shown in Figure 3.11a. After thermal annealing at 600 $^{\circ}\text{C}$ in air for one hour, besides a vertical shrinkage from ~ 250 nm to ~ 140 nm and a lateral shrinkage from ~ 650 nm to ~ 350 nm, no breakage, distortion and residue was observed from the resulting nanostructures. (Figure 3.11b and 3.11c) We compare the profile of a single nanowire to the one made by DUV light interference (600 nm period) as shown in Figure 3.11c. Unlike patterned by laser interference showing a thin-film like profile with a height to width ratio ~ 0.025 , ZnO nanowires patterned by binary mask shows a three-dimensional profile with a height to width ratio ~ 0.4 . In addition, ~ 300 nm line width of the DUV-patterned ZnO nanowires is comparable to the diameters of various kinds of nanowires prepared by other methods.^[12-14]

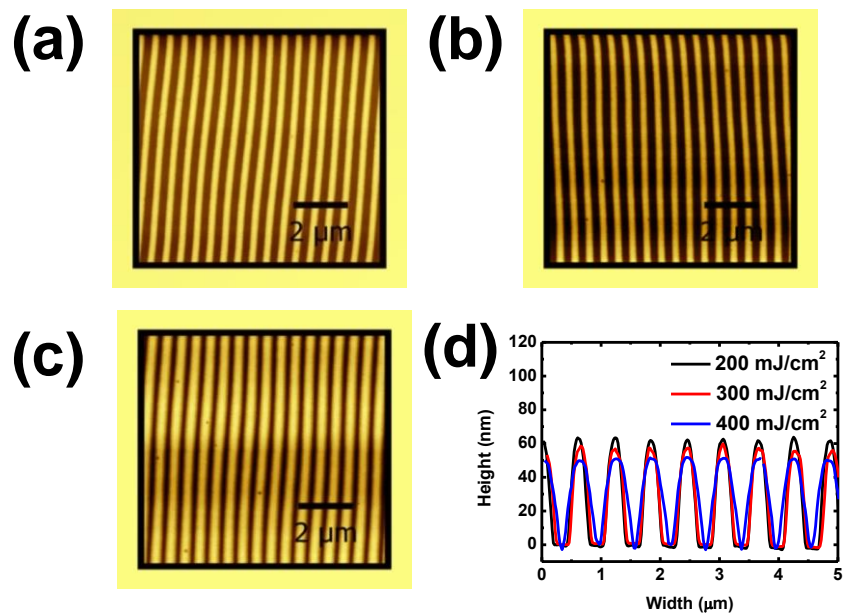


Figure 3.9. (a) Top view AFM image of ZnMAA nanostructures patterned by DUV laser interference with energies of 200 mJ/cm^2 , (b) 300 mJ/cm^2 and (c) 400 mJ/cm^2 . (d) Cross-sectional profiles of ZnMAA nanostructures.

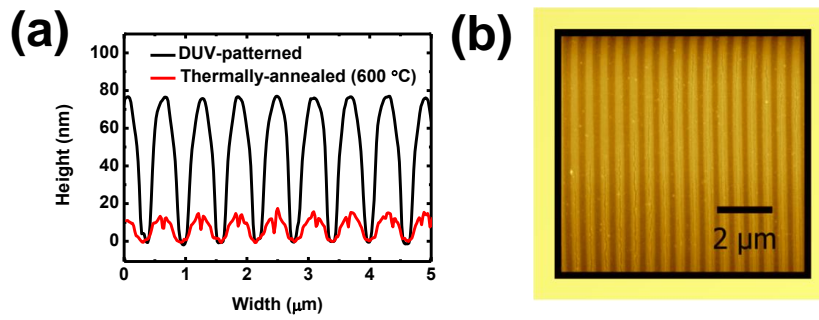


Figure 3.10. (a) Cross-sectional profiles of ZnMAA nanowires before and after thermal treatment. (b) Top view AFM image of ZnO nanowires formed after 600 °C thermal annealing in air for one hour.

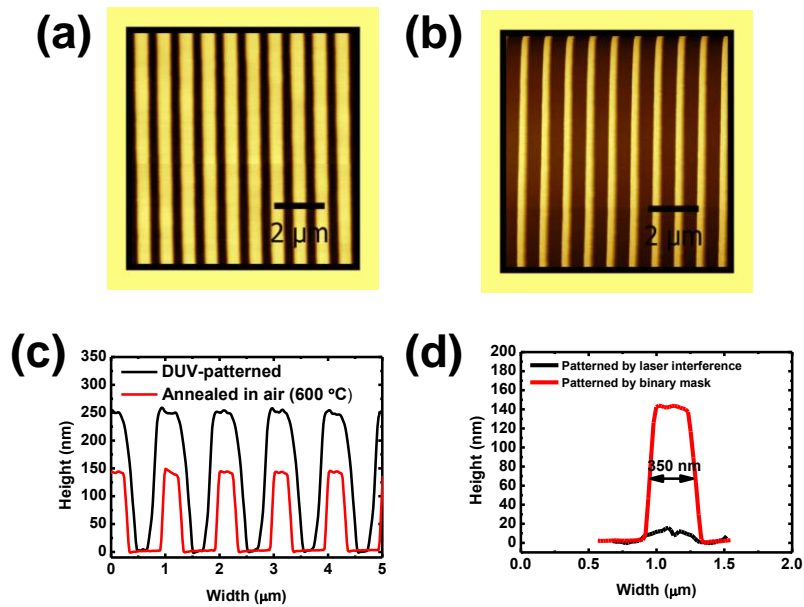


Figure 3.11. (a) DUV-patterned ZnMAA periodic lines (1 μm period). (b) ZnO periodic lines (1 μm period). (c) Cross-sectional profiles of ZnMAA and ZnO nanostructures. (d) Cross-sectional profiles of ZnO nanowires fabricated by DUV laser interference and by using a binary mask of 1 μm period.

3.4. Electrical and gas sensing properties of DUV-patterned ZnO structures

3.4.1. Electrical properties

To activate electrical properties in DUV-patterned ZnMAA structures, thermal annealing is required to remove organic compounds embedded in the structures. According to the results of

chemical analysis discussed previously, ~ 400 °C is required to completely remove organic ligands; therefore, we expect that semiconducting ZnO structures can be obtained after a thermal annealing above 400 °C. To investigate how thermal annealing affects charge transport in ZnMAA patterns we fabricated thin-film transistors (TFTs) with ZnMAA thin-films as active layers which were patterned by DUV irradiation and then annealed at different temperatures from 300 °C to 600 °C in air for one hour. Their transfer characteristics are shown in Figure 3.12a. The TFT annealed at 400 °C began to show semiconducting behavior. However, due to a large amount of defects inside the ZnO thin film, the on/off ratio is only $\sim 10^2$. As the annealing temperature was increased to 600 °C, the ratio of organic compounds can be reduced to less than 10% and a high proportion of well-connected M-O-M network can be generated in the ZnO thin film as revealed by XPS analysis. This leads to a better TFT performance with an on/off ratio up to $\sim 10^5$. To demonstrate that by using ZnMAA precursor combined with DUV lithography ZnO nanostructures can be easily produced and integrated into nanoscale devices, a bottom-gate top-contact ZnO nanowire transistor was fabricated as illustrated in Figure 3.12b. The ZnO nanowires were derived from ZnMAA nanowires patterned by DUV interference lithography. After thermal annealing at 600 °C in air for one hour, organic compounds in ZnMAA nanowires can be removed completely, leading to the formation of ZnO nanowires. After depositing Al electrodes, electrical properties of the ZnO nanowire transistor can be measured. The transfer characteristic and output characteristic are shown in Figure 3.12c and Figure 3.12d. The device exhibits the highest mobility of $0.45 \text{ cm}^2/\text{Vs}$, threshold voltage of 3.4 V, subthreshold swing of 0.46 Vdec^{-1} and on-off ratio of 2.79×10^6 . In previous studies, zinc acetate was usually used as precursor for the fabrication of ZnO devices. To the best of our knowledge, no report was found using ZnMAA as precursor to fabricate ZnO field-effect transistors (FET). Here, we demonstrate DUV-patterned ZnO nanowire transistor of smallest channel width (300 nm) with the use of ZnMAA-based precursor. It's noteworthy that, in our previous work, Hung-Cheng Lin *et al.* have demonstrated DUV direct-write IGZO nanowires of 300 nm line-width; however only electrical performance of direct-write IGZO TFTs with dimensions larger than $5 \mu\text{m}$ is exhibited in the article. Furthermore, the height of IGZO nanowires is only 16 nm before thermal annealing. After thermal annealing, the height of nanowires could shrink to a few nanometers which may cause non-uniformity in fabrication and instability in device operation.^[15]

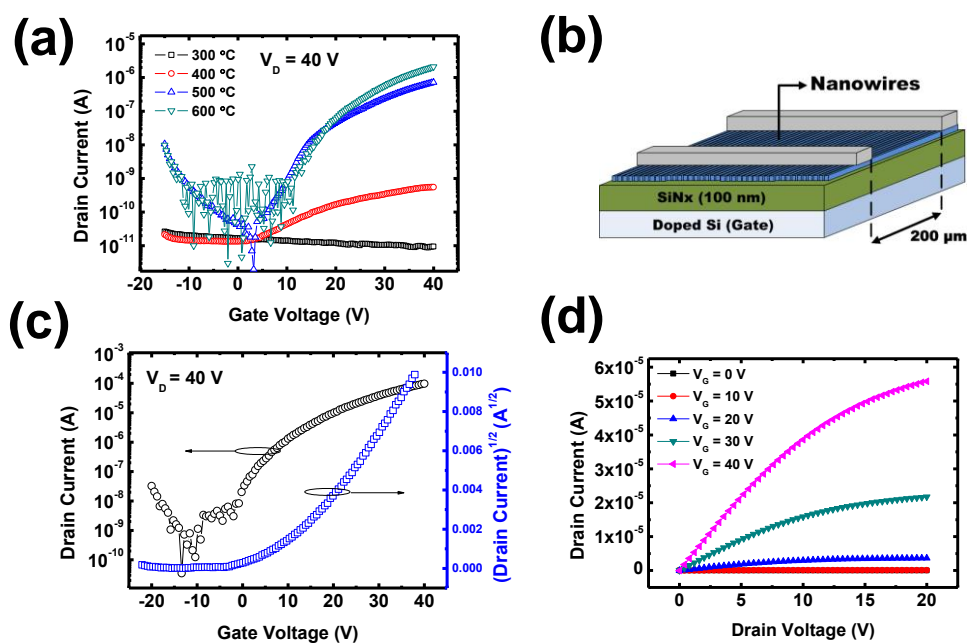


Figure 3.12. (a) Transfer curves of DUV-patterned ZnO thin-film transistors annealed at different temperatures. (b) Schematic showing a bottom gate, top contact ZnO nanowire transistor. (c) Transfer and (d) output characteristics of ZnO nanowire transistor.

3.4.2. Sensor properties

Due to their high surface-to-volume ratio and desirable electrical properties, there has been an increasing interest of ZnO nanowires for biosensor applications. During sensing procedure, the analytes absorb on the surface of ZnO nanowires acting as charge-trapping centers or donors which are responsible for the variation of conductivity. The concentration of analytes therefore can be detected by reading the change of current magnitude as a function of time. Moreover, nanowire has extremely high sensitivity with the detection limit able to monitor a single molecule.^[16,17] Here, the gas sensing behaviors of DUV direct-patterned ZnO nanowires (profile as shown in Figure 3.10a and 3.10b) were demonstrated for the first time. Many previous works reported that ZnO is very sensitive to acetone; thus, acetone was chosen as a target gas in our experiment. The gas sensing experiment was carried out in microfluid sensing chamber with nitrogen (N₂) as background ambient (N₂ flow rate: 0.5 L/min). The sample was heated up to 200 °C during sensing to acetone as shown in Figure 3.13. Two types of resistive sensors were prepared and compared: DUV-patterned ZnO thin-film sensor (STD device) and DUV-patterned ZnO nanowire sensor (NWs device) as shown in Figure 3.14a. The thickness of STD and NWs devices were both around 10 nm. We controlled voltage bias to fix the sensing current at microampere level. After the current became stable, 10 ppm acetone was introduced into the sensing

chamber. A decrease of current was observed for both NWs and STD devices as shown in Figure 3.14b. Generally, when ZnO is exposed to acetone, a positive current response (current increases) is expected due to the removal of oxygen species on the surface of ZnO.^[18] In our work, however, we observed a negative current response (current decreases), which can be explained as follows. Heating in N₂ ambient can reduce oxygen species on the surface of ZnO.^[19] Without oxygen to oxidize acetone into carbon dioxide, acetone molecules absorbed on the surface of ZnO can act as electron trapping centers due to their negative electron affinity. These traps reduce the number of free carriers and therefore a current decrease was observed. In addition, we observed that, in comparison to the NWs device, the STD device had an unstable current decrease during a 30 s exposure to 10 ppm acetone (Figure 3.14b). To explain this observation, we assume that acetone molecules create depletion regions around themselves once contact to the surface of zinc oxide as show in Figure 3.14c. The current path from one contact to another contact was then gradually blocked by these depletion regions during the exposure to acetone. Moreover, current flowing in NWs device is expected to be easily blocked by the depletion regions of acetone molecules. Several acetone molecules are able to connect their depletion region to each other, forming a larger depletion region than the width of a single nanowire (Figure 3.14c), so the current must go through these depletion regions of higher resistivity, which ensures a stable current decrease. On the other hand, the pending of current decrease observed in the STD device can be attributed to nonuniform distribution of acetone molecules in the sensing area. As shown in Figure 3.14c, the paths uncovered by depletion regions are of lower resistivity and may slow down the rate of current decrease during exposure to acetone. Even though these leakage paths can be blocked by depletion regions after absorbing more acetone molecules on the surface of ZnO, they may cause false judgement toward sensing results. We can, therefore, conclude that NWs device has a better sensing performance than STD device. Figure 3.15 shows the sensing response of NWs device to acetone and nitrogen monoxide (NO). Same as acetone, we observed a negative current response when sensing to 5 ppm NO (530 s to 590 s). This observation can be explained as follows. Since NO is a strong oxidation gas, during NO exposure, free electrons on the surface of ZnO were captured by NO molecules and the decrease of free electrons resulted in a current decrease.^[20] To make sure that the sensing response only comes from target gas, we purged N₂ into sensing chamber (710 s to 790 s) through the tube for the input of target gas at a flow rate of 50 cc/min and kept background N₂ flowing at the same time. No significant change was observed, showing that the change of N₂ flow doesn't influence the sensing response.

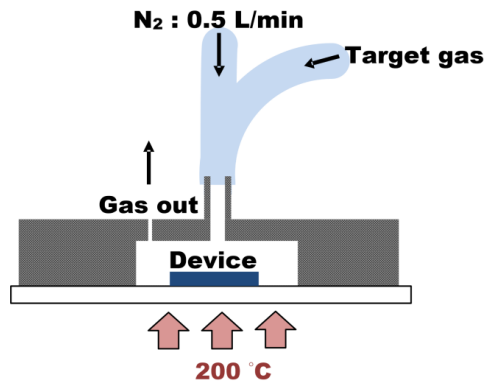


Figure 3.13 Schematic diagram of gas sensing system.

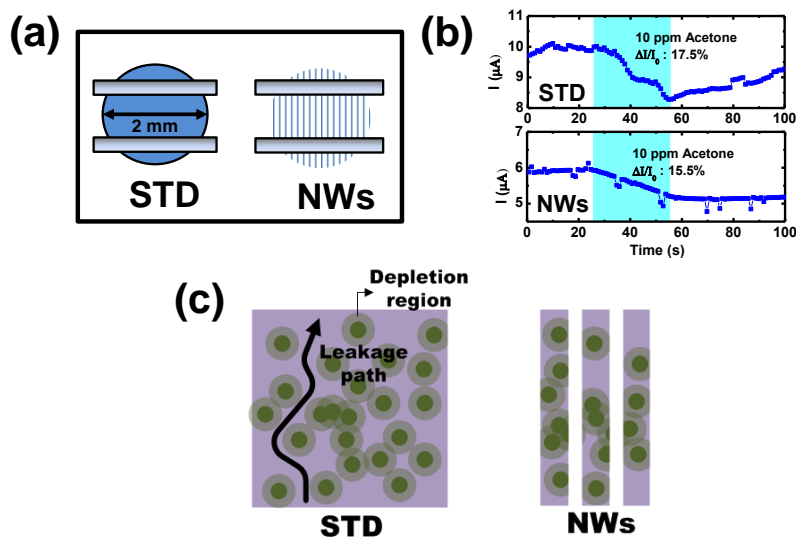


Figure 3.14 (a) Schematic showing two types of resistive gas sensors; STD device (DUV-patterned ZnO thin-film sensor) and NWs device (DUV-patterned ZnO nanowire sensor). (b) Sensing responses of STD device and NWs device to 10 ppm acetone. (c) Schematic showing acetone molecules absorbing on the surface of STD device and NWs device.

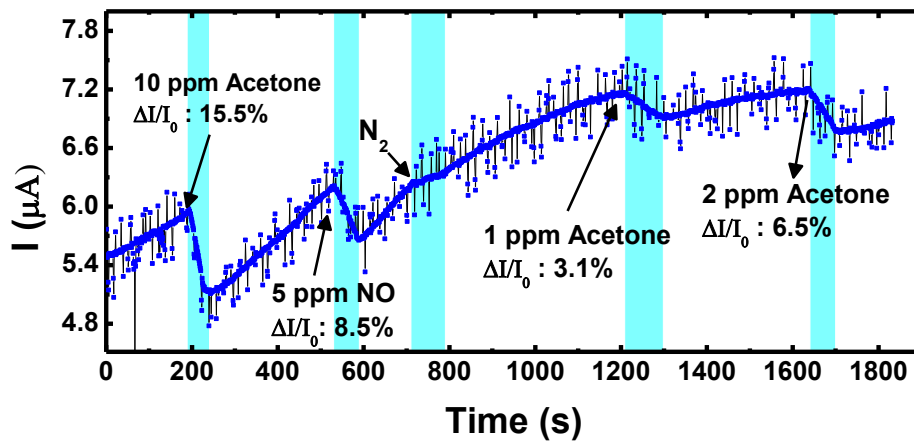


Figure 3.15. Sensing responses of NWs device to acetone, NO and N₂.

3.5. Enhancing conductivity of ZnO structures by doping group III elements

Group III elements such as In, Ga and Al are usually used to dope ZnO to achieve lower resistivity.^[21,22] For Al-doped ZnO, each effective substitution of Zn^{2+} by Al^{3+} generates a free electron, and therefore carrier concentration is increased. To demonstrate intrinsic property of DUV-patterned ZnO can be modulated by doping a small amount of elements, we doped Al into DUV-patterned ZnO structures. The atomic ratio of $\text{Al}/\text{Al}+\text{Zn}$ was 0.02. Figure 3.16a shows the AFM image of Al-doped ZnMAA lines patterned by DUV laser with a binary mask of $1.6\ \mu\text{m}$ period. The doping by Al did not degrade the capacity of ZnMAA precursor for DUV patterning. The DUV-patterned structures were firstly annealed at $600\ ^\circ\text{C}$ in air for one hour to remove organic compounds and then annealed at $600\ ^\circ\text{C}$ in Ar/H_2 (95/5) for 30 mins to activate Al dopants in ZnO lattice.^[23] In order to make electrical measurements, 100 nm-thick Al electrodes were thermally deposited through a shadow mask on Al-doped ZnO lines as shown in the inset of Figure 3.16b. The distance between two electrodes is $200\ \mu\text{m}$. Under a given voltage bias between $-3\ \text{V}$ and $+3\ \text{V}$, the current value of Al-doped ZnO lines was compared with ZnO lines without doping. As expected, the conductivity of ZnO was enhanced by 2% of Al doping from $\sim 1.5 \times 10^{-4}\ (\Omega\text{cm})^{-1}$ to $\sim 3.2 \times 10^{-3}\ (\Omega\text{cm})^{-1}$. (Figure 3.16b) These results imply that direct-patterned ZnO could have a wide range of applications for its modulatable material property. Using the same material platform and same lithography tool (DUV lithography), it is possible to incorporate conducting, semiconducting materials, which will be very useful for easy integration in complex devices.

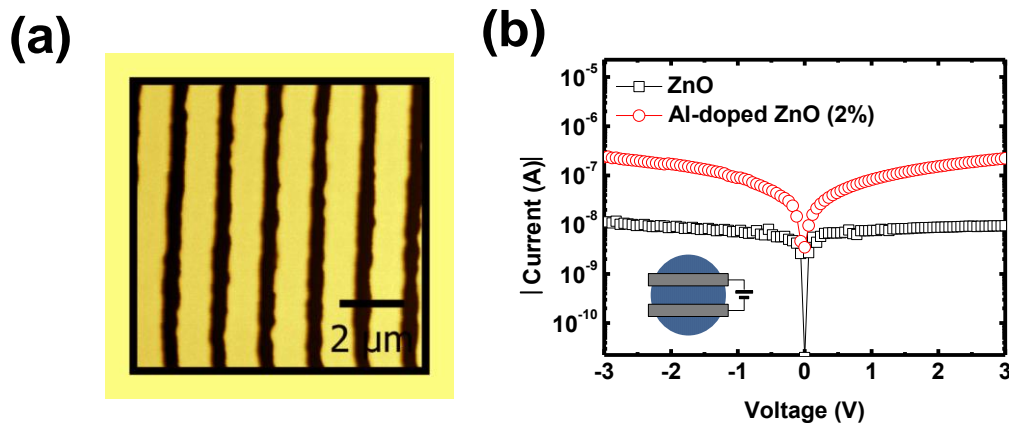


Figure 3.16. (a) DUV-patterned ZnMAA lines doped with aluminum acetylacetonate ($\text{Al}/\text{Al}+\text{Zn} = 0.02$). (b) I-V characteristics of DUV-patterned ZnO lines with and without doping.

3.6. Conclusion and perspective

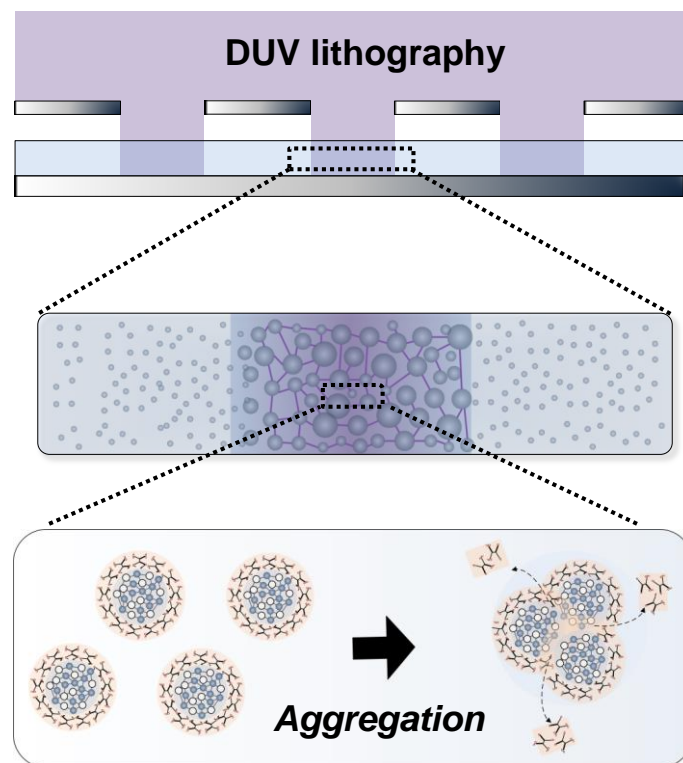
We have successfully demonstrated ZnO micro- and nanostructures via DUV direct patterning. In comparison to other lithography techniques such as e-beam lithography and EUV lithography, DUV lithography is important for more common use in semiconductor industry. Moreover, DUV direct patterning has the advantages of low cost, simple process, applicability to solutions of different composition, and excellent controllability in the size, shape and location. In this work, we have developed a ZnMAA-based precursor which shows excellent photosensitivity to DUV light and is able to produce high resolution patterns down to 300 nm. The photoreactions induced by DUV light in ZnMAA-based precursor have been investigated by in situ ellipsometry, *in situ* FTIR, XPS analysis and electrical measurements. The results indicate that DUV irradiation only gives rise to a small amount of M-O-M network and therefore high portion of direct-patterned ZnMAA structures is organic without electrical properties. After thermal annealing at temperature above 400 °C in air for one hour, organic part can be removed thoroughly, leading to the formation of ZnO with semiconducting properties. To show that the proposed technique can be used in device fabrication, we have demonstrated a direct-patterned ZnO nanowire FET with mobility of 0.45 cm²/Vs, threshold voltage of 3.4 V and subthreshold swing of 0.46 Vdec⁻¹. We also explored the gas sensing behavior of direct-patterned ZnO nanowires. Negative current response was observed during exposure to acetone and NO in a background of N₂. Finally, we enhanced the conductivity of direct-patterned ZnO by doping with 2% of Al. These results suggest the potential for producing nanoscale ZnO devices and systems by using ZnMAA-based precursors and DUV lithography.

3.7. Bibliography

- [1] F. Stehlin, F. Wieder, A. Spangenberg, J. M. Le Meins, O. Soppera, *J. Mater. Chem. C* 2014, 2, 277.
- [2] Edited by J. Lewis and R. G. Wilkins, *Modern coordination chemistry*, Interscience Publishers, New York 1960, 387
- [3] Y. H. Hwang, S. J. Seo, J. H. Jeon, B. S. Bae, *Electrochem. Solid-State Lett.* 2012, 15, H91.
- [4] H. Li, Y. Huang, Q. Zhang, Y. Qiao, Y. Gu, J. Liu, Y. Zhang, *Nanoscale* 2011, 3, 654.
- [5] Y. H. Kim, J. S. Heo, T. H. Kim, S. Park, M. H. Yoon, J. Kim, M. S. Oh, G. R. Yi, Y. Y. Noh, S. K. Park, *Nature* 2012, 489, 128.
- [6] S. Park, K.-H. Kim, J.-W. Jo, S. Sung, K.-T. Kim, W.-J. Lee, J. Kim, H. J. Kim, G.-R. Yi, Y.-H. Kim, M.-H. Yoon, S. K. Park, *Adv. Funct. Mater.* 2015, 25, 2807.
- [7] R. Coquand, M. Casse, S. Barraud, D. Cooper, V. Maffini-Alvaro, M.-P. Samson, S. Monfray, F. Boeuf, G. Ghibaudo, O. Faynot, T. Poiroux, *IEEE Trans. Electron Devices* 2013, 60, 727.
- [8] A. M. Burke, D. J. Carrad, J. G. Gluschke, K. Storm, S. Fahlvik Svensson, H. Linke, L. Samuelson, A. P. Micolich, *Nano Lett.* 2015, 15, 2836.
- [9] C. Zhang, W. Choi, P. K. Mohseni, X. Li, *IEEE Electron Device Lett.* 2015, 36, 663.
- [10] W. I. Park, G. C. Yi, M. Kim, S. J. Pennycook, *Adv. Mater.* 2002, 14, 1841.
- [11] P. Yang, H. Yan, S. Mao, R. Russo, J. Johnson, R. Saykally, N. Morris, J. Pham, R. He, H. Choi, *Adv. Funct. Mater.* 2002, 12, 323
- [12] T. J. Morrow, M. Li, J. Kim, T. S. Mayer, C. D. Keating, *Science* 2009, 323, 352.
- [13] C. Jiang, S. Liu, X. Chen, S. Yu, *CrystEngComm* 2014, 16, 8646.
- [14] A. Amma, B. Razavi, S. K. St Angelo, T. S. Mayer, T. E. Mallouk, *Adv. Funct. Mater.* 2003, 13, 365.
- [15] H.-C. Lin, F. Stehlin, O. Soppera, H.-W. Zan, C.-H. Li, F. Wieder, A. Ponche, D. Berling, B.-H. Yeh, K.-H. Wang, *Scientific reports* 2015, 5.
- [16] F. Patolsky, G. Zheng, O. Hayden, M. Lakadamyali, X. Zhuang, C. M. Lieber, *PNAS* 2004, 101, 14017.
- [17] Z. Jiang, Q. Qing, P. Xie, R. Gao, C. M. Lieber, *Nano Lett.* 2012, 12, 1711.
- [18] S. J. Chang, T. J. Hsueh, I. Chen, S. F. Hsieh, S. P. Chang, C. L. Hsu, Y. R. Lin, B. R. Huang, *IEEE Trans. Nanotechnol.* 2008, 7, 754.
- [19] Y. H. Hwang, S. J. Seo, B. S. Bae, *J. Mater. Res.* 2010, 25, 695.
- [20] A. Afzal, N. Cioffi, L. Sabbatini, L. Torsi, *Sens Actuators B Chem.* 2012, 171, 25.
- [21] P. Nunes, E. Fortunato, P. Tonello, F. B. Fernandes, P. Vilarinho, R. Martins, *Vacuum* 2002, 64, 281.
- [22] M. Gabás, A. Landa-Cánovas, J. L. Costa-Krämer, F. Agulló-Rueda, A. R. González-Elipe, P. Díaz-Carrasco, J. Hernández Moro, I. Lorite, P. Herrero, P. Castellero, A. Barranco, J. Ramón Ramos-Barrado, *J. Appl. Phys.* 2013, 113, 163709.
- [23] H. Damm, P. Adriaenssens, C. De Dobbelaere, B. Capon, K. Elen, J. Drijkoningen, B. Conings, J. V.

Manca, J. D'Haen, C. Detavernier, P. C. M. M. Magusin, J. Hadermann, A. Hardy, M. K. V. Bael,
Chem. Mater. 2014, 26, 5839.

Chapter IV: Chemical and structural investigation of Zn-oxo cluster photoresist



Résumé du Chapitre IV.....	100
4.1. Introduction.....	101
4.2. Formation of Zn-oxo clusters in precursor solution.....	102
4.3. DUV Exposure.....	103
4.4. Prebaking.....	106
4.5. Development	108
4.6. Thermal annealing.....	109
4.7. Conclusion and perspective	114

Résumé du Chapitre IV

Dans le Chapitre IV, nous avons effectué une étude détaillée de l'effet des paramètres physico-chimiques sur les microstructures. Le même précurseur que précédemment (ZnMAA) est utilisé. Dans un premier temps, on s'intéresse aux réactions en solutions et il est montré que ces réactions conduisent à la formation d'oxo-clusters de Zn (ZnOC) de taille nanométriques, stables, après un vieillissement de 2 mois, même pour une solution à haute concentration (> 1 M). Cet étude met en évidence un des intérêts de notre méthode qui permet de préparer des solutions stables de nanoclusters de ZnO photoréticulables.

Par la suite, une étude de la structure du matériau à chaque étape du procédé est menée. En particulier les phénomènes de cristallisation qui se produisent lors de l'étape de recuit thermique sont discutés. Ils conduisent à la formation d'une sur-structuration qui peut s'expliquer par une cristallisation non-homogène dans les microstructures.

Les spectres d'absorption obtenus à partir des mesures par ellipsométrie révèlent que l'irradiation DUV et le recuit thermique peuvent donner lieu à une réticulation-agrégation des ZnOC. Cependant, l'irradiation DUV n'induit que l'agrégation des ZnOC sans provoquer de cristallisation. En revanche, le recuit thermique peut non seulement provoquer l'agrégation, mais aussi la nucléation et la croissance des nanoparticules de ZnO. En outre, le réseau M-O-M induit par irradiation DUV est similaire à une structure ZnO amorphe obtenue lors d'un recuit thermique inférieur à 300 °C. Bien que l'impact soit faible, nous avons constaté que l'irradiation DUV affecte la structure cristalline de ZnO. Le rapport de la phase cristalline de l'orientation des axes c des échantillons à motif DUV est plus élevé que ceux qui ne sont pas soumis à une irradiation DUV.

Cette étude améliore la compréhension du photoresist à base de clusters d'oxyde métallique et de sa transformation de l'état hybride organique-inorganique à l'état inorganique. Les mécanismes proposés dans ce travail peuvent être étendus à d'autres types de resists d'oxyde métallique à base de clusters ou de nanoparticules. À l'avenir, nous projetons d'étudier l'effet des paramètres d'exposition tels que la longueur d'onde d'exposition, la réflectance du substrat, l'écart entre le masque et le film, et l'angle d'exposition sur la taille et la forme des structures.

4.1. Introduction

It has been shown that the photo-induced crosslinking of metal oxide resists relies on ligand exchange and aggregation of clusters or colloidal particles that leads to the solidification into metal oxide inorganic network in photo-irradiated regions.^[3,4] Non-irradiated regions remain soluble and can thus be easily removed by developers just like negative tone resist. However, the underlying mechanisms causing variation on the size and shape of photo-patterned metal oxide structures have not been well understood. Moreover, an additional thermal annealing is usually required to transform the inorganic-organic hybrid material into pure inorganic material for semiconductor or conductor applications. The annealing condition plays an important role in deciding final crystallization results which will govern the structural shape as well as the physical properties of metal oxide nano- or micro-patterns.

In this Chapter, we carried out a detailed investigation of the effect of physical-chemical parameters on structures after photopatterning and focused on the impact of aggregation and crystallization of photosensitive metal-oxide clusters (MOCs). As a model system, DUV patternable ZnOC photoresist was used. In previous works, metal oxide nanocomposites were synthesized and then dispersed into a solution or photoresist.^[1-3] In this study, ZnOCs were formed directly in our photoresist via hydrolysis-condensation reactions between ZnMAA and acid-water, which is a simpler method for preparing photoresist containing metal oxide nanocomposites. The well-controlled synthesis conditions lead to the formation of very stable ZnO clusters, without precipitation after 2-month aging, even for high-concentration solution (> 1 M). In comparison to other works, we believe our method is simpler and quicker for preparing organic-inorganic hybrid nanocomposite photoresist.

The standard procedure used in this study to fabricate ZnO lines is displayed in Figure 4.1. ZnOC resist was prepared from ZnMAA and spin-coated (2000 rpm, 60 s) on the Si substrate. To remove excess solvent, the sample is heated on a hot plate at moderate temperature (50 °C for 5 minutes). Then, the dried film is exposed to DUV light (193 nm, 450 mJ cm⁻²) through a binary mask (600 lines mm⁻¹). The photo-induced solidification occurs in the exposed regions. After putting the sample in the developer (1-propanol) for 30 s, the non-irradiated regions can be removed. To remove organic part inside the structures, post annealing is performed as a final step. In the following experiments, we investigated the influence of each process step on

patterns made by ZnOC photoresist as well as underlying mechanisms. Only experimental parameter in the targeting process step was changed. Other parameters were kept the same as shown in the standard procedure.

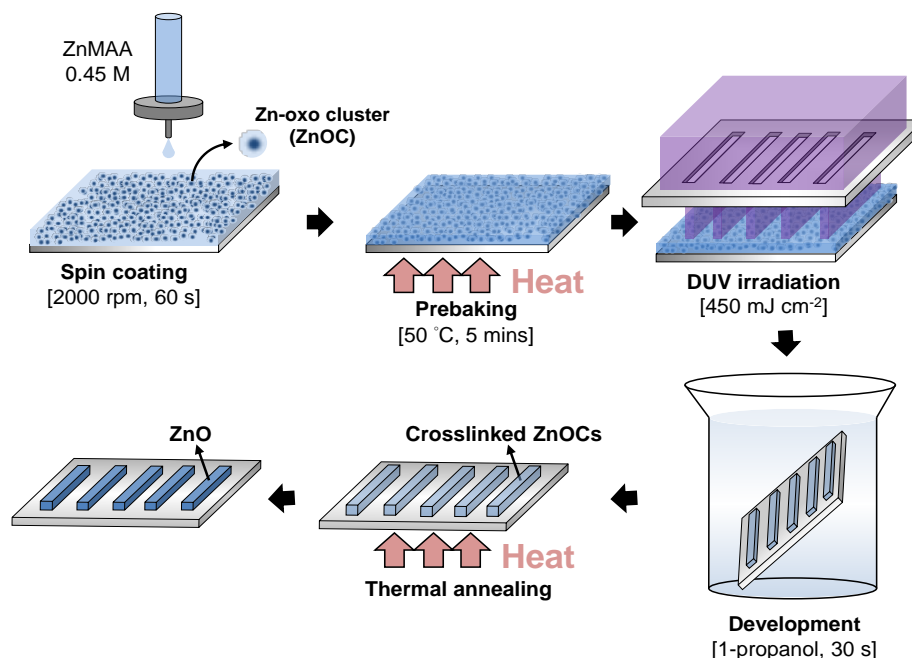


Figure 4.1. Schematic illustration of standard fabrication procedure used in this study for making periodic ZnO lines.

4.2. Formation of Zn-oxo clusters in precursor solution

Due to water molecules added into the ZnMAA precursor, ZnOCs are formed via hydrolysis-condensation reactions as shown in Figure 4.2a. FTIR spectrum of an as-spun ZnOC resist is shown in Figure 4.2b. Two distinct peaks at 1410 cm^{-1} and 1570 cm^{-1} can be attributed respectively to symmetric and asymmetric stretch bands of MAA ligands on the surface of ZnOCs and peak at 430 cm^{-1} can be attributed to vibration of ZnO framework inside the clusters.^[4,5] Figure 4.3a and 4.3b show high-resolution transmission electron microscopy (HRTEM) image of ZnOCs formed in a 0.45 M ZnMAA solution. The cluster size was found to be around 2.5 nm and the distance between ZnO crystal planes is $\sim 0.26\text{ nm}$, which matches that of the (002) planes of the wurtzite structural ZnO.

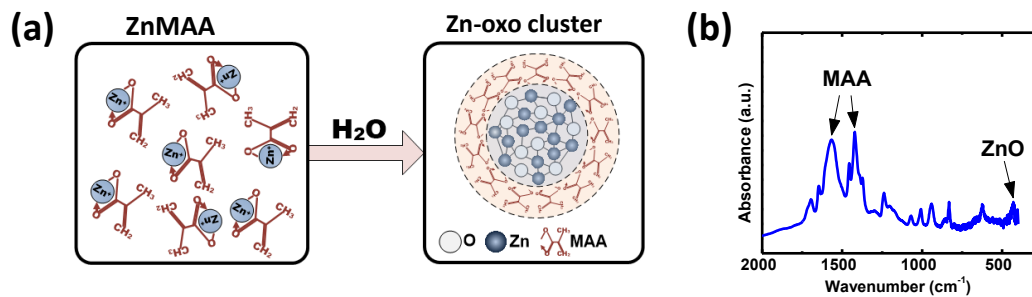


Figure 4.2. (a) Formation of ZnOCs via hydrolysis-condensation reaction. (b) FTIR spectrum of an as-spun ZnOC resist film.

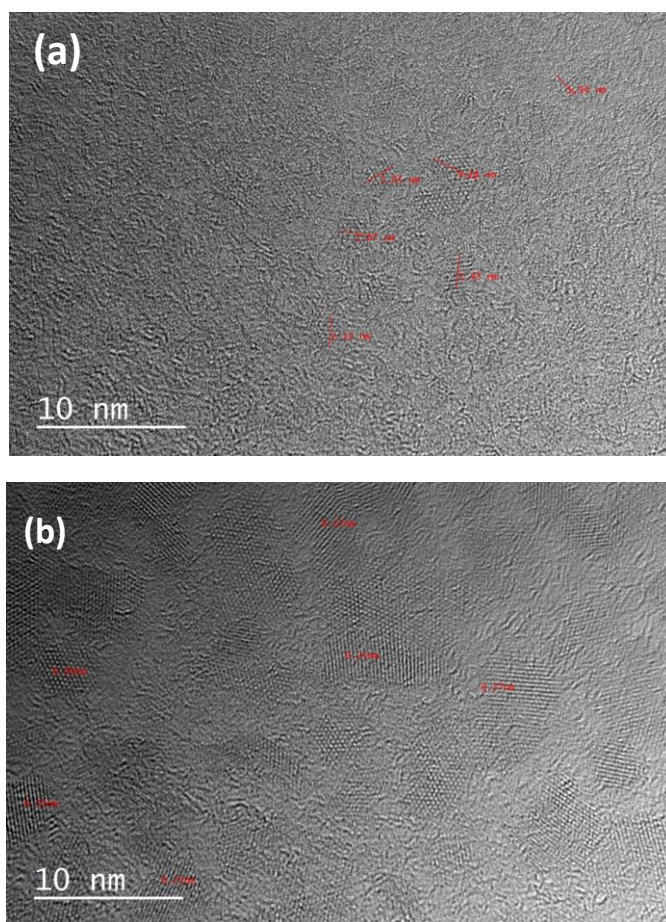


Figure 4.3 (a) HRTEM image showing the size of ZnOCs formed in our photoresist. (b) RTEM image showing distances between the crystal planes in ZnOCs.

4.3. DUV Exposure

Under DUV irradiation, MAA ligands on the surface of ZnOCs are replaced by -OH ligands,

leading to crosslinking-aggregation of ZnOCs as shown in Figure 4.4a.^[6] DUV-induced ligand exchange phenomenon can be observed by the variation of absorption spectrum as shown in Figure 4.4b. The absorption intensity at 193 nm decreased with the increase DUV irradiation, indicating the decomposition of MAA ligands.

The top view AFM images and cross-sectional profiles of DUV-patterned lines made by different energies are shown in Fig. 4.5(a)-(d) respectively. As shown in Figure 4.5a, irregular topography is observed in the pattern irradiated by 150 mJ cm^{-2} , which can be attributed to insufficient crosslinking in exposed regions. During the development step, those low-crosslinked regions were partially dissolved. The line-width of DUV-patterned lines increased gradually with the increase of exposure dose. (Figure 4.6a) The occurrence of lateral expansion can be attributed to reflected light from the surface of silicon substrate and diffracted light produced by the edges of binary mask and the gap between binary mask and substrate. (Figure 4.6b) Spacers of $150 \mu\text{m}$ were placed on the gel films to avoid possible contamination to the photo-mask. The setup can thus be regarded as proximity lithography with negative tone oxide resist.^[7] If we “overexpose” ZnOC resist films with high energy doses, strong reflected and diffracted light can lead to excess crosslinking; thus, line-width increased significantly. These results show that the patterning property of metal oxide photoresist is almost the same as conventional organic negative tone resist. However, many studies indicates that ZnOCs in solution can aggregate and grow into larger colloid particles spontaneously, which sometimes even causes precipitation in solution.^[8] Although no precipitation was found in our solutions even after two months aging, indicating a very slow rate of cluster aggregation, it’s unclear if the spontaneous cluster aggregation affects size and shape of patterns. In particular spin-coating provokes solvent evaporation and ZnOCs get very close to each other; thus, rapid cluster aggregation or agglomeration may occur. To investigate whether ZnOCs in non-exposed regions are stable without affecting the size of DUV-pattern structures, we aged samples with different time intervals before development as shown in Figure 4.7a. The cross-sectional profiles of DUV-patterned lines after development are shown in Figure 4.7b. Even after aging in atmosphere for two hours, no significant difference was observed, showing ZnOCs in our photoresist possess good stability for photopatterning.

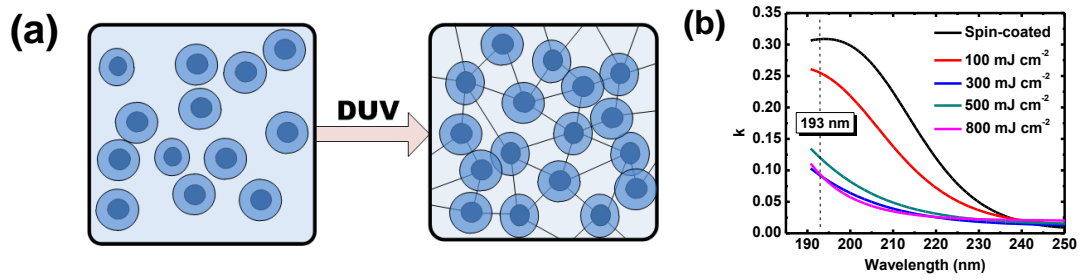


Figure 4.4. (a) DUV-induced crosslinking-aggregation of ZnOCs. (b) Absorption spectra of ZnOC resist films patterned with different DUV energies.

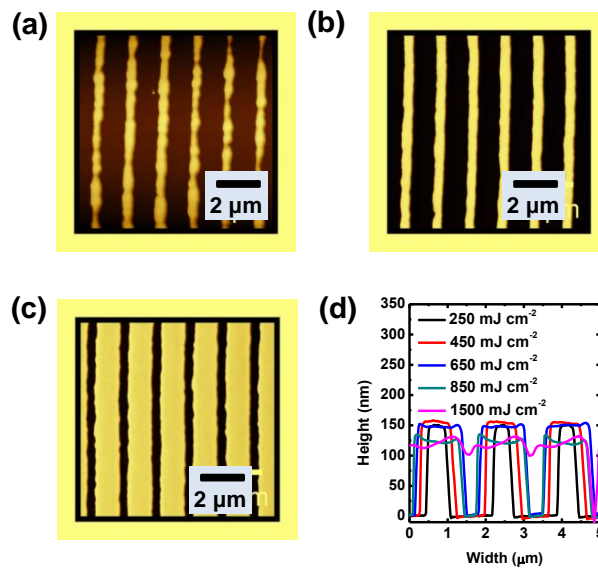


Figure 4.5. (a) Top-view AFM images of DUV-patterned period lines fabricated with different DUV exposure energies of 150 mJ cm^{-2} (b) 250 mJ cm^{-2} , and (c) 850 mJ cm^{-2} . (d) Cross-sectional profiles of DUV-patterned periodic lines fabricated with different DUV exposure energies.

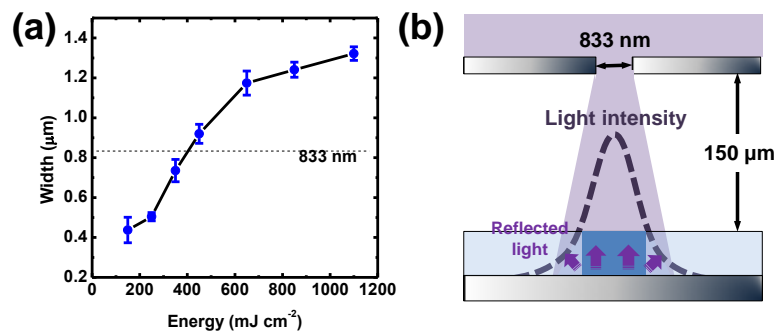


Figure 4.6. (a) Line-width versus DUV energy. (b) Schematic illustration of diffracted and reflected light during DUV exposure.

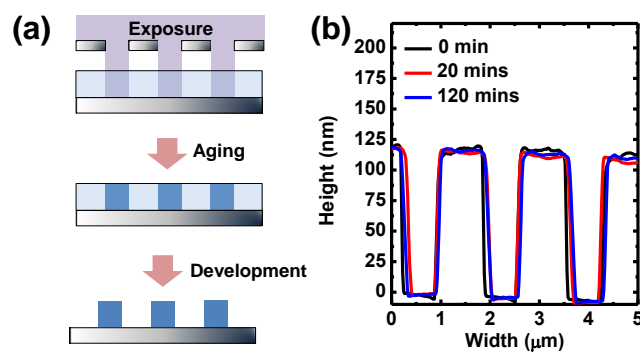


Figure 4.7. (a) Schematic showing DUV-exposed ZnOC resist films aged in air with different time intervals before development. (b) Cross-sectional profiles of DUV-patterned periodic lines aged in air with different time intervals.

4.4. Prebaking

Figure 4.8a-d shows topographies and cross-sectional profiles of DUV-patterned lines obtained from different prebaking conditions (50 °C, 70 °C and 90 °C for 5 minutes). Without prebaking, no patterns can be obtained after development due to a lot of solvent inside the as-spun film, hindering crosslinking reactions during DUV irradiation. With a moderate prebaking, excess solvent can be removed; thus, aggregation of ZnOCs can happen more easily under DUV irradiation. Fine patterns can be obtained by prebaking at 50 °C and 70 °C; however, after prebaking at 90 °C, line-width increased rapidly, implying the 90 °C baking gave rise to crosslinking-aggregation reactions. L. Li *et al.* has reported the observation of DUV-assisted as well as thermal-assisted aggregation of MAA-functionalized hafnium oxide nanoparticles.^[4] The authors summarized that thermal heating has similar effect as DUV irradiation. Both of them can cause particle aggregation. We suppose large lateral expansion after prebaking at 90 °C is due to thermal-assisted cluster aggregation. Figure 4.9a shows the thickness and refractive index (n) as a function of prebaking temperature. Owing to removal of excess solvent, the thickness decreases with the increase of prebaking temperature and the n value increases with the increase of prebaking temperature. When the temperature was higher than the boiling point of ethanol (78 °C), the n value increased rapidly, indicating the intrinsic property of the thin film was changed. The changes caused by prebaking can be interpreted better by monitoring the absorption spectra as shown in Figure 4.9b. Before prebaking, we observed an absorption band peaked at ~ 210 nm which is resulted from charge transfer to solvent band of $\text{OH}^-_{(\text{aq})}$.^[9] After prebaking at 70 °C, excess solvent was removed, which increased the concentration of ZnOCs as well as MAA ligands in the resist film; thus the absorption coefficient (k) at 193 nm increases from 0.18 to 0.42. As the prebaking

temperature was further increased to 90 °C, a slight red shift was observed in the absorption spectrum, implying ZnOCs started to nucleate.^[9] In contrast, no red shift was observed for DUV-assisted aggregation (Figure 4.3b), implying DUV patterning only induces crosslinking-aggregation of ZnOCs without initiating nucleation and the growth of ZnO crystals. In addition, we found the k value at 193 nm decreased when prebaking temperature is higher than 90 °C. As mentioned before, we attribute absorption band peaked at 193 nm to MAA ligands on the surface of ZnOCs and the decrease of the absorption intensity at 193 nm after prebaking at 90 °C can be attributed to the replacement of MAA ligands by M-O-M networks between ZnOCs due to thermal-assisted aggregation. The k value at 193 nm decreased further after prebaking at 110 °C, and the film cannot be removed by the developer, indicating rigid M-O-M network was constructed between ZnOCs as well as between the film and substrate. These results indicate that by using prebaking with temperature at the range of 50-70 °C we can remove excess solvent and enhance absorption of ZnOC resist to DUV light; however, too much heating should be avoided, because it may lead to residue layer on the substrate.

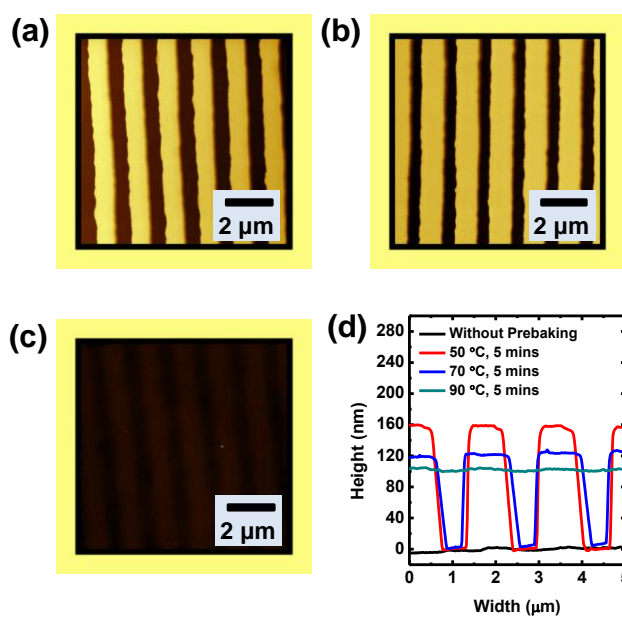


Figure 4.8. Top-view AFM images of DUV-patterned period lines fabricated with different prebaking temperatures of (a) 50 °C, (b) 70 °C, and (c) 90 °C before DUV patterning. (d) Cross-sectional profiles of DUV-patterned periodic lines fabricated with different prebaking temperatures.

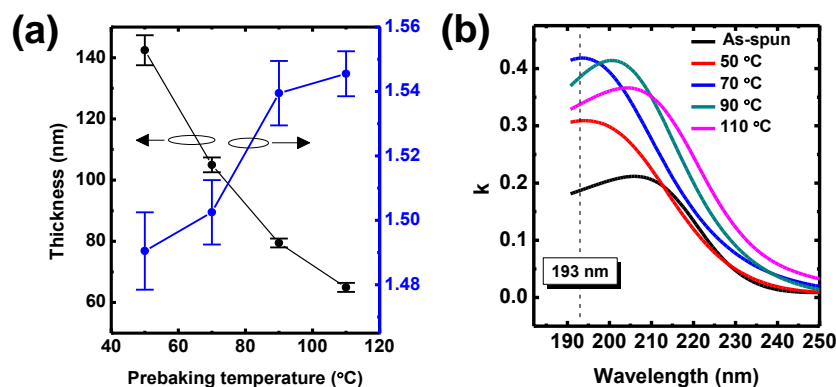


Figure 4.9. (a) Variation of thickness and refractive index (n) at 633 nm with different prebaking temperatures. (b) Absorption spectra of ZnOC resist films prebaked at different temperatures.

4.5. Development

After DUV exposures, M-O-M network is formed in exposed regions connecting ZnOCs in the solidified patterns. A good developer can dissolve non-exposed regions but do not damage the crosslinked patterns for negative tone resists. In previous studies, polar solvents such as ethanol, 2-methoxyethanol and cyclohexanone were used as developer for photo-patterned metal oxide structures.^[6,10,11] Generally, the dielectric constant (ϵ) of solvent is proportional to its ability to dissolve ionic compounds^[12]; thus, developing in solvents of different dielectric constants may lead to different results. For instance, some difference of DUV-patterned structures was found between samples developed in ethanol ($\epsilon = 25.00$) and those developed in 1-propanol ($\epsilon = 20.81$) as shown in Figure 4.10a and 4.10b. As ethanol was used as developer, some damage at the edges was observed in the topography, suggesting that part of ionic bonds were broken by ethanol molecules with strong polarity. In contrast, when 1-propanol was used as developer, no damage was observed. Thus, 1-propanol was chosen as developer in this work. Figure 4.10c shows cross-sectional profiles of patterns developed in 1-propanol for different developing times from 5 s to 300 s. Besides some height variation due to run-to-run variation in spin-coating process, line-widths are almost the same for developing times more than 15 s, indicating development is a very stable process for metal oxide resist.

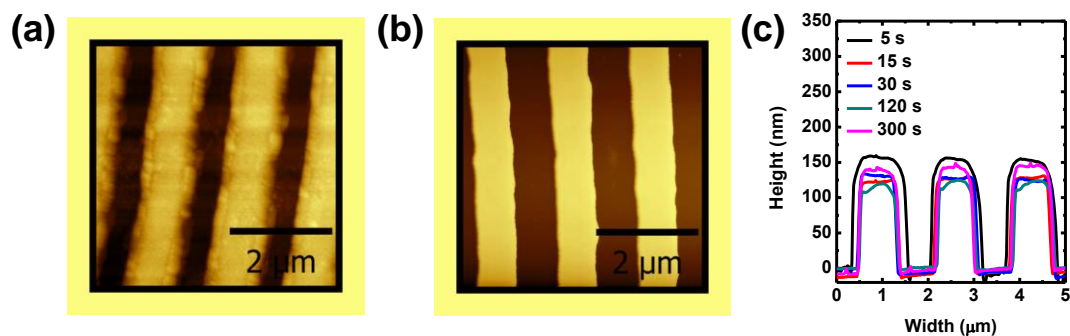


Figure 4.10. Top-view AFM images of DUV-patterned period lines developed in (a) ethanol and (b) 1-propanol. (c) Cross-sectional profiles of DUV-patterned periodic lines developed in 1-propanol with different time intervals.

4.6. Thermal annealing

Thermal annealing plays an important role in eliminating embedded organic compounds and crystallizing metal oxide resist. To investigate the effect of thermal annealing on embedded organic compounds, FTIR analysis was performed. Two types of samples were prepared for comparison: spin-coated ZnOC resist film without DUV patterning and ZnOC resist film patterned by DUV lithography. Evolution of the FTIR spectra of spin-coated and DUV-patterned ZnOC resist films as a function of annealing temperature are shown in Figure 4.11a and 4.11b respectively. In the spectra, we observed a broad absorption band ranging from 3200 cm^{-1} to 3700 cm^{-1} corresponding to hydroxyl groups and a small absorption band peaked at 2960 cm^{-1} corresponding to C-H bonding.^[13] As mentioned before, the two absorption bands peaked at 1410 cm^{-1} and 1570 cm^{-1} are attributed to MAA ligands on the surface of ZnOCs.^[4] The intensity of these absorption bands decreased with the increase of annealing temperature for the two types of samples, implying the occurrence of thermal-induced crosslinking and decomposition of embedded organic ligands. After annealing at temperature above $400\text{ }^{\circ}\text{C}$, all absorption bands disappeared, indicating embedded organic compounds were removed completely.

To investigate thermal-induced crystallization in ZnOC resist films, ellipsometry analysis was performed. Figure 4.12a and 4.12b show, respectively, absorption spectra of spin-coated and DUV-patterned ZnOC resist films annealed at different temperatures. It has been known that aggregation and the growth of ZnO crystals can increase density of electronic states and decrease absorption band gap; thus, absorption spectrum can be used to monitor the size of ZnO crystals embedded in ZnOC resist.^[14] For the spin-coated resist film, the absorption band extended to $\sim 350\text{ nm}$ after annealing at $200\text{ }^{\circ}\text{C}$, indicating bigger ZnO crystals were formed after the thermal treatment. In contrast, no red shift was observed for DUV-patterned resist film after $200\text{ }^{\circ}\text{C}$ thermal annealing, indicating the size of ZnO crystals was almost unchanged after the thermal treatment. (Figure 4.12b) According to previous reports, amorphous ZnO structure is stable up to $200\text{ }^{\circ}\text{C}$ without

recrystallization.^[15] We suppose the M-O-M network generated by DUV irradiation is similar to an amorphous structure with organic compounds trapped inside the oxide framework; thus, a 200 °C thermal annealing is insufficient to cause crystallization. As annealing temperature was increased to 300 °C, no significant change was found for spin-coated resist film. On the other hand, we observed a low-intensity absorption band extending to 400 nm for DUV-patterned resist film, which can be attributed to small amount of ZnO crystals formed inside the resist film. As annealing temperature was increased to 400 °C, clear absorption bands extending to 400 nm was observed for both types of films, indicating they were transformed into crystalline ZnO films. Figure 4.13a and 4.13b show, respectively, refractive-index spectra of spin-coated and DUV-patterned ZnOC resist films annealed at different temperatures. We found that thermal annealing can effectively increase the refractive index (n) of ZnOC resist. The n values at 633 nm were increased to ~1.63 for both types of films after annealing at 300 °C in air for one hour. However, as annealing temperature was increased to 400 °C, n values at 633 nm decreased to ~1.52 and ~1.47 for spin-coated and DUV-patterned films respectively. The variation of refractive index can be explained as follows. After annealing at 300 °C, unreacted or weakly bonded organic species can be removed and M-O-M network was increased due to thermal-induced crosslinking, which increase the density as well as the refractive index of the film.^[16] After annealing at temperatures above 400 °C, organic compounds were completely removed and a large peak located at 373 nm in the refractive-index spectra is due to extinction-like transition in crystalline ZnO.^[17] Generally, refractive index of a dense ZnO film is ~2 in visible light range. The low refractive index ~1.5 obtained from thermally-crystallized ZnOC resist implies a porous ZnO structure was formed.^[18] For obtaining high refractive-index metal oxide structures, titanium oxide based resist maybe a better option, because it has a refractive index ~0.6 higher than ZnO.^[16] It's noteworthy that in our previous work we have demonstrated by using DUV sensitive MAA modified titanium isopropoxide precursor high refractive index (n ~2 at 633 nm) TiO₂ patterns can be obtained.^[6]

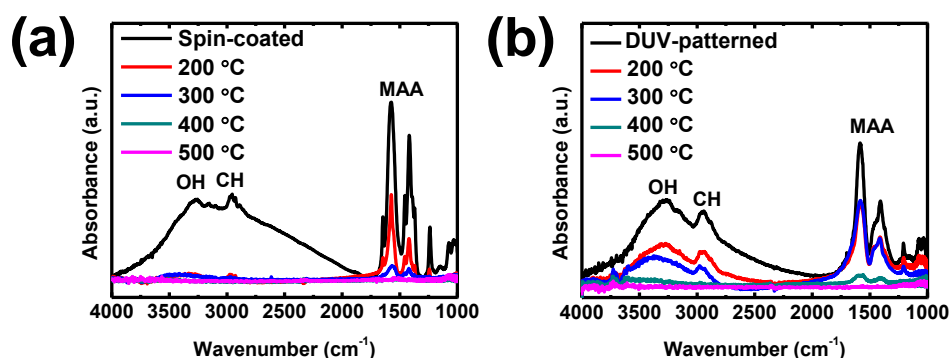


Figure 4.11. (a) FTIR spectra of spin-coated ZnOC resist films annealed at different temperatures. (b) FTIR spectra of DUV-patterned ZnOC resist films annealed at different temperatures.

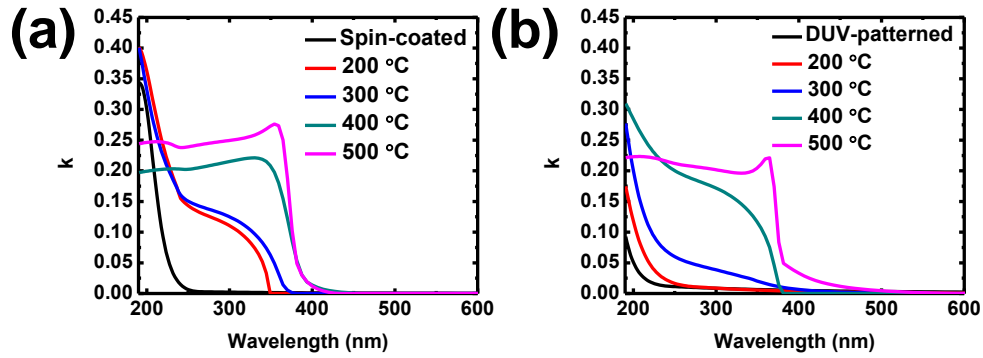


Figure 4.12. (a) Absorption spectra of spin-coated ZnOC resist films annealed at different temperatures. (b) Absorption spectra of DUV-patterned ZnOC resist films annealed at different temperatures.

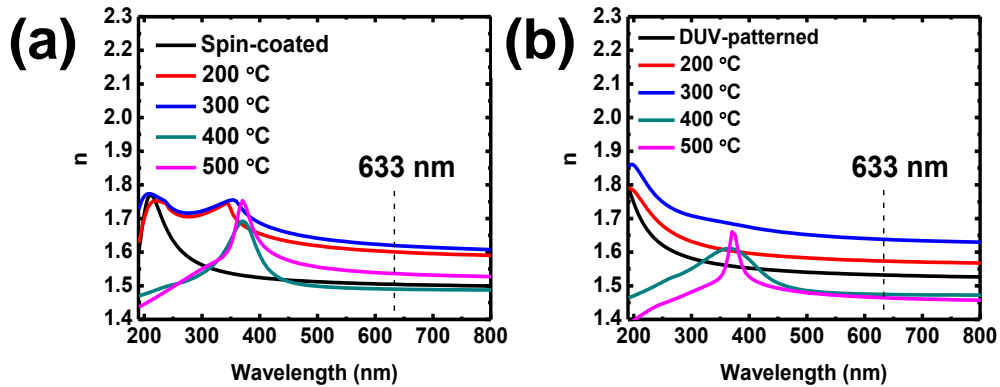


Figure 4.13 (a) Refractive-index spectra of spin-coated ZnOC resist films annealed at different temperatures. (b) Refractive-index spectra of DUV-patterned ZnOC resist films annealed at different temperatures.

The crystalline structures of ZnO films derived from ZnOC resist films were investigated by X-ray diffraction (XRD) analysis. Figure 4.14a and Figure 4.14b show, respectively, XRD patterns of spin-coated and DUV-patterned ZnOC resist films with annealing at different temperatures in air for one hour. No diffraction peak can be observed as annealing temperature is lower than 300 °C for both types of resist films, indicating they were not fully crystallized. After annealing at 500 °C, both types of resist films were transformed into polycrystalline ZnO films with Wurtzite 2H crystal structure type.^[19] We found that DUV-patterned samples have higher portion of c-axis or (002) orientation indicated by the peak at 34.4°. The enhancement of c-axis orientation might be due to the occurrence of structural relaxation caused by DUV irradiation before crystallization.^[20] Figure 4.14c shows XRD patterns of ZnOC resist films patterned by different DUV exposure energies and then annealed at 500 °C in air for one hour. No significant difference was found in the XRD patterns, implying DUV-induced crosslinking only has a small impact on nucleation and growth of ZnO crystals. Because ZnO is a semiconducting material, the effect of organic decomposition can also be monitored by electrical

properties. I_D - V_G curves of DUV-patterned ZnO TFTs annealed at different temperatures are shown in Figure 4.14d. No electrical property can be characterized for device annealed at 300 °C, implying the annealing temperature is insufficient to completely decompose embedded organic compounds which degrade carrier transport property. As annealing temperature was increased to 400 °C, we observed n-type transistor behaviour with on-off ratio 1.82×10^4 and field effect-mobility of $0.0075 \text{ cm}^2\text{V}^{-1}\text{s}^{-1}$. As annealing temperature was further increased to 500 °C, field-effect mobility increased to $0.034 \text{ cm}^2\text{V}^{-1}\text{s}^{-1}$. The enhancement of field-effect mobility can be attributed to the increase of ZnO grain size. Since ZnO grain size increases with the increase of annealing temperature, grain-boundary scattering effects on carrier transport were reduced.^[20]

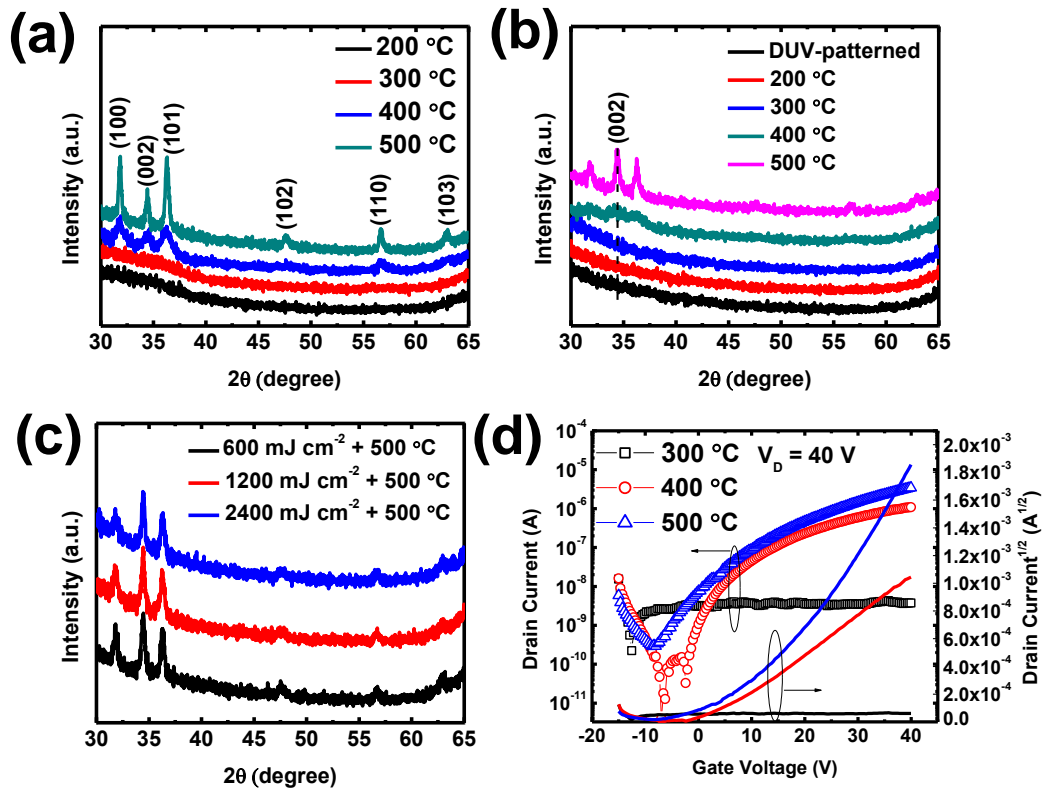


Figure 4.14. (a) XRD patterns of spin-coated ZnOC resist films annealed at different temperatures. (b) XRD patterns of DUV-patterned ZnOC resist films annealed at different temperatures. (c) XRD patterns of thermally crystallized ZnOC resist films which had been patterned by different DUV energies. (d) I_D - V_G curves of DUV-patterned ZnO TFTs.

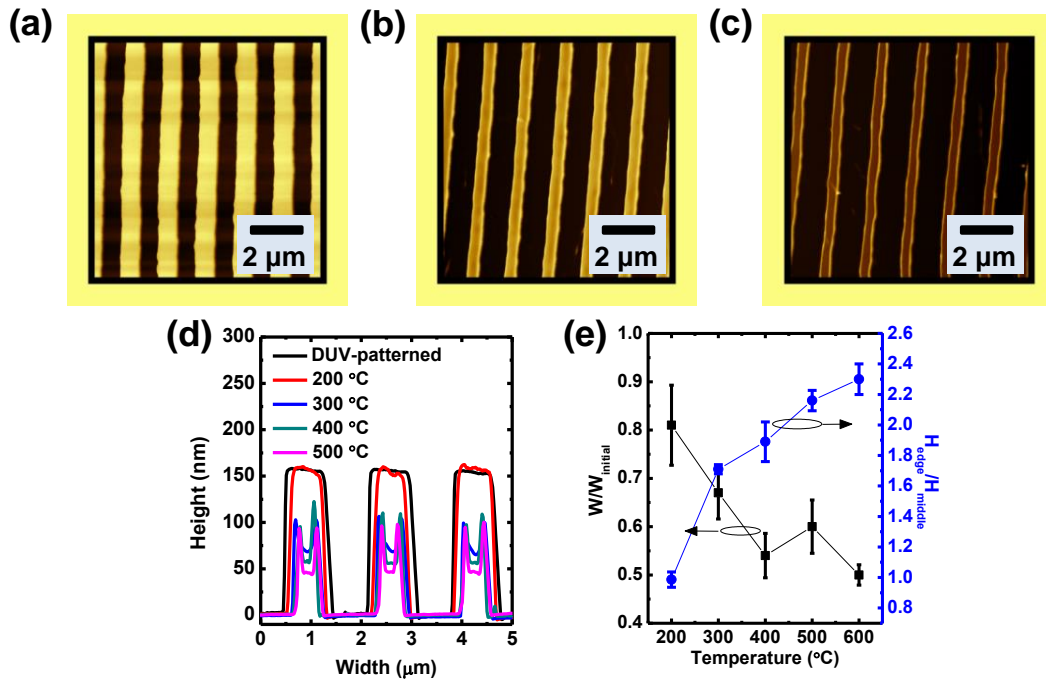


Figure 4.15. Top-view AFM images of DUV-patterned period lines (a) before post annealing, (b) annealed at 300 °C and (c) annealed at 500 °C. (d) Cross-sectional profiles of DUV-patterned period lines annealed at different temperatures. (e) Showing the variation of the ratio of [line-width after thermal annealing/line-width before thermal annealing] and the ratio of [height at edge/height at the middle part of DUV-patterned lines] as a function of annealing temperature.

To investigate how thermal annealing affects the size and shape of DUV-patterned metal oxide resist, periodic lines patterned by DUV lithography with the use of ZnOC resist were made and then annealed at different temperatures in air for one hour. The topographies and cross-sectional profiles are shown in Figure 4.15a-d. After annealing at 200 °C, no significant change was observed. However, as annealing temperature was increased to 300 °C, a double-peak profile appeared on the edge of the lines. In addition, the line-width largely shrank to around ~ 0.65 times of its initial value. It is observed that lateral shrinkage and the height of the peaks increase with the increase of annealing temperature. As annealing temperature was increased to 600 °C, the width of the lines shrink to ~ 0.5 times of its initial value and the edge part is ~ 2.3 times higher than the middle part. (Figure 4.15e) Similar double-peak profile has also been observed in micromolding patterned $\text{Pb}(\text{Zr}_{0.52}\text{Ti}_{0.48})\text{O}_3$ lines by Christopher R. Martin *et al.*^[21] The authors suggested that the occurrence of double-peak structures is due to rapid evaporation of organic compounds at the edge corners that with higher surface-to-volume ratio. Mathematical calculation and simulation were made to support the postulation. However, the shrinkage phenomenon was not considered in the bottom part of the line. In our case, we found after thermal treatment, ZnO lines had lateral shrinkage that shows no change in sidewall slope. If the double-peak profile is only caused by the high surface-to-volume ratio of upper corners, the sidewall slope should

always become less vertical regardless of the adhesion force between patterns and substrates after thermal annealing, because the upper part of the lines always shrinks more than the bottom part of the lines. Therefore, the double-peak profile might be explained better by an alternative explanation as follows. As shown in Figure 4.16, at the beginning of annealing, organic compounds close to the surface are decomposed faster into gaseous substances such as CO_2 and H_2O than those deep inside the structure, leading to the formation of a crystalline ZnO shells on the outer surface of the lines. During prolonged annealing, organic compounds deep inside the oxide layers are then gradually decomposed and removed from the patterns. During the crystallization of inner part of the structure, ZnO shells on the surface experience a contractive force that exerts on each face of the lines. Because the edge parts are supported by the sidewalls of ZnO shells, the vertical shrinkage is less severe, giving rise to the formation of double-peak profile. Interestingly, we only observe parallel shift of sidewalls toward each other, which can be explained by weak adhesion force between ZnO lines and the Si substrate. In addition, DUV-patterned ZnOC resist lines decrease their volumes to $\sim 18\%$ after turned into crystalline ZnO lines, implying a large part of DUV-patterned ZnOC resist is composed of organic species.

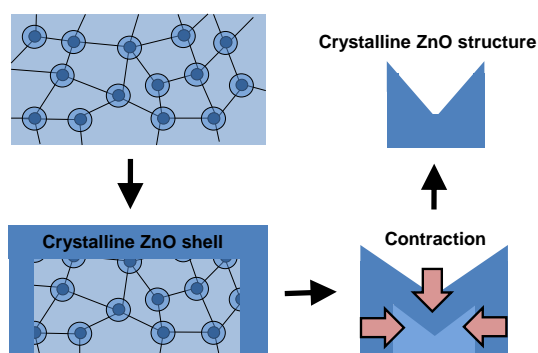


Figure 4.16. Schematic showing proposed mechanism for the formation of double-peak profile.

4.7. Conclusion and perspective

Zn-oxo clusters (ZnOCs) were successfully used as building blocks for DUV-patterned ZnO microstructures. In this study, we carried out a detailed investigation to the effect of crosslinking-aggregation of ZnOCs as well as crystallization on the size and shape of DUV-patterned periodic lines. The results are summarized in Table 4.1. Mechanisms accounting for line profile distortion like enlargement or double peak structure was investigated. In particular, the formation of double-peak profile can be explained by inhomogeneous crystallization that the crystallization process starts from the surface to the inner parts of the patterns.

Absorption spectra obtained from ellipsometry spectroscopy reveal that both DUV patterning and thermal annealing can give rise to crosslinking-aggregation of ZnOCs. However, DUV patterning only induces aggregation of ZnOCs without causing crystallization. On the other hand, thermal annealing

can not only cause aggregation but also cause nucleation and growth of ZnOCs. In addition, M-O-M network in DUV-patterned ZnOC resist film is similar to amorphous structure which suppresses crystallization during thermal annealing below 300 °C. Although the impact is small, we found that DUV patterning affects the crystalline structure of ZnO. The ratio of c-axis orientation crystalline phase of DUV-patterned samples is higher than those without DUV patterning.

This study improves the understanding to metal oxide photoresist based on metal oxide clusters and its transformation from organic-inorganic hybrid state to inorganic state. One may extend the mechanisms purposed in this work to various kinds of metal oxide resists based on metal-oxo clusters or nanoparticles to fabricate fine patterns with desirable physical properties. In the future, we will continue to investigate the effect of exposure parameters such as exposure wavelength, substrate reflectance, gap between the mask and resist film, and exposure angle on the size and shape of metal oxide cluster photoresist.

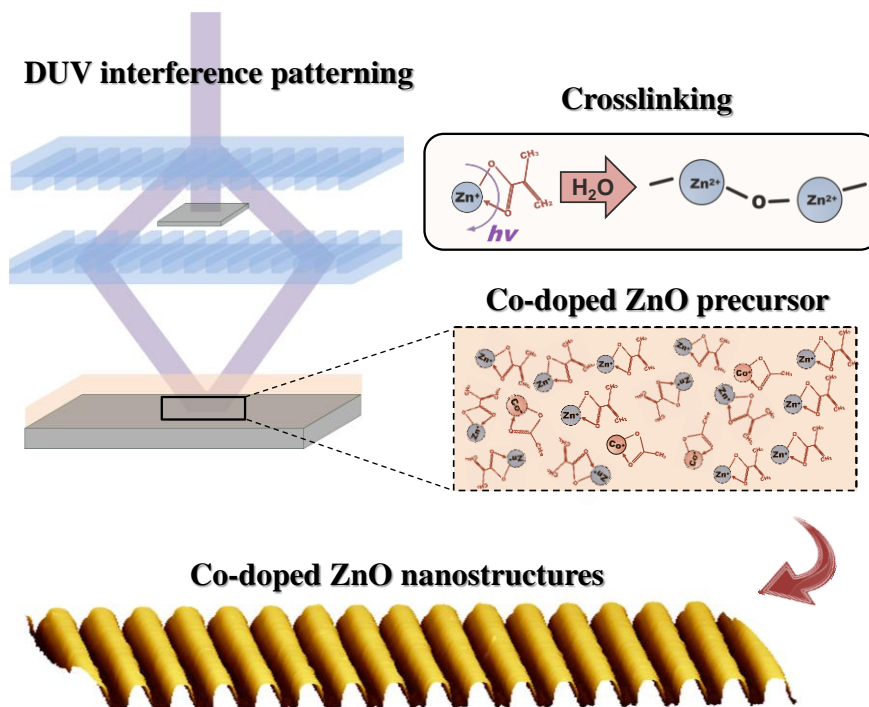
Table 4.1. General overview of line-width and surface roughness variation of DUV-patterned ZnO lines caused by each process step.

Process	Influence on line-width	Influence on surface roughness	Comments
Prebaking	↑	x	-Enhance absorption in DUV light range. -High prebaking temperature gives rise to thermal-assisted aggregation.
DUV irradiation	↑	x	-Exposure time ↑ line-width ↑ due to diffracted light.
Development	x	x	-Developers with high dielectric constant may damage patterns.
Thermal annealing	↓	↑	-A double-peak profile appears on the topography.

4.8. Bibliography

- [1] W. J. Bae, M. Trikeriotis, J. Sha, E. L. Schwartz, R. Rodriguez, P. Zimmerman, E. P. Giannelisa and C. K. Ober, *J. Mater. Chem.*, 2010, 20, 5186.
- [2] P. G. Reddy, N. Mamidi, P. Kumar, S. K. Sharma, S. Ghosh, K. E. Gonsalves and C. P. Pradeep, *RSC Advances*, 2016, 6, 67143.
- [3] L. Li, S. Chakrabarty, J. Jiang, B. Zhang, C. Ober and E. P. Giannelis, *Nanoscale*, 2016, 8, 1338.
- [4] L. Li, S. Chakrabarty, K. Spyrou, C. K. Ober, and E. P. Giannelis, *Chem. Mater.*, 2015, 27, 5027.
- [5] S. Verma and S. L. Jain, *Inorg. Chem. Front.*, 2014, 1, 534
- [6] F. Stehlin, F. Wieder, A. Spangenberg, J. M. Le Meins and O. Soppera, *J. Mater. Chem. C*, 2014, 2, 277.
- [7] X. Tian, G. Liu, Y. Tian, P. Zhang and X. Zhang, *Microsyst Technol.*, 2005, 11, 265.
- [8] M. S. Tokumoto, S. H. Pulcinelli, C. V. Santilli and A. F. Craievich, *J. Non-Cryst. Solids*, 1999, 247, 176.
- [9] A. Wood, M. Giersig, M. Hilgendorff, A. Vilas-Campos, L. M. Liz-Marzán and P. Mulvaney, *Aust. J. Chem.*, 2003, 56, 1051.
- [10] H.-C. Lin, F. Stehlin, O. Soppera, H.-W. Zan, C.-H. Li, F. Wieder, A. Ponche, D. Berling, B.-H. Yeh and K.-H. Wang, *Sci Rep.*, 2015, 5.
- [11] H. S. Lim, Y. S. Rim and H. J. Kim, *Sci Rep.*, 2014, 4.
- [12] Z. Hu, G. Oskam and P. C. Searson, *J. Colloid Interface Sci.*, 2003, 263, 454.
- [13] Y. S. Rim, H. Chen, Y. Liu, S. H. Bae, H. J. Kim and Y. Yang, *ACS nano*, 2014, 8, 9680.
- [14] L. Spanhel and M. A. Anderson, *J. Am. Chem. Soc.*, 1991, 113, 2826.
- [15] J. Bruncko, A. Vincze, M. Netrvalova, P. Šutta, D. Hasko and M. Michalka, *Thin Solid Films*, 2011, 520, 866.
- [16] S. K. Park, B. -K. Kang, J. -W. Shin, C. W. Joo, J. Moon, D. -H. Cho, B. Yu, H. Y. Chua and J. -I. Lee, *J. Mater. Chem. C*, 2014, 2, 4468.
- [17] A. Mendoza-Galvan, C. Trejo-Cruz, J. Lee, D. Bhattacharyya, J. Metson, P. J. Evans and U. Pal, *J. Appl. phys.*, 2006, 99, 014306.
- [18] L. Fanni, B. Delaup, B. Niesen, Y. Milstein, D. Shachal, M. Morales-Masis, S. Nicolay and C. Ballif, *Mater. Res. Express*, 2015, 2, 075006.
- [19] C. C. Yeh, H. C. Liu, M. Y. Chuang, J. Denzer, D. Berling, H. W. Zan and O. Soppera, *Adv. Mater. Interf.*, 2016, 3, 19.
- [20] J. H. Lee, K. H. Ko and B. O. Park, *J. Cryst. Growth*, 2003, 247, 119.
- [21] C. R. Martin and I. A. Aksay, *J. Phys. Chem. B*, 2003, 107, 4261.

Chapter V: Effect of Co-doping on photo-patterned ZnO structures



Résumé du chapitre V	121
5.1. Introduction.....	121
5.2. Investigating the incorporation of Co ions into ZnO lattice.....	122
5.3. Magnetic and electrical measurements of Co:ZnO films.....	126
5.3.1. Magnetic properties of Co:ZnO films	126
5.3.2. Electrical properties of Co:ZnO films.....	129
5.4. DUV-patterned Co:ZnO micro- and nanostructures	130
5.5 Conclusion and perspective	132
5.6. Bibliography	133

Résumé du chapitre V

L'objectif principal du Chapitre V est d'étendre le travail précédent pour obtenir un matériau à propriétés magnétiques photostructurables par DUV. Ceci est réalisé en dopant la matrice de précurseur de ZnO avec des ions Co^{2+} . Les conditions pour la photostructuration par lithographie DUV (193 nm) du précurseur de méthacrylate de zinc photosensible (ZnMAA) dopé avec de l'acétate de cobalt (II) sont ainsi définies des films Co: ZnO peuvent ainsi être préparés.

Dans un premier temps, l'effet de l'irradiation DUV ainsi que le recuit thermique sur les propriétés magnétiques des films de Co:ZnO dérivés du précurseur ZnMAA ont été étudiés. Ensuite, le nanopatterning par DUV des solutions photosensibles a été démontré.

Après la photostructuration, le matériau peut être transformé en films Co:ZnO par traitement thermique. Pour une compréhension approfondie de l'effet de l'irradiation DUV ainsi que du recuit thermique, les propriétés optiques, magnétiques et électriques ont été caractérisées sur des films Co: ZnO préparés par différentes conditions. L'analyse XPS et les mesures SQUID ont révélé que le recuit sous vide peut non seulement améliorer l'incorporation des ions Co^{2+} dans le réseau ZnO mais également améliorer de manière significative le signal FM pour les films Co:ZnO préparés sans irradiation DUV. Le signal FM fort a été expliqué par la formation de clusters de Co. D'autre part, bien que le signal FM soit plus faible, aucun cluster de Co n'a été observé dans le film Co:ZnO structuré par DUV après un recuit sous vide, ce qui indique que l'étape d'irradiation DUV améliore l'uniformité de la distribution des ions Co^{2+} dans le réseau ZnO. La résolution obtenue par le dispositif de lithographie interférentielle (~ 300 nm) ouvre des perspectives d'application dans le domaine de la spintronique.

5.1. Introduction

In recent years, wide band-gap diluted magnetic semiconductors (DMSs) such as transition metal (TM) doped ZnO and TM-doped TiO_2 are catching intense interest due to their expected potential applications in spin transistors, spin light emitting diodes, spin filters, sensors and memories.^[1-7] By using photopatterning techniques, TM doped metal oxide structures can be easily integrated in complex systems. In previous studies, Yuanqing Chen *et al.* have used photosensitive precursors and UV light to fabricate Co-doped ZnO and Co-doped TiO_2 patterns.^[8,9] However, these DMS structures are in microscale dimensions (> 100 μm), which cannot be integrated into small-dimension devices. In

addition, the effect of photopatterning on the magnetic properties of the TM-doped metal oxides was not investigated.

The objective of this Chapter is to extend the previous work to materials with magnetic properties, by doping the ZnO precursor matrix with Co ions. In more details, we used DUV (193 nm) lithography and photosensitive zinc methacrylate (ZnMAA) precursor doped with cobalt (II) acetate to fabricate Co:ZnO films. At first, the effect of DUV-patterning as well as thermal annealing on the magnetic properties of Co:ZnO films derived from Co-doped ZnMAA precursor were investigated. Then, DUV nanopatterning of the photosensitive solutions was demonstrated.

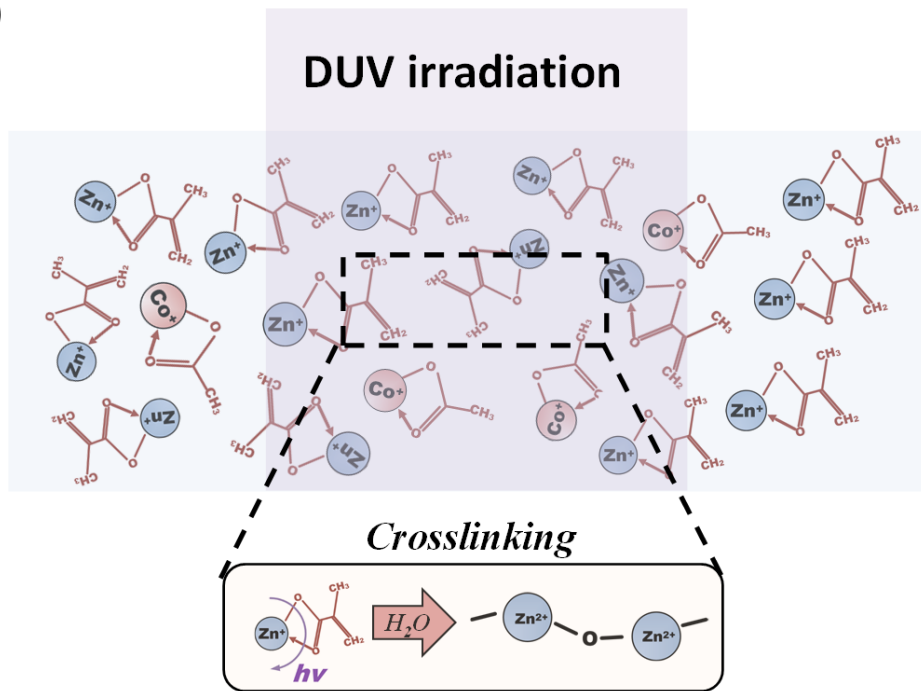
5.2. Investigating the incorporation of Co ions into ZnO lattice

The main strategy is to use zinc methacrylate ZnMAA as matrix resist with photosensitivity to DUV light of 193 nm.^[10] In the present case, conditions to introduce cobalt (II) acetate into ZnMAA solution with an atomic ratio $\text{Co}/(\text{Co}+\text{Zn}) = 0.15$ were defined and a stable photosensitive Co-doped ZnMAA precursor solution could be successfully prepared (see Chapter II). This solution can be used to prepare thin films by spin-coating and these films can be solidified by DUV irradiation via photo-induced crosslinking-condensation reactions. The photocrosslinking process relies, as described before, on a DUV induced photolysis of the ZnMAA complex followed by condensation reaction, as schematized in Figure 5.1a.^[11] It was shown previously that the DUV treatment is effective for crosslinking but some organic molecules remains in the film, even for long irradiation. Thermal treatment is used in a second step to remove the organic compounds embedded in the thin film, giving rise to the formation of crystalline Co:ZnO films.

To investigate the effect of DUV-patterning as well as of thermal annealing on Co:ZnO films, we prepared Co:ZnO films by spin-coating with different post-deposition processing, hereafter referred to sample A, sample B, and sample C, as shown in Figure. 5.1b. After spin-coating, sample A was annealed at 500 °C in air for one hour. Since many reports indicate that the room temperature ferromagnetism (RTFM) observed in Co-doped ZnO system originates from oxygen vacancy defects,^[12-14] sample B was firstly annealed at 500 °C in air for one hour and then annealed at 450 °C in vacuum (1×10^{-6} mbar) for three hours to increase oxygen vacancies. Sample C was patterned by DUV lithography after spin-coating and then annealed with the same condition as sample B. The thicknesses of Co:ZnO films determined by spectroscopic ellipsometry for the three conditions are all ~100 nm.

Figure 5.2a shows XPS spectra of Co 2p core of Co:ZnO films prepared by different conditions. Two peaks located at 780.2 eV and 795.4 eV were observed in the Co 2p spectrum of sample A, corresponding respectively to Co 2p_{3/2} and Co 2p_{1/2} peaks. On the other hand, besides Co 2p_{3/2} and Co 2p_{1/2} peaks, two additional peaks located at 786.2 eV and 802.3 eV were observed in the Co 2p spectra of sample B and sample C, corresponding to satellite peaks of high spin divalent Co²⁺ ions.^[15] The absence of the satellite peaks in the Co 2p spectrum of sample A suggests that most of the Co ions are low spin Co³⁺ which can be reduced to Co²⁺ by vacuum annealing. However, no significant difference was observed in the XPS Co 2p spectra between sample B and sample C, indicating that the binding state of Co ions is not affected by DUV-patterning. Figure 5.2b shows XPS spectra of O 1s core of Co:ZnO films prepared by different conditions. Generally, O 1s peak can be deconvoluted into three components O_(i), O_(ii) and O_(iii). The O_(i) component peak located at 529.6 eV, corresponds to oxygen ions in the fully oxidized surroundings. O_(ii) component peaked at 531.1 eV corresponds to oxygen ions in oxygen deficient regions, and O_(iii) component peaked at 532.3 eV is attributed to OH groups integrated into the Co-doped ZnO films.^[16] As shown in Figure 2b, no O_(i) component can be observed for sample B and sample C, which can be explained by the increase of oxygen vacancy defects in ZnO lattice due to the vacuum annealing. Figure 5.3 shows the optical absorption spectra of undoped ZnO and the Co:ZnO films prepared by different conditions. Due to its wide bandgap, no absorption was observed in visible light region of undoped ZnO film. On the other hand, absorption peaks located at 567, 610 and 655 nm were observed in the Co:ZnO films. These peaks are attributed to well-known d-d transition of Co²⁺ ions occupying tetrahedral lattice positions on Zn²⁺ sites.^[17, 18] The absorption intensities at 567, 610 and 655 nm are stronger in sample B and C than in sample A, showing that vacuum annealing increases the number of Co²⁺ ions substituted in the Zn²⁺ sites. The result is consistent with XPS analysis. However, R López Antón *et al.* reported that vacuum annealing can reduce CoO nanoparticles to metallic Co at temperature below 400 °C.^[19] XRD patterns of the vacuum-annealed Co:ZnO films (sample B and sample C) are shown in Figure 5.4. No secondary phase corresponding to Co clusters or cobalt oxide could be observed in the detection limit of the XRD technique.

(a)



(b)

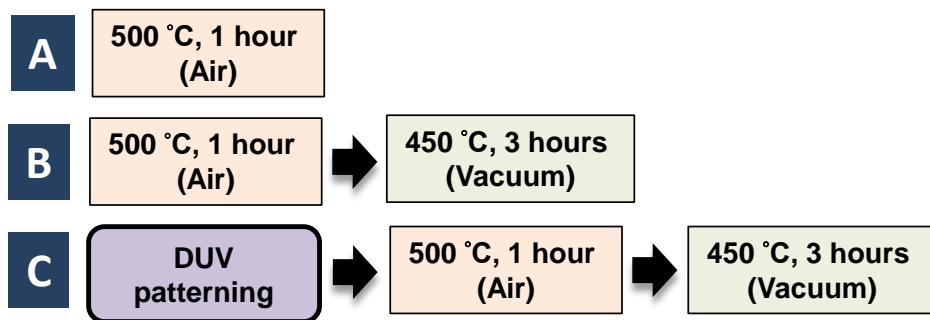


Figure 5.1. (a) Schematic view of the crosslinking reactions of ZnMAA complexes in the DUV-irradiated region.

(b) Schematic diagram showing three different fabrication procedures for the Co-doped ZnO samples.

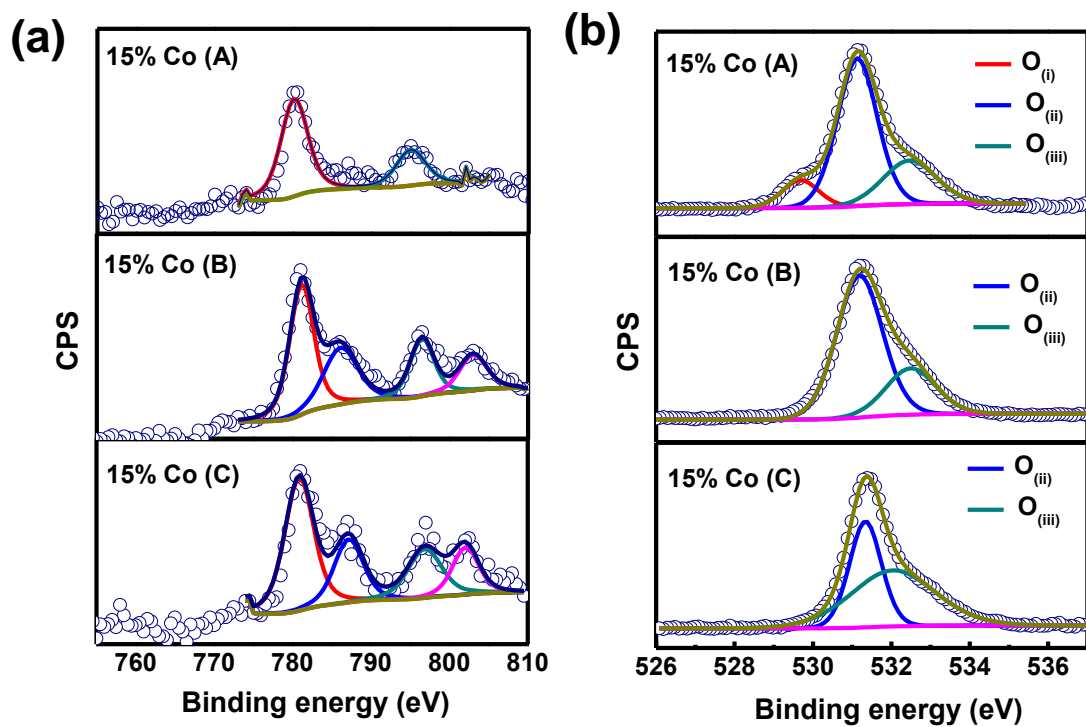


Figure 5.2. (a) XPS Co 2p and (b) O 1s spectra of the Co-doped ZnO samples.

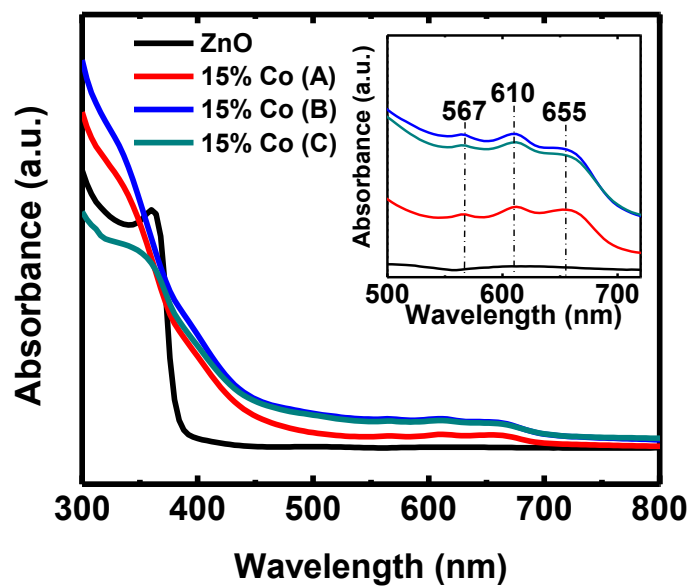


Figure 5.3. UV-vis spectra of the undoped ZnO and the Co-doped ZnO samples.

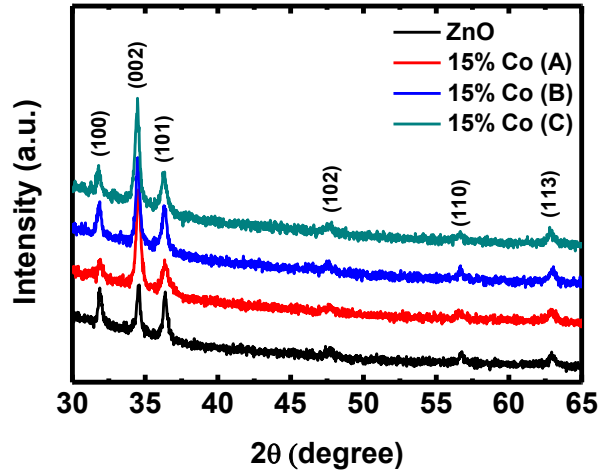


Figure 5.4. XRD patterns of undoped ZnO and Co-doped ZnO samples.

5.3. Magnetic and electrical measurements of Co:ZnO films

5.3.1. Magnetic properties of Co:ZnO films

Magnetic properties of Co:ZnO films were measured at room and variable temperatures using an alternative gradient field magnetometer (AGFM) and a superconducting quantum interference device (SQUID) magnetometer respectively. Figure 5.5a shows magnetization (M) versus field (H) curves of Co:ZnO films prepared under the 3 different conditions. Sample B exhibited ferromagnetic (FM) signal that is much stronger than sample A, indicating that vacuum annealing plays an important role in enhancing FM. In addition, we found that the FM signal of sample C is only half of the one of sample B, showing that DUV-patterning has great impact on magnetic properties. Since no significant difference was observed in chemical bindings as well as crystalline structures between sample B and sample C, the difference between the magnetic properties of sample B and sample C is probably due to very small Co clusters embedded in the Co:ZnO films. These clusters are too small to be detected by XPS analysis or XRD analysis but have great influence on magnetic properties.

Field-cooling (FC) and zero-field-cooling (ZFC) magnetization measurements can however unambiguously show the presence of very ultra-small magnetic particles or clusters in metal-oxide matrix.^[20,21] For an inhomogeneous metal-oxide matrix containing diluted magnetic clusters, superparamagnetic behavior with a clear blocking temperature (T_B) can be observed.^[22] Figure 5.5b shows FC and ZFC magnetization curves of sample B measured under external field of 500 Oe from 5 K to 300 K. Large discrepancy between the FC and ZFC curves was observed and a clear T_B at ~ 300 K

indicates that magnetic Co clusters are embedded in the film. The strong FM signal of sample B presented in the M-H curve in Figure 3a can thus be attributed to these Co clusters. In contrast, no clear T_B can be observed in FC and ZFC magnetization curves of sample C (Figure 5.5c), implying no Co cluster is embedded in the Co:ZnO film. The observation may be explained as follows, as illustrated in Figure 5.5d: in the solution and after spin-coating, Co complexes are distributed uniformly in the precursor. If the precursor is directly crystallized by air-annealing, due to self-purification effect, cobalt complexes in the precursor may migrate to form growing cobalt oxide grains. These Co rich regions can be reduced into metallic Co clusters during the vacuum annealing.^[19] On the other hand, if the gel-film is firstly patterned by DUV lithography, due to the M-O-M networks created by DUV irradiation, cobalt complexes are fixed at their positions, which suppresses the migration and aggregation of Co complexes and improves the uniformity of Co ion distribution in ZnO lattice. It's noteworthy that, in our previous work, such effect of DUV patterning has already been used to explain the significant improvement of the field-effect mobilities observed in DUV-patterned IGZO thin-film transistors. During the vacuum annealing, since there is no Co rich region in the film, no metallic Co cluster was formed. Figure 5.6a and Figure 5.6b show, respectively, the high resolution transmission electron microscopy (HRTEM) image and energy dispersive X-ray (EDX) elemental maps of sample C, no secondary phases due to cobalt clusters was observed, indicating Co ions distribute uniformly in the film.

RTFM observed in sample C can be explained by shallow donor model proposed by J. M. Coey *et al.* that the high Curie temperature is due to hybridization and charge transfer from shallow donor impurity band to unoccupied 3d states at the Fermi level.^[23] Furthermore, K. R. Kittilstved *et al.* summarized two general conditions in order to obtain conductive sample and RTFM which are (i) the potential of the reduced (or oxidized) dopant is similar to that of the shallow donor (or acceptor) (ii) small energy difference between reduced dopant to conduction band for n type DMS or oxidized dopant to valance band for p type DMS.^[24] Because after annealing in vacuum, weakly bonded atoms such as absorbed oxygen, interstitial zinc and oxygen atoms are supposed to be released from the sample, oxygen vacancies can thus be considered as the main source of shallow donor defects in the sample C. In addition, the energy difference between Co^+ level and oxygen vacancy level is as small as ~ 0.3 eV and the energy difference between Co^+ level and conduction band of ZnO is as small as ~ 0.3 eV,^[24, 25] fulfilling Kittilstved's conditions to exhibit RTFM.

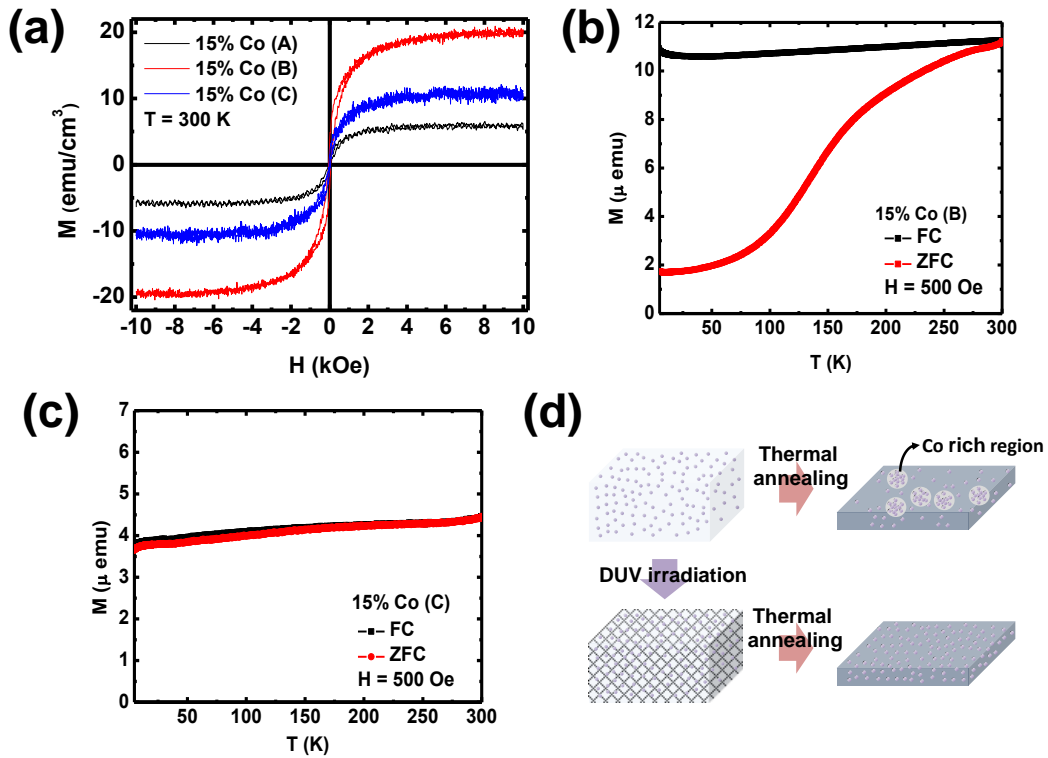


Figure 5.5. (a) M-H curves of the Co-doped ZnO samples. (b) FC and ZFC curves of sample B. (c) FC and ZFC curves of sample C. (d) Schematic view of the effect of DUV irradiation and thermal annealing on Co ion distribution.

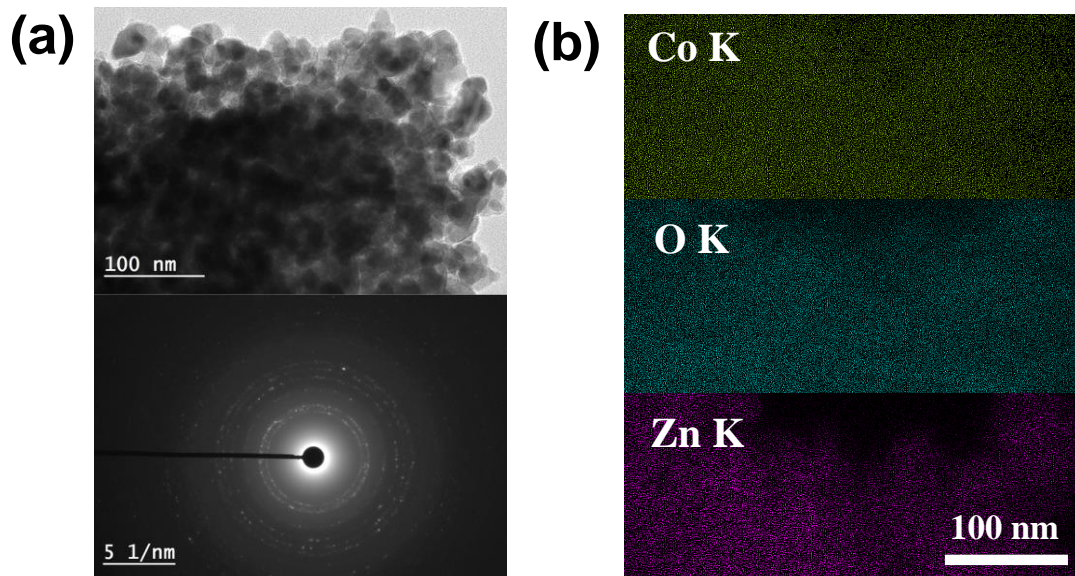


Figure 5.6. (a) HRTEM image and electron diffraction pattern of a Co-doped ZnO powder obtained from sample C. (b) EDX maps of K edge energies of Co, Zn and O in sample C.

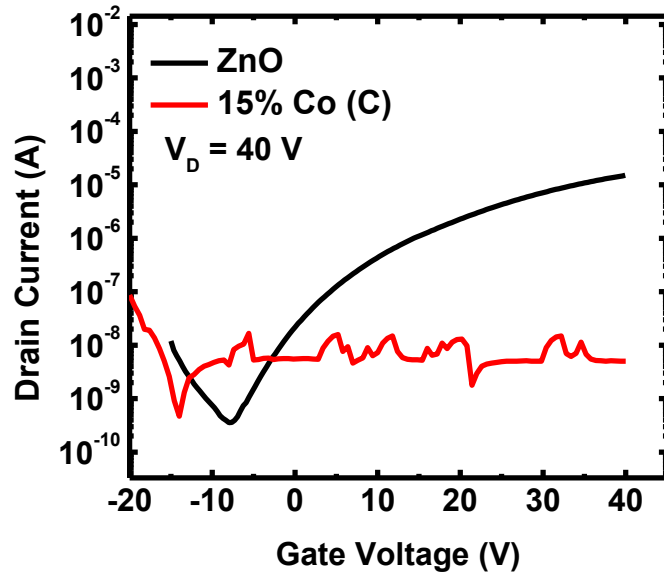


Figure 5.7. Transfer characteristics of undoped and Co-doped ZnO TFTs.

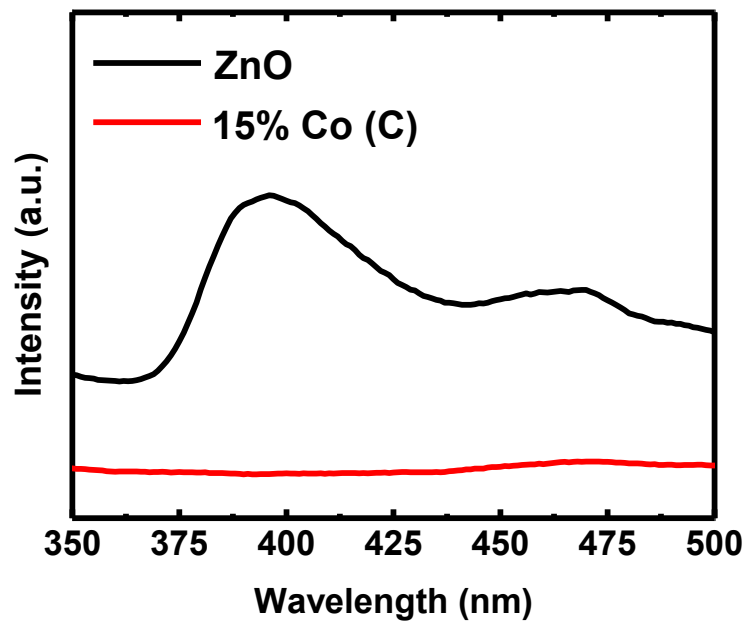


Figure 5.8. PL spectra of the undoped ZnO and the Co-doped ZnO sample.

5.3.2. Electrical properties of Co:ZnO films

To confirm the material structure, the effect of Co doping on electrical properties of ZnO was investigated, for DUV-patterned undoped ZnO thin film and Co-doped (15%) ZnO thin film which was annealed at the same condition as sample C. Both materials were integrated into transistor structure. Transfer characteristics (drain current versus gate voltage) of undoped ZnO and Co-doped ZnO

thin-film transistors (TFTs) are shown in Figure 5.7. Undoped ZnO TFT exhibits good transfer characteristics with on-off ratio $\sim 10^5$ and subthreshold swing ~ 3.3 V decade⁻¹. On the other hand, poor transfer characteristics were observed in Co-doped ZnO TFT, indicating that Co doping decreases the conductivity of ZnO film. According to the shallow donor model, RTFM is mediated by free electrons transferring from shallow donor defects to Co²⁺ ions.^[25] Thus, Co²⁺ ions can therefore be considered as trapping centers which decrease the free carrier concentration and therefore the conductivity. Additional energy levels induced by Co doping can be observed by photoluminescence (PL) spectroscopy analysis. In Figure 5.8, two emission peaks appear in the PL spectrum of undoped ZnO film. One large peak around ~ 395 nm and one small peak ~ 470 nm correspond respectively to the near-band emission (NBE) of ZnO and transition between oxygen vacancy and interstitial oxygen.^[26] On the other hand, no NBE peak can be observed in PL spectrum of the DUV-patterned Co-doped ZnO film (sample C), suggesting that excited electron-hole pairs fell into additional energy levels induced by Co doping without making radiative electron-hole recombination. Based on the results of optical characterizations, Zhiyan Xiao *et al.* suggest the existence of charge transfer (CT) levels below the conduction band of Co-doped ZnO. During light irradiation, photoexcited electron-hole pairs fall into CT levels and recombine non-radiatively.^[27] The absent of emission peak at ~ 470 nm in the Co-doped ZnO film might be due to the decrease of interstitial oxygen after vacuum annealing and confirm thus the previous results.

5.4. DUV-patterned Co:ZnO micro- and nanostructures

Finally, the patterning performance of Co-doped ZnMAA precursor is evaluated. One unique feature of our material is to be suitable for DUV lithography as a negative tone resist. We first used a binary mask of 833 nm line-width and DUV lithography to pattern the Co-doped zinc precursor as shown in Figure 5.9a. Well-defined Co:ZnMAA patterns can be obtained after development as shown in the atomic force microscopic (AFM) image Figure 5.9b. After thermal annealing at 500 °C in air for one hour, besides lateral and vertical shrinkage due to the removal of embedded organic species, a double-peak profile appeared on the topography of crystalline Co:ZnO lines (Figure 5.9c and Figure 5.9d), which can be explained by the inhomogeneous crystallization inside the patterns.^[28] In order to prove the nanoscale resolution line-width, DUV interference system was used to pattern Co-doped ZnMAA precursor as shown in Figure 5.10a. DUV interference can generate sinusoidal light intensity distribution of 600 nm period on the substrate. Periodic line patterns with ~ 300 nm line-width is then obtained. Figure 5.10b shows Co:ZnMAA nanostructures prepared by DUV interference system. After annealing thermal annealing, embedded organic compounds were removed, leading to the formation of

crystalline Co:ZnO nanostructures. (Figure 5.10c) In addition, the height of DUV-patterned nanostructures was decreases from ~ 100 nm to ~ 20 nm, but no lateral shrinkage was observed. (Figure 5.10d) These results suggest the potential of using Co-doped ZnMAA precursor combined with DUV lithography for fabricating nanoscale DMS structures.

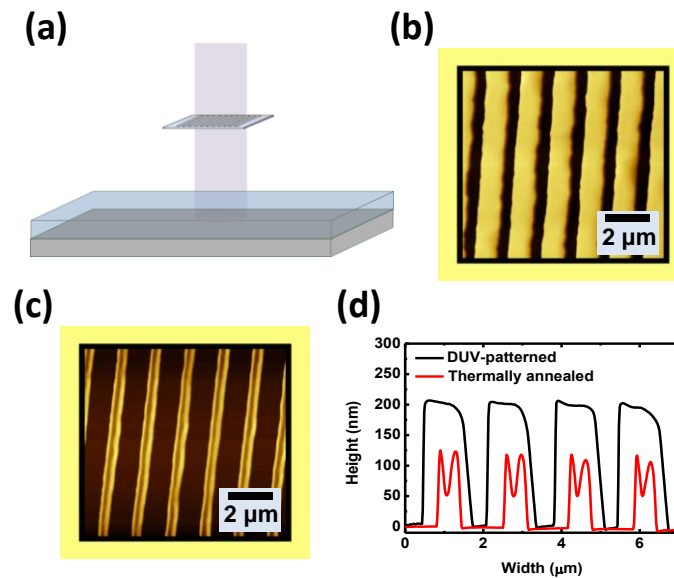


Figure 5.9. (a) Schematic view of DUV patterning with a binary mask of $1.6 \mu\text{m}$ period. (b) AFM image of periodic Co:ZnMAA lines prepared by mask lithography (c) AFM images of periodic Co:ZnO lines after thermal annealing (d) Cross-sectional profiles of periodic Co:ZnMAA lines before and after thermal annealing.

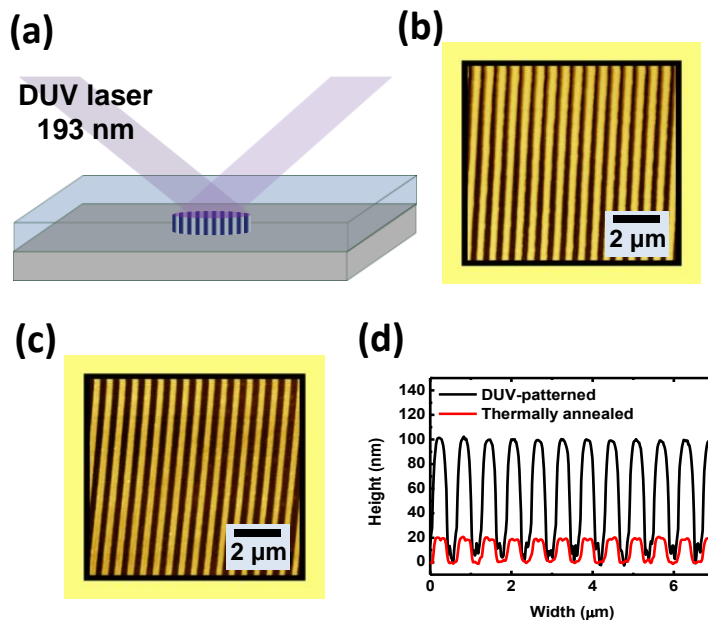


Figure 5.10. (a) Schematic view of DUV interference patterning. (b) AFM image of Co:ZnMAA lines of 600 nm period. (c) AFM image of periodic Co:ZnO lines of 600 nm period. (d) Cross-sectional profiles of periodic Co:ZnMAA lines before and after thermal annealing.

5.5 Conclusion and perspective

In summary, we mixed cobalt (II) acetate into zinc methacrylate (ZnMAA) to form a photosensitive Co-doped zinc precursor that can be patterned by DUV lithography as a negative tone resist. After photopatterning, it can be transformed into Co:ZnO films by thermal treatment. To have an in-depth understanding to the effect of DUV-patterning as well as thermal annealing on Co:ZnO films derived from Co-doped ZnMAA precursor, optical, magnetic and electrical characterizations were performed on Co:ZnO films prepared by different conditions. XPS analysis and SQUID measurements revealed that vacuum annealing can not only enhance the incorporation of Co^{2+} ions in ZnO lattice but also significantly enhance the FM signal for the Co:ZnO film prepared without DUV-patterning. The strong FM signal was explained by the formation of Co clusters. On the other hand, although FM signal is weaker, no Co clusters was observed in the DUV-patterned Co:ZnO film after vacuum annealing, indicating that DUV-patterning improves the uniformity of Co ions in ZnO lattice. Furthermore, the smallest line-width obtained from DUV interference patterning is as small as ~ 300 nm, which suggests the potential of using photopatterning and solution-processing methods for making future spintronic devices.

5.6. Bibliography

- [1] L. -T. Chang, C. -Y. Wang, J. Tang, T. Nie, W. Jiang, C. -P. Chu, S. Arafin, L. He, M. Afsal, L. -J. Chen and K. L. Wang, *Nano lett.*, 2014, 14, 1823.
- [2] M. Holub, P. Bhattacharya, *J. Phys. D: Appl. Phys.*, 2007, 40, R179.
- [3] X.J. Yang, Y.K. Li, C.Y. Shen, B.Q. Si, Y.L. Sun, Q. Tao, G.H. Cao, Z.A. Xu, F. C. Zhang, *Appl. Phys. Lett.*, 2013, 103, 022410.
- [4] Y. Jouane, S. Colis, G. Schmerber, C. Leuvrey, A. Dinia, P. Leveque, T. Heiser, and Y.A. Chapuis, *J. Mater. Chem.*, 2012, 22, 1606.
- [5] Y. Jouane, S. Colis, G. Schmerber, A. Dinia, P. Leveque, T. Heiser, and Y.A. Chapuis, *Org. Electron.*, 2013,14, 1861.
- [6] M. Balestrieri, S. Colis, M. Gallart, G. Ferblantier, D. Muller, P. Gilliot, P. Bazylewski, G.S.Chang, A. Slaoui, and A. Dinia, *J. Mater. Chem. C*, 2014, 2, 9182.
- [7] I. Soumahoro, S. Colis, G. Schmerber, C. Leuvrey, S. Barre, C. Ulhaq-Bouillet, D.Muller, M. Abd-lefdil, N. Hassanain, J. Petersen, A. Berrada, A. Slaoui, A. Dinia, *Thin Solid Films*, 2014, 566, 61.
- [8] Y. Chen, G. Zhao, F. Yan, *J. Sol-Gel Sci. Technol.*, 2010, 54, 325.
- [9] Y. Chen, G. Zhao, Y. Ren, Z. Wang, *Thin Solid Films*, 2011, 519, 1985.
- [10] C. C. Yeh, H. C. Liu, M. Y. Chuang, J. Denzer, D. Berling, H. W. Zan and O. Soppera, *Adv. Mater. Interfaces*, 2016, 3, 19.
- [11] F. Stehlin, F. Wieder, A. Spangenberg, J. M. Le Meins and O. Soppera, *J. Mater. Chem. C*, 2014, 2, 277.
- [12] Z. Y. Wu, F. R. Chen, J. J. Kai, W. B. Jian, J. J. Lin, *Nanotechnology*, 2006, 17, 5511.
- [13] G. Chen, C. Song, C. Chen, S. Gao, F. Zeng, F. Pan, *Adv. Mater.*, 2012, 24, 3515.
- [14] H. Chou, K.-S. Yang, Y.-C. Tsao, G. D. Dwivedi, C.-P. Lin, S.-J. Sun, L. K. Lin, S. F. Lee, *Appl. Phys. Lett.*, 2016, 108, 142404.
- [15] X. Wang, R. Zheng, Z. Liu, H. P. Ho, J. Xu, S. P. Ringer, *Nanotechnology*, 2008, 19, 455702.
- [16] Y. H. Hwang, S. J. Seo, J. H. Jeon, B. S. Bae, *Electrochem. Solid-State Lett.*, 2012, 15, H91.
- [17] J. J. Beltrán, C. A. Barrero, A. Punnoose, *J. Phys. Chem., C* 2014, 118, 13203.
- [18] M. Bouloudenine, N. Viart, S. Colis, and A. Dinia, *Chem. Phys. Lett.*, 2004, 397, 73
- [19] R. L. Antón, J. A. González, J. P. Andrés, J. Canales-Vázquez, J. A. De Toro, J. M. Riveiro, *Nanotechnology*, 2014, 25, 105702.
- [20] W. Wan, J. Huang, L. Zhu, L. Hu, Z. Wen, L. Sun, Z. Ye, *CrystEngComm*, 2013, 15, 7887.
- [21] R. Larde, E. Talbot, P. Pareige, H. Bieber, G. Schmerber, S. Colis, V. Pierron-Bohnes, and A. Dinia, *J. Am. Chem., Soc.* 2011, 133, 1451

- [22] J. H. Park, M. G. Kim, H. M. Jang, S. Ryu, Y. M. Kim, *Appl. Phys., Lett.* 2004, 84, 1338.
- [23] J. M. D. Coey, M. Venkatesan, C. B. Fitzgerald, *Nat. Mater.*, 2005, 4, 173.
- [24] K. R. Kittilstved, W. K. Liu, D. R. Gamelin, *Nat. Mater.*, 2006, 5, 291.
- [25] Q. Zhu, C. Xie, , H. Li, C. Yang, S. Zhang, D. Zeng, *J. Mater. Chem. C*, 2014, 2, 4566.
- [26] V. Gandhi, R. Ganesan, H. H. Abdulrahman Syedahamed, M. Thaiyan, *J. Phys. Chem. C*, 2014, 118, 9715.
- [27] Z. Xiao, H. Matsui, N. Hasuike, H. Harima, H. Tabata, *J. Appl. Phys.* 2008, 103, 043504.
- [28] C. C. Yeh, H. C. Liu, W. Heni, D. Berling, H. W. Zan, O. Soppera, *J. Mater. Chem. C*, 2017, 5, 2611.
- [29] H.-C. Lin, F. Stehlin, O. Soppera, H.-W. Zan, C.-H. Li, F. Wieder, A. Ponche, D. Berling, B.-H. Yeh, K.-H. Wang, *Scientific reports* 2015, 5.

Conclusions and outlook

In this thesis, an in-depth investigation to the photosensitive zinc methacrylate precursor was made. Zinc methacrylate can be crosslinked under DUV (193) and irradiation. The photo-induced solidification is attributed to the π to π^* electronic transition in the ZnMAA complex, which gives rise to the following hydrolysis-condensation reactions and the formation of Zn-O-Zn networks. The bonding variation and decomposition of organic species caused by DUV irradiation were carefully investigated by FTIR and discussed in Chapter III. The decrease of peaks at 1410 cm^{-1} and 1570 cm^{-1} after DUV irradiation implies MAA ligands were cleaved from zinc cations. However, the intensity of MAA ligands can only be reduced to $\sim 2/3$ of its initial intensity regardless the extension of irradiation time, implying only a small amount oxide network can be induced by DUV irradiation. The small amount of Zn-O-Zn networks inside the photo-irradiated regions can effectively decrease the solubility of photo-irradiated regions in polar solvents such as ethanol, 1-propanol, cyclohexanone, which makes ZnMAA precursor just like a negative tone resist and able to be patterned into two-dimensional structures by DUV lithography. Due to good photosensitivity to DUV light (193 nm), the dimension of DUV-patterned ZnMAA structures can be decreased to sub-micro by using binary masks and the effects of each pattering step including (i) DUV exposure, (ii) prebaking and (iii) development on the size and shape of DUV-patterned ZnMAA structures are discussed in Chapter IV. In order to fabricate nanoscale ZnMAA structures, a home-made DUV interference system was used to pattern ZnMAA precursor and 300 nm periodic lines were successfully made.

The DUV-patterned crosslinked ZnMAA organic-inorganic hybrid structures can be directly converted to ZnO structures by thermal annealing. XPS, XRD, ellipsometry, Raman spectroscopy and atomic force microscopy were performed to analyze the thermally-crystallized ZnO thin-films and structures. The minimum temperature required to completely decompose organic species inside the ZnMAA precursor was found to be around $400\text{ }^\circ\text{C}$. In addition, the formation of ZnO leads to a clear absorption bandgap $\sim 3.3\text{ eV}$ in the absorption spectrum and the crystalline structure of ZnO was found to be Wurzite 2H type by using XRD analysis. Due to removal of organic compounds and crystallization of ZnMAA, the size and shape of DUV-patterned ZnMAA structures were changed. A

double-peak profile appeared in DUV-patterned ZnMAA lines after thermal annealing at temperatures above 300 °C. The formation of double-peak profile was explained by the inhomogeneous crystallization in the ZnMAA lines. The crystallization process starts earlier for ZnMAA close to the surface than ZnMAA deep inside the structures as discussed in Chapter IV. In addition, after complete crystallization, the volume of DUV-patterned ZnMAA structures shrank to ~20% of its initial volume, suggesting most of the ZnMAA structures crosslinked by DUV irradiation are organic compounds.

Because ZnO is a well-known n-type semiconducting material, electrical measurements were performed to investigate the electrical properties of DUV-patterned ZnO structures. No electrical property was observed for ZnMAA film annealed at temperature below 400 °C, which is attributed to incomplete removal of organic compounds inside the film. For ZnMAA films crystallized at temperatures above 400 °C, semiconducting property can be characterized and the conductivity was found to increase with the increase of annealing temperature. This observation can be explained by the growth of bigger ZnO grains at higher annealing temperature, which reduces grain boundaries and electron scattering. Thermally-crystallized semiconducting ZnO films were integrated into thin-film transistor and gas sensors and the device performance was evaluated. The field-effect mobility observed in the DUV-patterned ZnO transistor is ~ 0.4 cm²/Vs and clear sensing responses were observed when exposed to acetone and nitrogen monoxide at several ppm level. These results show the potential of using DUV-patterned ZnO for to fabricate functional devices.

Thanks to solution processing method, it is possible to dope ZnMAA precursor with other kinds of metal salts, forming a new type of precursor solution containing different kinds of cations. Aluminum acetylacetonate and cobalt acetate were doped into ZnMAA precursor for making Al-doped ZnO and Co-doped ZnO thin films and structures. For aluminum acetylacetonate doped (3%) ZnMAA precursor, no degradation of photosensitivity was found. Fine Al doped ZnMAA structures can be patterned by DUV lithography. After thermal annealing, Al dope ZnMAA structures can be converted to Al:ZnO structures and the conductivity of Al:ZnO can be around ten times higher than undoped ZnO. The increase of conductivity is attributed to free electrons released from Al dopants incorporated into the ZnO lattice. In addition, room temperature ferromagnetism was observed in Co-doped (15%) ZnO films derived from ZnMAA precursor doped with cobalt acetate. Since no bifurcation was observed between FC and ZFC curves in SQUID measurements, the occurrence of room-temperature ferromagnetism was explained by the formation of bound magnetic polarons rather than metallic cobalt clusters. It's noteworthy that only a small amount of aluminum acetylacetonate or cobalt acetate was

doped into ZnMAA precursor; therefore, the photosensitivity of ZnMAA precursor was almost not affected. For high doping concentration, the photosensitivity of each type of metal salt has to be considered to avoid degradation of precursor in the photopatterning procedure.

Even though a comprehensive investigation was made to ZnMAA precursor, DUV-patterned ZnMAA and ZnO structures, which provides a model system for photopatterning with metal oxide precursors, there are still challenges remains regarding to annealing temperature and crystalline quality for ZnO thin-films and structures. The minimum annealing temperature required to convert ZnMAA to semiconducting ZnO was found to be around 400 °C. However, for flexible substrates such as plastic foils and textiles, the annealing temperature has to be lower than 200 °C. To effectively reduce the minimum annealing temperature, a new chemical route or chemical modification to ZnMAA precursor is in need and worth further investigation. The crystalline structure of ZnO derived from thermally crystallized ZnMAA precursor on silicon substrate is polycrystalline with a lot of grain boundaries and defects, which is inferior to c-axis orientated single-crystal ZnO for carrier transport. Since the nucleation and growth of ZnO crystals are affected by many factors such as solvent, solution concentration, substrate material, heating rate and additive, the crystalline structures of ZnO may be further improved by adjusting the fabrication parameters, leading to higher mobility in electronic devices.

The author wishes this study can provide fundamental knowledge and inspire new ideas for researchers working in this field and other related fields using solution processing for making micro- and nanostructures.